



HAL
open science

Trees on Geometrical Deformations to Model the Statistical Variability of Organs in Medical Images

Christof Seiler

► **To cite this version:**

Christof Seiler. Trees on Geometrical Deformations to Model the Statistical Variability of Organs in Medical Images. Medical Imaging. Université Nice Sophia Antipolis; Universität Bern, 2012. English. NNT: . tel-00844610

HAL Id: tel-00844610

<https://theses.hal.science/tel-00844610>

Submitted on 15 Jul 2013

HAL is a multi-disciplinary open access archive for the deposit and dissemination of scientific research documents, whether they are published or not. The documents may come from teaching and research institutions in France or abroad, or from public or private research centers.

L'archive ouverte pluridisciplinaire **HAL**, est destinée au dépôt et à la diffusion de documents scientifiques de niveau recherche, publiés ou non, émanant des établissements d'enseignement et de recherche français ou étrangers, des laboratoires publics ou privés.

u^b

b
**UNIVERSITÄT
BERN**



University of Bern, Graduate School for Cellular and Biomedical Sciences
and
University of Nice Sophia Antipolis, Sciences et Technologies de
l'Information et de la Communication (ED STIC)

Trees on Geometrical Deformations to Model the Statistical Variability of Organs in Medical Images

Ph.D. Thesis submitted by **Christof SEILER** (from Madiswil, Bern)

for the joint degree of

Doctor of Philosophy in Biomedical Engineering

from the University of Bern

and

Docteur en Sciences

from the University of Nice Sophia Antipolis

Mention: Automatique, traitement du signal et des images

Thesis Advisors: **Mauricio REYES and Xavier PENNEC**

Defense: September 27, 2012

Jury:

Sebastien OURSELIN, Ph.D., Prof.	University College London
Rasmus R. PAULSEN, Ph.D., Prof.	Technical University of Denmark
Marco-D. CAVERSACCIO, M.D., Prof.	University Hospital Bern
William M. WELLS III, Ph.D., Prof.	Harvard and MIT
Mauricio REYES, Ph.D.	University of Bern
Xavier PENNEC, Ph.D.	INRIA Sophia Antipolis

Accepted by the Faculty of Medicine, and the Faculty of Science of the University of Bern at the request of the Graduate School for Cellular and Biomedical Sciences,

Bern, Dean of the Faculty of Medicine

Bern, Dean of the Faculty of Science

Bern, Dean of the Vetsuisse Faculty Bern

This Ph.D. thesis was prepared at the Medical Image Analysis group, Institute for Surgical Technology and Biomechanics, University of Bern, Stauffacherstrasse 78, 3014 Bern, Switzerland and at the Asclepios team, INRIA Sophia Antipolis - Méditerranée, 2004 route des Lucioles, BP 93, 06902 Sophia Antipolis Cedex, France.

Abstract

In medical image analysis, geometrical deformations are used to model intersubject variability. In orthopaedic applications, the geometrical variability is usually observable across anatomical scales. For instance, anatomical differences between mandible bones of different patients can be found on a coarse scale, between the entire left or right side, or on a fine scale, between teeth. Each level of granularity has specific regions of interest in clinical applications. The challenge is to connect the geometrical deformations to clinical regions across scales.

In this thesis, we present this connection by introducing structured diffeomorphic registration. At the core of our method is the parametrization of geometrical deformations with trees of locally affine transformations describing intersubject variability across scales. In a second step, we statistically model the deformation parameters in a population by formulating a generative statistical model. This model allows us to incorporate deformation statistics as a prior in a Bayesian setting and it enables us to extend the classical sequential coarse to fine registration to a simultaneous optimization of all scales. This kind of group level prior is natural in a polyaffine context, if we assume one configuration of regions that describes an entire group of images with varying transformations for each region.

We validate our approach on a wide range of orthopaedic applications: population-based implant design, biomechanical simulations and allograft selection for femur and mandibles. The improved intelligibility for clinicians and accuracy makes our method a good candidate for clinical use.

Keywords: Parametrization of diffeomorphisms, Shape statistics, Multiscale and hierarchical trees, Log-Euclidean polyaffine transformations, Polyaffine registration, Log-Demons registration, Generative statistical model, Bayesian registration

Résumé

Dans l'analyse d'images médicales, les déformations géométriques sont utilisées pour modéliser la variabilité entre les patients. Dans les applications orthopédiques, la variabilité géométrique est habituellement observable à différentes échelles. Dans le cas des os mandibulaires, par exemple, on observe des différences anatomiques entre le côté gauche et droit sur une échelle grossière, ou entre les dents sur une échelle plus fine. Chaque niveau de granularité contient des régions d'intérêt pour les applications cliniques. La difficulté est de relier les déformations géométriques avec les régions d'intérêt pour chaque type d'échelles.

Dans cette thèse, nous présentons cette liaison par l'introduction du recalage difféomorphe et structuré. Le coeur de notre méthode est le paramétrage des déformations géométriques avec des arbres de transformations localement affines qui décrivent la variabilité entre les patients. En second lieu, nous modélisons statistiquement les paramètres de déformations dans une population par la formulation d'un modèle statistique génératif. Cette méthode nous permet d'intégrer des statistiques de déformations comme une probabilité a priori dans un cadre Bayésien et elle nous permet d'étendre le recalage classique d'un schéma grossier à un schéma fin avec une optimisation simultanée pour toutes les échelles.

Nous validons notre approche sur plusieurs applications orthopédiques: la conception des implants pour une population, des simulations biomécaniques et la sélection d'allogreffes. L'amélioration de l'intelligibilité pour les cliniciens et de la précision obtenue fait de notre méthode un candidat prometteur pour des usages cliniques.

Mots-clés: Paramétrisation des difféomorphismes, Statistiques de forme, Arbres multi-échelles et hiérarchiques, Transformations log-euclidiennes polyaffines, Recalage polyaffine, Recalage log-demons, Modèle statistique génératif, Recalage bayésien

Acknowledgments

First, I would like to thank my thesis advisors Xavier Pennec and Mauricio Reyes. I will never forget the long meetings Xavier and I had in Sophia (the longest was seven hours without breaks). These meetings fundamentally changed the way I think. After every meeting with Xavier, I was full of new ideas and inspiration. But these meetings were far more than only a source of inspiration, equally important was that we developed the methods from the ground up. I learned how to ask scientific questions, among many other things.

I would like to thank Mauricio for guiding me through the Ph.D. thesis. It was with him that I first came in contact with scientific problems. With his creativity and out of the box thinking, he showed me how to tackle problems from different angles. He also gave me the opportunity to conduct my research both in Switzerland and France, and as a visiting graduate fellow at SAMSI¹. I will always be thankful for his support and trust during the past years.

Second, I would like to thank the reviewers of this manuscript, Rasmus R. Paulsen and Sebastien Ourselin, for reading my thesis. I am looking forward to their feedback and interesting discussions.

A special thank you note is dedicated to Isabelle Strobant and Barbara Schmitter, without whom it would have been impossible to organize the joint Ph.D. between France and Switzerland.

As mentioned above, I spent the Fall Semester 2010 in North Carolina as a Graduate Fellow at SAMSI. During that time I met many inspiring people, some of whom are: J.S. Marron, UNC at Chapel Hill, who was my advisor during that time; Hans George Müller, University of California, Davis; Viktor Panaretos, EPFL; Ian Dryden, University of South Carolina; Martin Styner, who let me participate in the weekly “Shape Stats” meetings at UNC; Marc Niethammer, and Stephen Pizer from UNC.

I would like to thank my collaborators: Rémi Blanc, ETH; Tateyuki Iizuka, Department of Cranio-Maxillofacial Surgery, University of Bern, for providing us with valuable clinical feedback; Lucas Ritacco, Italian Hospital of Buenos Aires, Argentina, and Michael Kistler, University of Bern, for manually measuring landmarks on 146 femur CT images; Serena Bonaretti and Habib Bou-Sleiman, University of Bern; Krissy McLeod, INRIA Sophia Antipolis, and Nicolas Bronsard, Centre Hospitalier Universitaire de Nice, France.

Finally, I would like to thank my family and friends for their support: My mother Ursula Hofmann, my father Martin, my sisters Anna and Eva Seiler, my cousin Andrea Hofmann; Harald Studer, for being part of our journey to become scientists; Serena Bonaretti, for questioning everything and introducing me to the Italian way of eating; Marco Lorenzi, for his smart input, salesmanship advice and for making me buy printed books again; Jay Sungu, for visiting me in France after

¹Statistical and Applied Mathematical Sciences Institute, NC, USA

so many years of living on different continents; Krissy McLeod, Stefan Feissli, Edith Remund, Anna Weber, Stefanie Studer, Christoph Studer, Betina and Amir Kleiner Qamar, Stephanie Marchesseau, Vikash Gupta, Hervé Lombaert, the entire MIA group at ISTB, University of Bern and the entire Asclepios Research Group at INRIA Sophia Antipolis.

Contents

1	Introduction	1
1.1	Ontology of the Human Anatomy	2
1.1.1	Anatomical Structure, Granularity and Relations	2
1.1.2	Intersubject Anatomical Variability – Big Data	4
1.2	Modeling of the Human Anatomy	6
1.2.1	An Engineer’s View: Algorithmic Modeling of Organs	6
1.2.2	A Statistician’s View: Modeling of the Variability	8
1.2.3	A Clinician’s View: Intelligibility of Models	9
1.3	Structure of the Manuscript and Contributions	10
1.4	List of Publications and Awards	11
2	Capturing the Multiscale Anatomical Shape Variability	15
2.1	Implant Design for Mandible Fractures	17
2.1.1	Clinical Problem	17
2.1.2	Methodological Framework	18
2.2	Projection of SVFs Onto the Linear Space of LEPTs	20
2.2.1	Exponential and Logarithm of Matrices	22
2.2.2	Exponential and Logarithm of Vector Fields	23
2.2.3	Our Contribution: Linear Projection	23
2.2.4	New Metric on Stationary Velocity Fields	24
2.3	Hierarchical Structuring of Polyaffine Transformations in Trees	24
2.4	Anatomy-Driven Definition of Regions	25
2.4.1	OBBTree on Contour Extracted from Template Image	25
2.4.2	OBBTree on Feature Image Extracted from Template Image	26
2.5	Estimation of Transformations	27
2.5.1	Log-Demons Algorithm	28
2.5.2	Integration of the Estimation into the Log-Demons	29
2.6	Femur Bone Registration with Manual Regions	30
2.6.1	Clinical Problem	30
2.6.2	Special Case of a Polyaffine Transformation Tree	31
2.6.3	Validation with Landmark Measurements by Medical Experts	31
2.7	Mandible Bone Registration with Hierarchical Regions	32
2.7.1	Weights Derived from Oriented Bounding Boxes	35
2.7.2	Estimation of the Transformation Tree	35
2.7.3	Analysis of Obtained Tree Transformations	38
2.8	Implant Design Based on Statistical Analysis	38
2.8.1	Link Between Clinical and Data-Driven Regions	38
2.8.2	Clustering of Polyaffine Parameters for Selected Regions	40
2.9	Discussion and Conclusion	40

3	A Generative Statistical Model for Deformations	45
3.1	Introduction	47
3.1.1	Ontology of the Human Anatomy	47
3.1.2	Population-Based Implant Design	49
3.1.3	Trees on Geometrical Deformations	50
3.2	A GLM Formulation of Intersubject Deformations	51
3.2.1	Linear Model for Deformations	53
3.2.2	Observing Noisy Stationary Velocity Fields	53
3.3	A Generative Statistical Model for Deformations	54
3.3.1	Posterior Inference of Polyaffine Parameter	54
3.3.2	Sample Covariance Matrix Inverse	55
3.4	Experiments on Real CT Data	57
3.4.1	Comparison of Sample Covariance Inverse Methods	59
3.5	Discussion and Conclusion	65
4	Clinical Applications	67
4.1	Left-Right Symmetry in Femur and Tibia Bones	68
4.2	Regression of Geometrical Deformations in Femur Bones	71
4.3	Biomechanics of Femur Bones	78
4.4	Allograft Selection for Femur Bones	80
4.5	Implant Shape Design for Mandible Bones	82
4.6	Prediction of Bone Surface for Orthopaedic Research	83
4.7	Heart Modeling with Incompressibility Constraints	85
5	Conclusion and Perspectives	87
5.1	Conclusion	88
5.2	Short Term Perspectives	89
5.2.1	Validation on 100'000 Landmarks in 400 Spine CT's	89
5.2.2	More Structures: Spine, Whole Body Scans, Brain	90
5.2.3	Regions Derived from Atlases	92
5.2.4	Multivariate Regression on Geometrical Deformations	92
5.3	Long Term Perspectives	92
5.3.1	Probabilistic FEM Parameterized with PTTs	93
5.3.2	Empirical Bayes Method to Optimize Hyperparameter	93
5.3.3	Sparse Anatomical Relations at the Group Level	93
5.3.4	Hyperpriors for Polyaffine Parameter	93
5.3.5	Applied Topology to Analyze Tree Deformations	94
5.3.6	A Prior Distribution of Weight Trees	94
5.3.7	Image Registration by MCMC Simulations	96
5.3.8	Angiogenesis of Heart Muscle Fibers	96
A	Appendix: Phylogenetic Trees	99
A.1	What are Phylogenetic Trees?	99
A.2	Geometry of Phylogenetic Tree Space	99

B Appendix: Directional Derivative of Matrices	103
C Appendix: Implementation in ITK	105
C.1 Extending the Log-Demons Code	105
C.2 Trees in ITK	106
C.3 New Transformation Class for Polyaffine Trees	106
C.4 Input Parameters	106
C.5 Output Parameters	107
C.6 Example	107
Bibliography	109

Introduction

Contents

1.1	Ontology of the Human Anatomy	2
1.1.1	Anatomical Structure, Granularity and Relations	2
1.1.2	Intersubject Anatomical Variability – Big Data	4
1.2	Modeling of the Human Anatomy	6
1.2.1	An Engineer’s View: Algorithmic Modeling of Organs	6
1.2.2	A Statistician’s View: Modeling of the Variability	8
1.2.3	A Clinician’s View: Intelligibility of Models	9
1.3	Structure of the Manuscript and Contributions	10
1.4	List of Publications and Awards	11

1.1 Ontology of the Human Anatomy

The term *anatomy* originates from the two Greek words *ana* and *temnein*, which translate in English to *apart* and *to cut*, respectively. The origin of this word leads us directly to the essence of this manuscript, which is to deepen our understanding of parts of our human body and how they interact. A quote from [Benjamin 1994] reads:

“The traditional goal of ontological inquiry in particular is to divide the world ‘at its joint’ to discover those fundamental categories or kinds into which the world’s objects naturally fall.”

As the reader will see this quote is an apt summary of the manuscript presented herein. In the following, we describe the ontology of human anatomy and how it helps us understand the underlining challenges in this field.

The Foundational Model Anatomy (FMA) ontology, as presented in [Rosse 2008], is a formal description of classical human anatomy textbooks. In classical textbooks the anatomy is divided according to function or regions. The FMA provides a more formal definition of the division process. At the core of the FMA is a tree data structure that represents the hierarchical and multiscale anatomical shape at different levels of granularity.

1.1.1 Anatomical Structure, Granularity and Relations

The FMA definition of anatomical structures is given by the following three points:

1. Anatomical structures are three-dimensional shapes
2. Anatomical structures are products of our genes
3. The parts of an anatomical structure are arrangements through our genes

Therefore, a mathematical description of anatomical structures needs to be able to describe three-dimensional shapes that are divided into parts and interact with other parts of the same or other anatomical structures. A quote from [Rosse 2008] reads:

“In conclusion, anatomical structures at each level of granularity share some structural properties inherited from their taxonomic ancestors, and also exhibit additional properties specific to their own level. These inherited and level-specific attributes account for the emergent properties of anatomical structures at levels of increasing structural complexity. One of these emergent properties is the potential they manifest for participating in higher level biological processes than those at a lower level...”

We can see that one central point is the tree-based description of the anatomy, where entities at finer levels of granularity inherent properties form coarser levels. This kind of reasoning is implicitly considered in many medical image analysis algorithms

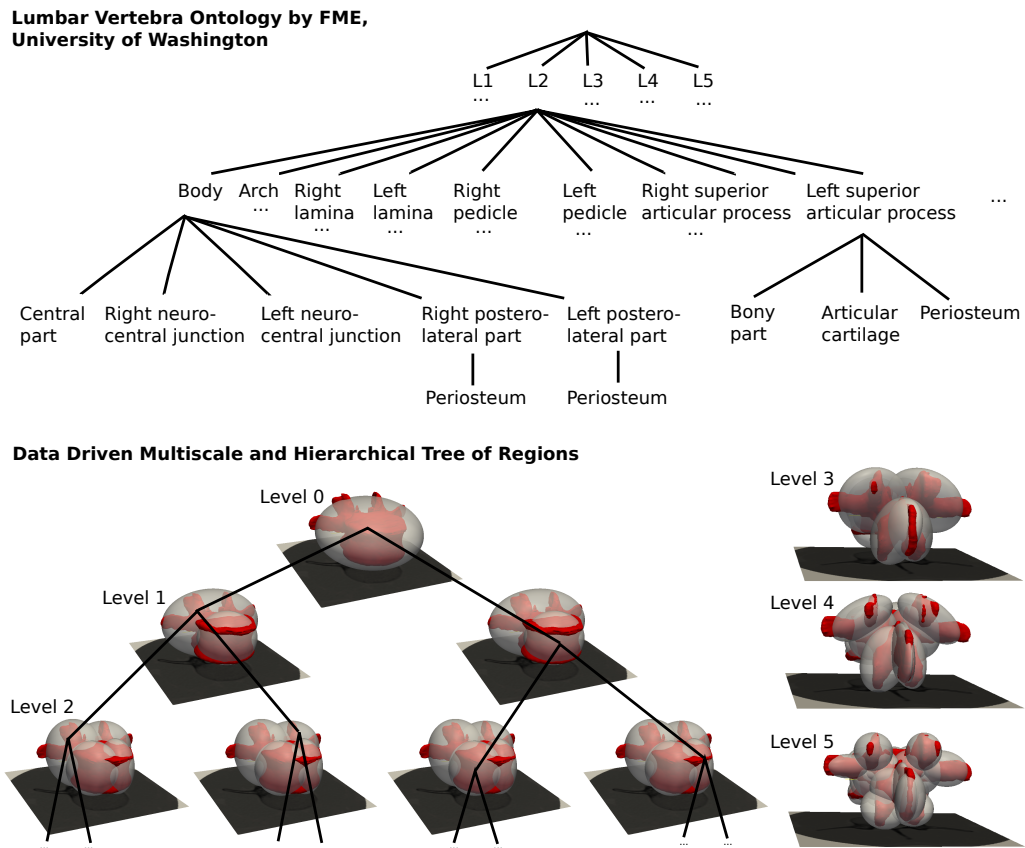


Figure 1.1: **Top:** Ontology of lumbar vertebra anatomy. Subdivision of vertebra into anatomical regions proposed by [Foundational Model Explorer](#), University of Washington [Rosse 2008]. **Bottom:** Tree of Gaussian weights. Weights divide the anatomy into continuous parts. The tree can be directly interpreted by clinicians. Each Gaussian weight represents one region and is visualized as one ellipsoid thresholded at σ . The red contours are extracted from CT data and one slice of the original CT image is shown (to indicate that we work in the image domain and not only on the contour).

through a (multiscale) coarse to fine analysis. In this work, we make it explicit by modeling the granularity with trees of geometrical deformations.

In the context of anatomy, the term granularity refers to the level of detail at which we observe or describe the anatomical structure. It defines the extent to which the anatomy is broken down into small parts. In Figure 1.1, the lumbar vertebral body L2 is shown at different levels of granularity. On the top, we see a small extract of the FMA ontology from the University of Washington [Rosse 2008]. On the bottom, an illustration of the data-driven approach that we present in this manuscript is given.

According to FMA, anatomical relations are associations between anatomical entities. Relations are visualized with edges between nodes in the ontology tree (Fig. 1.1). This means that anatomical structures can not only be described by their spatial location but also indirectly through their related structures. In the realm of medical image analysis, researchers have been exploring these connections through statistical analysis of cohorts of functional and structural images. Particularly interesting are relations that are not obvious, e.g. relations between non-neighboring structures [Allasonnière 2011]. By investigating these relations we might find new anatomical knowledge that improves diagnostics for patients.

1.1.2 Intersubject Anatomical Variability – Big Data

The term ‘Big Data’ has recently been coined in popular science magazines and newspapers to define a new discipline in the realm of statistics and artificial intelligence (particularly machine learning). The term defines the analysis of large amounts of data to find patterns that help predict future events or to understand relationships between entities within a dataset. The rise of this new discipline is fueled by an increasing amount of data available and the increase in computational resources.

According to an article¹ in the New York Times, the prediction power of Big Data shows promise in fields like public health, economic development and economic forecasting. It is for instance reported that researchers found an increase of Google search requests for terms like “flu symptoms” and “flu treatments” a few weeks before an increasing number of flu patients visit the emergency rooms of hospitals. Another example of its growing influence is the new initiative created by the United Nations, called the Global Pulse, to focus on Big Data for global development. Global Pulse will analyze messages in social networks and text messages to predict job losses, spending reductions or disease outbreaks in different regions of the world.

Big Data can also be associated with medical imaging data to compare pathological versus control subjects or groups, to track the evaluation of a disease or to build anatomical atlases (representation of an average organ with annotation from medical experts). At ISTB², strong efforts have been taken to build a large database

¹Steve Lohr, “The Age of Big Data”, New York Times, February 11, 2012

²Institute for Surgical Technology and Biomechanics, University of Bern

of CT³ images of bones. This has led to a database of a total of approximately 2800 images with different anatomical structures: head, mandible, pelvis, femur, tibia, fibula, patella, humerus and full body. If we assume that one image is 100MB, this equals to 280GB of imaging data.

This is still a small sample size dataset compared to other Big Data applications. For instance, the number of Twitter message per day reached 340 million by 2012, according to an announcement⁴ by the company. In addition to the smaller sample size in medical image datasets, we need to select a subset of images for a specific clinical application, and for the validation of new methods we need manually segmented or otherwise annotated data, which narrows down the number of images actually used in a study even more. In this manuscript, we focus on the following dataset:

- 328 CT images of tibia bones
- 309 CT images of femur bones
- 43 CT images of mandible bones

These datasets give us the opportunity to answer clinical questions in the context of symmetric assessment of tibias and femurs, biomechanics of femurs, allograft selection for femurs, implant design for mandibles and regression models for orthopaedic research. Two computing clusters enable us to run experiments on this amount of data:

- dream at INRIA Sophia Antipolis, France
- obelix at University of Bern, Switzerland

To fully take advantage of the computing power available, we believe that current algorithmic medical image approaches will move towards a more probabilistic approach, for instance the usage of Monte Carlo simulations might become an important part of our field. In this thesis, we take first steps towards that goal by introducing a model that could be furthered optimized by Monte Carlo simulations. We mention some ideas along this direction of research in Chapter 5. This is also supported by the current trend of CT and MR image acquisition. In a recent article⁵ in the New York Times, it was reported that the number of CTs taken by patients tripled over the past 14 years (1996 to 2010) to 14.9%, while the number of MRIs⁶ quadrupled to 6.5%.

Big Data enables us to move the FMA from a description of the average anatomical structure, granularity and relations towards a description of the variability of these terms in a population of subjects.

³Computed Tomography

⁴“Twitter turns six”, March 21, 2012

⁵Alastair Gee, “Radiation Concerns Rise With Patients’ Exposure”, June 12, 2012

⁶Magnetic Resonance Imaging

1.2 Modeling of the Human Anatomy

To analyze the dataset described in the previous section, the formal definition of FMA helps to focus on the important requirements for anatomical modeling. As explained in Section 1.1, we need a representation that is granular (description at different levels of detail), captures different parts and describes how the different parts are related to each other.

In this section, we try to analyze the problem of anatomical modeling from three different points of view.

1.2.1 An Engineer's View: Algorithmic Modeling of Organs

In the field of medical image analysis the anatomy is modeled via landmarks (points, curves, surfaces and skeletons) or via the entire image domain. In the case of point landmarks, a comprehensive introduction is given in [Dryden 1998]. The landmarks in these models are typically labeled manually or extracted using feature detection methods. For the modeling of curves, surfaces and the entire image domain, geometrical deformations are the underlying concept to warp one anatomy towards another. The reference or template serves as the object that is to be deformed into a target or subject anatomy. The geometrical deformation from a reference is used in a pairwise setting. For a groupwise setting a template is chosen and subjects are deformed towards it. The field concerned with finding geometrical deformations for the anatomy is called medical image registration. There are at least two cases that can be distinguished in registration: registration of images from the same subject, and intersubject registration. Registration methods deform curves, surfaces [Vaillant 2005, Glaunès 2008, Durrleman 2008, Durrleman 2009, Durrleman 2011], skeletons [Pizer 2003, Siddiqi 2008], or the entire image domain [Klein 2009].

Figure 1.2 visualizes an example of a geometrical diffeomorphic deformation obtained with the log-demons algorithm [Vercauteren 2009]. Each curve represents the trajectory along which the deformation occurs, and is generated by taking the Exponential map from a stationary velocity field (SVF) at different time points [Arsigny 2006, Ashburner 2007, Hernandez 2007]. A diffeomorphic deformation and its inverse are smooth. The smoothness property guarantees no overlaps or holes in the deformation and its inverse. Thus, we assume that the anatomies under study have the same topology. More details on diffeomorphisms will be given in Chapter 2.

This is one example of a registration, but without an underlining physical model it is unclear which registration method to choose. What most registration methods have in common are the formulation of a parameterization of the geometrical deformation, a regularization and an optimization method to find a local solution for the geometric deformation. In [Klein 2009], a recent overview of popular registration methods compares their performance on a common dataset of brain MR images.

The observation of deformations like the one shown in Fig. 1.2, indicates a connection to the work on locally affine transformations. Locally affine transformations (also called polyaffine transformations) parameterize diffeomorphisms by spatially

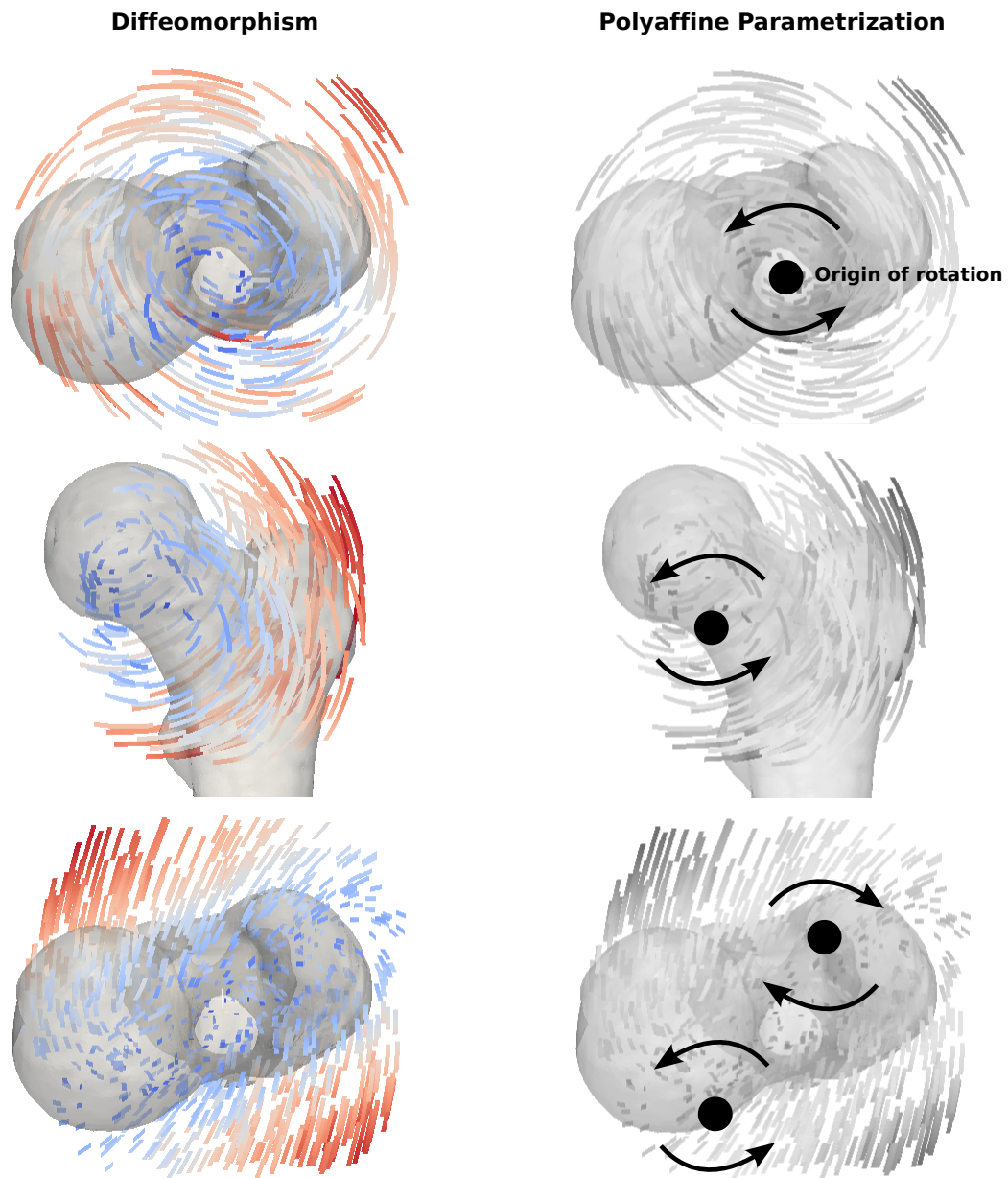


Figure 1.2: Three typical intersubject geometrical deformations on the femoral head. Each curve represents the trajectory along which the deformation occurs. For visualization purposes we picked a random set of curves from the equally spaced vector field. The color code indicates the length of the curve. **Left:** A parametrization of the deformation in terms of a vector field. **Right:** A parameterization of the deformation in terms of local rotations.

weighted logarithms of affine transformations. This kind of parameterization was pioneered in [Arsigny 2005, Commowick 2008, Arsigny 2009]. Figure 1.2, illustrates a possible parametrization with rotations about one or multiple points. In addition to a low dimensional representation of diffeomorphisms, it opens new ways of thinking about geometric deformations and their estimation. In this Ph.D. thesis, this parametrization led to a new statistical estimation of geometrical deformations (Chapter 3).

Recent developments in registration are concerned with a simultaneous registration of different anatomical scales [Risser 2010, Sommer 2011b, Sommer 2011a, Buerger 2011, Zhang 2011]. This is a very interesting problem, since it address the current lack of intermediate steps between a global deformation obtained from rigid or affine registrations, and a local registration obtained from non-linear registrations. Classical registration methods are divided into two steps, a global alignment (e.g. rigid and affine transformations) and a non-linear transformations (e.g. diffeomorphic deformations). This strategy turns out to be suboptimal for certain anatomical structure. In the case of femur bones, we improved registration results by introducing an intermediate step comprising of a registration of the three major parts of the bone (head, shaft and condyles) prior to non-linear registration (Chapter 2). In the case of mandible bones, we introduced a new type of hierarchical tree scheme that is able to capture volumetric shape variability encountered at different anatomical scales (e.g. left and right side, or teeth) (Chapter 2).

1.2.2 A Statistician's View: Modeling of the Variability

The first step in a statistical analysis of intersubject template to subject deformations could contain the computation of the mean and the covariance structure. For deformations parameterized with SVFs (example shown in the previous section), standard multivariate methods to compute the sample mean and covariance matrix can be used. Other parametrizations of deformations require more sophisticated non-Euclidean computations [Ma 2008, Bigot 2009, Durrleman 2009]. Recently Bayesian interpretations have been introduced to statistical model deformations [Ashburner 1997, Allasonnière 2007, Allasonnière 2010]. Here, we focus on SVFs to highlight some underlining difficulties.

The registration methods compared in [Klein 2009] have a degree of freedom between 10^6 and $28 \cdot 10^9$. The dataset that was used for the comparison consists of 80 MRI images of the brain. Statisticians refer to these kind of problems as High Dimension, Low Sample Size (HDLSS) problems. One way to study the covariance structure of a dataset is to extract its mode of variation using principal component analysis (PCA). In the statistical community, PCA is studied in the HDLSS settings through asymptotic analysis. In contrast to classical asymptotics, where the number of dimensions are fixed and the number of samples go to infinity, in HDLSS the number of samples are fixed while the number of dimensions go to infinity. Even if it is possible to show that the PCA in a HDLSS setting gives robust estimates of the eigenvalues and eigenvectors [Jung 2012], we are confronted with an interpretability

problem.

Let us take the case of statistical shape models (SSMs). The PCA is performed on the deformations that are found with non-linear registration, as shown for instance in [Cootes 2001]. We further assume that we can robustly estimate the first mode. The estimated mode will most likely be a mixture of non-local shape effects. It is unclear how to interpret the linear combination of non-local shape effects. So it seems that this tool is not ideal to statistically analyze geometrical deformations. To localize shape effects, we present in this Ph.D. thesis the structuring of geometrical deformations in trees to handle anatomical granularity, and to preserve the tree structure inherent in the definitions of the FMA.

In the statistics community, the importance of trees has been growing in recent years. There have recently been two workshops very closely linked to statistical problems on trees. At SAMSI⁷, a 12-month program on the “Analysis of Object Data” was organized during the year 2010 and 2011. The program had three research foci: Euclidean data (i.e., vectors of real numbers), mildly non-Euclidean data (i.e. points on a manifold and shapes) and strongly non-Euclidean data (i.e. tree or graph structured objects). One working group led by J.S. Marron was entirely dedicated to trees in statistics. The topics discussed were, combinatorics, folded Euclidean (maybe best known in the study of Phylogenetic Trees) and Dyck Path, among others. The other recent workshop was on “Statistics, Geometry, and Combinatorics on Stratified Spaces Arising from Biological Problems” and organized at the MBI⁸. Topics presented during this workshop were general surveys of stratified spaces, the geometry and statistics of geometric trees, towards statistical topology, among others.

Developments in this field also referred to as “stratified statistics” take their cue from more classical geometrical statistics, where data points are sampled from smooth manifolds, or from neighborhoods of embedded manifolds. Now, however, interesting algebraic geometry and combinatorics join the mix. Asymptotics on such spaces are governed not only by their local structure, but also by global topology (of the space and the data).

The tree model presented in this Ph.D. thesis has yet to fully take advantage of these recent developments in statistics. In Chapter 5, we outline ideas on how to use the synergies between medical image analysis and stratified statistics. Some interesting works on this topic can be found in [Metzen 2009, Aydin 2009, Lo 2010, Owen 2011, Feragen 2011, Aydin 2012].

1.2.3 A Clinician’s View: Intelligibility of Models

The link between the mathematical modeling of the anatomy and the clinician is challenging. The more sophisticated our models become the less likely it is that clinicians take the time to understand them. If they do not understand the models then they are less likely to be used in clinical applications. This subtle balance

⁷Statistical and Applied Mathematical Sciences Institute in NC, USA

⁸Mathematical Biosciences Institute, The Ohio State University, OH, USA

between model complexity and intelligibility for clinician is a crucial problem in medical image analysis.

We believe that a formulation of the anatomy in terms of tree-structured regions provides a good compromise. This is motivated by the online register of the AO foundation (describe in more details in Chapter 2). The online register uses a region-based classification scheme to guide surgeons through major steps of mandible reconstructive surgery ranging from diagnosis, selection of the optimal surgical approach, to aftercare treatment. On a more abstract level, the regions build the basis of FMA described in the beginning of this chapter.

In this Ph.D. thesis, we present such a model developed in close collaboration with our clinical partners. This collaboration with clinicians allowed us to explore a wide range of clinical applications (Chapter 4), and gave us a direct feedback on problems such as intelligibility of our methods. Together with Serena Bonaretti, University of Bern, we presented works in biomechanics [Bonaretti 2010, Bonaretti 2011]. Work on allograft selection was conducted in collaboration with Lucas Ritacco, Italian Hospital of Buenos Aires, Argentina [Ritacco 2012]. With Habib Bou-Sleiman, University of Bern, we presented works on implant bending and screw placement [Bou-Sleiman 2011, Bou-Sleiman 2012]. In collaboration with Remi Blanc, ETH Zurich, we studied conditional shape models to regress surface shapes of femur bones from clinical variables [Blanc 2009, Blanc 2012]. For cardio-applications we collaborated with Kristin McLeod, Asclepios Project, INRIA Sophia Antipolis [McLeod 2012].

1.3 Structure of the Manuscript and Contributions

Chapter 2: This chapter builds the foundation of this thesis by introducing a link between anatomical regions and intersubject deformations, and illustrates results on femur and mandible bones. This is accomplished with a new basis for stationary velocity fields with close links to anatomical substructures. We provide a hierarchical and multiscale tree structure for polyaffine transformations that can be efficiently optimized with the log-demons. With our new approach, we take a first step towards a unified algorithmic registration framework for a "continuous" subdivision of deformations across scales. This chapter was published as a journal article in Medical Image Analysis [Seiler 2012c]. The journal article builds upon two published conference papers in MICCAI and SPIE Medical Imaging [Seiler 2011b, Seiler 2011a].

Chapter 3: Here we introduce a statistical formulation of the method presented in Chapter 2. We introduce a General Linear Model (GLM) for multiscale intersubject deformations. This allows us to describe polyaffine deformations in a generative statistical model. In this model, we can incorporate deformation statistics as a prior in a Bayesian setting, enabling simultaneous estimation of multiscale deformations. We show how the maximum a posteriori probability of polyaffine transformation can be computed to obtain optimal parameter.

We improve registration robustness and accuracy with respect to registrations without prior. To the best of our knowledge, this is the first time that a prior at the group level in polyaffine registration is presented. This chapter is to be submitted as a journal article in IEEE Transactions on Medical Imaging [Seiler 2012b]. The journal article builds upon the published conference paper in MICCAI [Seiler 2012d].

Chapter 4: The development of the methodology presented in the previous two chapters is driven by applications in seven clinical settings: Symmetric assessment of tibias and femurs [Seiler 2009b], regression of geometrical deformations in femurs [Seiler 2010b], biomechanics of femurs [Bonaretti 2011, Bonaretti 2010], allograft selection for femurs [Ritacco 2012], implant design for mandibles [Bou-Sleiman 2012], prediction of bone surface for orthopaedic research [Blanc 2009, Blanc 2012] and heart modeling [McLeod 2012]. This chapter shows results in these clinical settings and summarizes works that we co-authored using the standard log-demons and the methodology presented in Chapter 2.

Chapter 5: In the last chapter, we make an overall conclusion of this manuscript and give our perspective on interesting open questions. We believe the work on statistics of trees in the context of Phylogenetic Trees has the potential to provide interesting insights in polyaffine transformation trees. We give a short introduction to this topic in Appendix A.

1.4 List of Publications and Awards

Journal Articles

- [Seiler 2012b] C. Seiler, M. Reyes and X. Pennec, A Generative Statistical Model for Multiscale Diffeomorphic Deformations, To be submitted to IEEE Transactions on Medical Imaging (TMI). Chapter 3.
- [Seiler 2012c] C. Seiler, X. Pennec and M. Reyes, Capturing the Multiscale Anatomical Shape Variability with Polyaffine Transformation Trees, Medical Image Analysis (MedIA), 2012. Chapter 2.
- [Seiler 2012a] C. Seiler, A. Gazdhar, M. Reyes, L.M. Benneker, T. Geiser, K.A. Siebenrock, B. Gantenbein-Ritter, Time-Lapse Microscopy and Classification of 2D Human Mesenchymal Stem Cells Based on Cell Shape Picks Up Myogenic from Osteogenic and Adipogenic Differentiation, Journal of Tissue Engineering and Regenerative Medicine, 2012. Not included in the thesis.
- [Blanc 2012] R. Blanc, C. Seiler, G. Székely, L. Nolte, M. Reyes, Statistical Model Based Shape Prediction from a Combination of Direct Observations and Various Surrogates. Application to Orthopaedic Research, Medical Image Analysis (MedIA), 2012. Summarized in Chapter 4.

- [Ritacco 2012] L. Ritacco, C. Seiler, G. Farfalli, L. Nolte, M. Reyes, D. Muscolo and L. Tinao, Validity of an Automatic Measure Protocol in Distal Femur for Allograft Selection from a Three-Dimensional Virtual Bone Bank System, Cell and Tissue Banking, 2012. Summarized in Chapter 4.

Book Chapter

- [Seiler 2009a] C. Seiler, P. Büchler, L.-P. Nolte, R. Paulsen and M. Reyes, Hierarchical Markov Random Fields Applied to Model Soft Tissue Deformations on Graphics Hardware, Recent Advances in the 3D Physiological Human (N. Magnenat-Thalmann, J. J. Zhang, and D. D. Feng, eds.), Chapter 9, pp. 133-148, Springer London, 2009. Not included in the thesis.

Selective Peer-Reviewed Conference Papers

- [Seiler 2012d] C. Seiler, X. Pennec and M. Reyes, Simultaneous Multiscale Polyaffine Registration by Incorporating Deformation Statistics, MICCAI, Nice, France, October 2012. (Acceptance rate: 248 of 779 papers = 32%). Was extended to the journal article [Seiler 2012b], Chapter 3.
- [Seiler 2011a] C. Seiler, X. Pennec and M. Reyes, Geometry-Aware Multi-scale Image Registration Via OBBTree-Based Polyaffine Log-Demons, MICCAI, Toronto, Canada, September 2011. Young Scientist Award and Student Travel Award. (Oral podium presentation, acceptance rate: 34 of 819 papers = 4.2%) Was extended to the journal article [Seiler 2012c], Chapter 2.
- [Bou-Sleiman 2012] H. Bou-Sleiman, C. Seiler, T. Iizuka, L. Nolte, M. Reyes, Population-Based Design of Mandibular Plates Based on Bone Quality and Morphology, MICCAI, Nice, France, October 2012. (Acceptance rate: 248 of 779 papers = 32%). Summarized in Chapter 4.
- [Blanc 2009] R. Blanc, M. Reyes, C. Seiler and G. Székely, Conditional Variability of Statistical Shape Models Based on Surrogate Variables, MICCAI, vol. 5762, pp. 84-91, London, UK, September 2009. (Acceptance rate: 32%). Summarized in Chapter 4.

Other Conference and Workshop Papers

- [Seiler 2011b] C. Seiler, X. Pennec, L. Ritacco and M. Reyes, Femur Specific Polyaffine Model to Regularize the Log-domain Demons Registration, SPIE Medical Imaging (Image Processing), Orlando, USA, February 2011. Was extended to the journal article [Seiler 2012c], Chapter 2.
- [Seiler 2010b] C. Seiler, X. Pennec and M. Reyes, Parametric Regression of 3D Medical Images Through the Exploration of Non-Parametric Regression Models, ISBI, Rotterdam, The Netherlands, April 2010. Section 4.2.

- [McLeod 2012] K. McLeod, C. Seiler, A. Prakosa, M. Sermesant, X. Pennec, A Near-Incompressible Poly-Affine Motion Model for Cardiac Function Analysis, STATCOM, MICCAI Workshop, Nice, France, October 2012. Summarized in Chapter 4.
- [Bonaretti 2011] S. Bonaretti, C. Seiler, C. Boichon, P. Büchler, M. Reyes, Mesh-Based vs. Image-Based Statistical Model of Appearance of the Human Femur: A Preliminary Comparison Study for the Creation of Finite Element Meshes, MeshMed, MICCAI Workshop, Toronto, Canada, September 2011. Summarized in Chapter 4.
- [Bauer 2010] S. Bauer, C. Seiler, T. Bardyn, P. Büchler, M. Reyes, Atlas-Based Segmentation of Brain Tumor Images Using a Markov Random Field-Based Tumor Growth Model and Non-Rigid Registration, EMBC, Buenos Aires, Argentina, September 2010. Not included in the thesis.
- [Bonaretti 2010] S. Bonaretti, M. Kistler, C. Seiler, M. Reyes and P. Büchler, Combined Statistical Model of Bone Shape and Mechanical Properties for Bone and Implant Modeling, CMBBE, Valencia, Spain, February 2010. Summarized in Chapter 4.

Conference Abstracts

- [Seiler 2010a] C. Seiler, A. Gazdhar, T. Geiser, M. Reyes and B. Gantenbein-Ritter, Mesenchymal Stem Cell Classification During Differentiation Based on Shape Information, TERMIS, Galway, Ireland, June 2010. Not included in the thesis.
- [Seiler 2009b] C. Seiler, S. Weber, W. Schmidt, F. Fischer, N. Reimers and M. Reyes, Automatic Landmark Propagation for Left and Right Symmetry Assessment of Tibia and Femur: A Computational Anatomy Based Approach, CAOS, Boston, USA, June 2009. Section 4.1.

Software

An ITK implementation of the presented work is available on github:

- [git://github.com/ChristofSeiler/PolyaffineTransformationTrees.git](https://github.com/ChristofSeiler/PolyaffineTransformationTrees.git)

Awards and Invitations

- The paper “Geometry-Aware Multiscale Image Registration Via OBBTree-Based Polyaffine Log-Demons” was awarded the “Young Scientist Award” at the MICCAI conference 2011 in Toronto, CA. (top 5 out of the majority of all 819 papers written by PhD students and postdocs)

- Invitation to submit a significantly extended and augmented version of the paper “Geometry-Aware Multiscale Image Registration Via OBBTree-Based Polyaffine Log-Demons” to Medical Image Analysis (MedIA) for the Special Issue (12 out of 819 papers = 1.5% were invited)
- The paper “Geometry-Aware Multiscale Image Registration Via OBBTree-Based Polyaffine Log-Demons” was awarded the “Student Travel Award” at the MICCAI conference 2011 in Toronto, CA.

Capturing the Multiscale Anatomical Shape Variability with Polyaffine Transformation Trees

This chapter was published as a journal article in [Seiler 2012c]. The journal article builds upon two published conference papers [Seiler 2011b, Seiler 2011a].

Abstract

Mandible fractures are classified depending on their location. In clinical practice, locations are grouped into regions at different scales according to anatomical, functional and aesthetic considerations. Implant design aims at defining the optimal implant for each patient. Emerging population-based techniques analyze the anatomical variability across a population and perform statistical analysis to identify an optimal set of implants. Current efforts are focused on finding clusters of patients with similar characteristics and designing one implant for each cluster. Ideally, the description of anatomical variability is directly connected to the clinical regions. This connection is what we present here, by introducing a new registration method that builds upon a tree of locally affine transformations that describes variability at different scales. We assess the accuracy of our method on 146 CT images of femurs. Two medical experts provide the ground truth by manually measuring six landmarks. We illustrate the clinical importance of our method by clustering 43 CT images of mandibles for implant design. The presented method does not require any application-specific input, which makes it attractive for the analysis of other multiscale anatomical structures. At the core of our new method lays the introduction of a new basis for stationary velocity fields. This basis has very close links to anatomical substructures. In the future, this method has the potential to discover the hidden and possibly sparse structure of the anatomy.

Contents

2.1	Implant Design for Mandible Fractures	17
2.1.1	Clinical Problem	17
2.1.2	Methodological Framework	18
2.2	Projection of SVFs Onto the Linear Space of LEPTs	20
2.2.1	Exponential and Logarithm of Matrices	22
2.2.2	Exponential and Logarithm of Vector Fields	23
2.2.3	Our Contribution: Linear Projection	23
2.2.4	New Metric on Stationary Velocity Fields	24
2.3	Hierarchical Structuring of Polyaffine Transformations in Trees	24
2.4	Anatomy-Driven Definition of Regions	25
2.4.1	OBBTree on Contour Extracted from Template Image	25
2.4.2	OBBTree on Feature Image Extracted from Template Image	26
2.5	Estimation of Transformations	27
2.5.1	Log-Demons Algorithm	28
2.5.2	Integration of the Estimation into the Log-Demons	29
2.6	Femur Bone Registration with Manual Regions	30
2.6.1	Clinical Problem	30
2.6.2	Special Case of a Polyaffine Transformation Tree	31
2.6.3	Validation with Landmark Measurements by Medical Experts	31
2.7	Mandible Bone Registration with Hierarchical Regions	32
2.7.1	Weights Derived from Oriented Bounding Boxes	35
2.7.2	Estimation of the Transformation Tree	35
2.7.3	Analysis of Obtained Tree Transformations	38
2.8	Implant Design Based on Statistical Analysis	38
2.8.1	Link Between Clinical and Data-Driven Regions	38
2.8.2	Clustering of Polyaffine Parameters for Selected Regions	40
2.9	Discussion and Conclusion	40

2.1 Implant Design for Mandible Fractures

2.1.1 Clinical Problem

Mandibular fractures most commonly result from facial trauma, with close to half of the patients requiring surgical repair [Ellis 1985]. A majority of 75% of fractures occur in males aged between 20 and 30 [Ellis 1985, Moore 1985], and are often caused by physical assault. Other causes of fractures include motor vehicle collisions, falls, and sports-related injury [Craig 2008, Kovan 2008]. For all these cases surgical repair proves most effective, with the goal of recovering the anatomical structure prior to the injury and thus restoring normal function. To reach this goal the surgeon places wires or implants at the fracture site, so that the natural fusion of separated bone pieces restores the prior structure [Fedok 1998] as closely as possible. A correct repair aligns teeth for food intake, and restores the patient's aesthetics.

In [Urken 1991], the authors propose a classification scheme for mandibles based on regions according to anatomical, functional and aesthetic considerations. The online register www.aofoundation.org uses the same classification (Fig. 2.1) to guide surgeons through the major steps of mandible reconstructive surgery ranging from diagnosis, selection of the optimal surgical approach, to aftercare treatment. According to [Moore 1985], the rate of fracture incidence for each of the classified region is as follows: "Symphyseal and parasymphyseal" region 19%, "body" 24%, "angle and ramus" 40%, "condylar process and head" 16%, and "coronoid" 1%. In addition to this classification scheme, the mandible can be subdivided even further into smaller regions, e.g. one region for each tooth. In the image space, this subdivision can theoretically be performed up to the voxel level, where coarser levels enclosed finer ones, representing a hierarchy of regions that can be organized in a tree-like fashion. As the regions become more fine, it is harder to find a consensus among clinicians on the size, shape and location of the region.

Recent work on biomechanical analysis of implants indicates that geometry and topology of implants are crucial to fracture stability. In [Lovald 2009], it was shown that implants optimized for the "body" region, (Fig. 2.1), have fracture strain of 69% to 59% and implant stress of 34% to 27% with respect to smaller standard implants, while minimizing patient intrusion by saving 55% of implanted volume of larger standard implants. The same authors presented results on implant optimization of the "symphyseal and parasymphyseal" region with similar results [Lovald 2010]. In [Cervantes 2012], flexible implants that allow the surgeon to adjust the geometry after bone fixation are presented. Instead of pre-manufacturing patient specific implants, there have been several works on population-based designs, for femurs [Kozic 2010, Bou-Sleiman 2011, Bonaretti 2011] and mandibles [Metzger 2011, Bou-Sleiman 2012]. In these approaches, the population is stratified into several sub-populations according to morphological differences or meta-information (e.g. gender, age, etc.). None of the aforementioned population-based approaches consider the bone mineral density in addition to the surface geometry, even though [Lovald 2009, Lovald 2010] reported its importance to achieve optimal

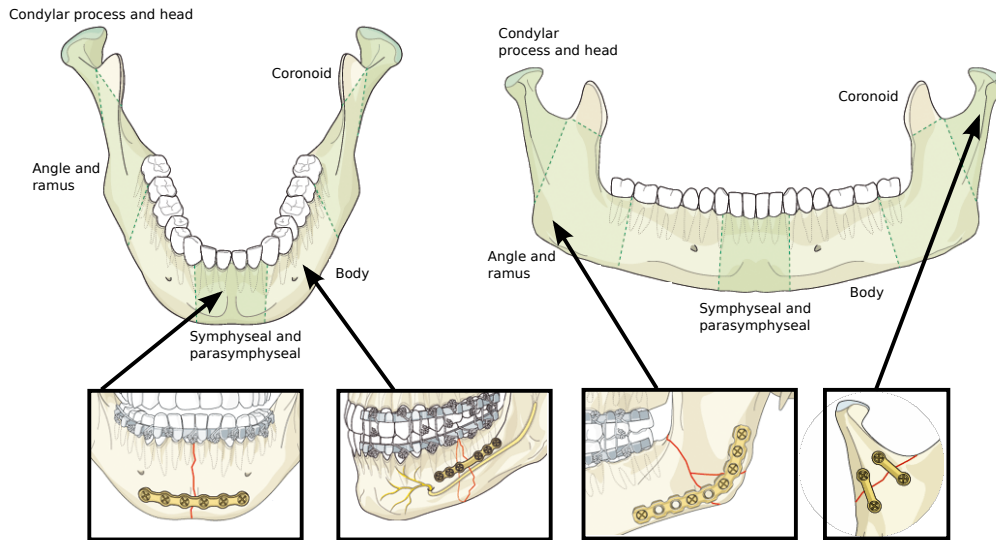


Figure 2.1: Subdivision of mandible into anatomical regions proposed by the AO foundation to classify fractures for reconstructive surgery. Implants at four different anatomical sites are shown. Images source: www.aofoundation.org.

design and placement of screws.

2.1.2 Methodological Framework

The economical cost of patient specific implants makes this approach impracticable at the moment, hence we focus on an intermediate goal: population-based implant design. Common key steps to population-based design [Kozic 2010, Metzger 2011, Bou-Sleiman 2011, Bou-Sleiman 2012] are registration to capture shape variability as encountered in a population and statistical analysis of the registration results, performed subsequently and independently. As mentioned, registration approaches for implant design should consider not only bone surface information, but also volumetric information describing the bone density distribution, which is needed to compute best location and orientation of the placement of screws to fixate implants.

It is a common practice to use principal component analysis (PCA) for dimensionality reduction and extraction of main modes of variation from deformations obtained through non-linear registration. However, due to the global nature of PCA only ad-hoc heuristics to decompose the anatomical shape into localized regions (as shown in Fig. 2.1) of interest are available, further it is unclear how to interpret the linear combination of different mixtures of shape effects. We therefore conclude that an intelligible link between PCA shape models and implant design for specific regions is missing.

M-reps [Pizer 2003, Siddiqi 2008] offer remedy for these kind of issues, by model-

ing surface shapes locally, thus providing a better link between model and clinically motivated regions. Focus on these regions of interest, as opposed to a full non-linear registration, potentially increases the robustness (small number of parameters) and intelligibility (direct connection between regions in a clinical context and shape modeling) of the registration. Unfortunately, due to the fact that the representation is surface-only, volumetric information cannot be included into the analysis to reconstruct bone density distributions.

Therefore we focus on another approach that allows for region-based local description of shape and volumetric information: locally affine transformations, also called polyaffine transformations. Polyaffine transformations were introduced in [Arsigny 2005] to fuse locally rigid and affine transformations into a diffeomorphism, and revisited in [Arsigny 2009] to obtain faster numerical algorithms. An efficient registration algorithm using approximations of polyaffine transformations was presented in [Commowick 2008]. In [Martín-Fernández 2009] an extension to articulated structures was presented, which considers weights (defining the influence of each region) fixed at landmark positions along a manually defined skeleton. Other recent work includes [Zhuang 2010], where a Locally Affine Registration Method (LARM) is developed for cardiac MR images. LARMS works by fusing the affine transformations directly, which can cause non-diffeomorphic transformations. These non-diffeomorphic cases are prevented through two additional regularization steps. The authors define regions that are important substructures of the heart and use LARM as an initialization to robustify the subsequent non-linear registration step. In [Seiler 2011b], we presented a polyaffine-regularized log-demons algorithm for femur bone registration with manually fixed weights. However, we believe that defining the regions for the locally affine deformations should not be left to the user, because this is subjective and reduces reusability. This becomes even more evident in the case of a multiscale representation of the geometry, where the definition of regions and their division process is not straightforward and time consuming.

To consider more complex shapes and foster reusability, [Buerger 2011] presented a multiscale approach with affine regions defined using a data-driven approach. The method splits rectangular shaped regions, which are aligned along the image directions, only if certain conditions are met. [Taquet 2011] iteratively optimizes between affine parameters and anchor positions (center of regions) estimation, through an expectation maximization approach. The weights are estimated with a Kriging estimator instead of the usual Gaussian functions. In [Zhang 2011], Log-Euclidean Polyaffine Transformations (LEPT) are employed to register multi-modal cardiac sequences in an elaborate scheme. The algorithm iteratively adds new uniform Gaussian weighted regions with different spatial position (mean parameter) and influence (variance parameter) until a mutual information-based criterion is satisfied. The authors in [Freiman 2011] showed how the standard diffeomorphic demons (not the log-demons) could be used to enforce an inhomogeneous regularization using a local affine fitting at each voxel of the image. Even though these methods are very promising, the link between the clinical regions (Fig. 2.1) and the regions found by these algorithms, is either constrained by aligned rectangular shaped regions

or spherical weights [Buerger 2011, Zhang 2011], or produce an intractable number (around 500 or one region per voxel) of regions [Taquet 2011, Freiman 2011].

We present here a new approach with emphasis on interpretability of regions in terms of the clinical requirements (as defined in Fig. 2.1), by introducing a hierarchical multiscale tree structure that is motivated by the nature of the mandible anatomy, where regions are ordered and interact with each other in a way tractable for human understanding. Further, since we formulate a data-driven approach, our presented algorithm can be applied to other anatomical structures without modification. To accomplish this we contribute the following points:

1. Linear projection of Stationary Vector Fields (SVF) onto the space of polyaffine transformations (Section 2.2).
2. Tree structured polyaffine transformations (Section 2.3).
3. Anatomy-driven definition of regions using a hierarchy of oriented bounding boxes (Section 2.4).
4. Efficient estimation of transformation parameters with the log-demons algorithm (Section 2.5).
5. Unified algorithmic registration framework for a “continuous” subdivision of deformations across scales, see Fig. 2.2 for an illustration.

A preliminary version of this work was presented at SPIE 2011 [Seiler 2011b] and MICCAI 2011 [Seiler 2011a] conferences. Additionally, in this paper, we extend the method from surface-based to image-based definitions of regions and provide a statistical analysis of the polyaffine deformations found. In the following, we first introduce our novel way of projecting SVFs onto the space of polyaffine transformations. Second, we formulate hierarchical polyaffine transformation trees and their estimation. Third, we conduct registration experiments on manual and hierarchical regions for femur and mandible bones. Fourth, we connect the clinical problem with our newly developed methodology by showing how it can be used for clustering in the context of population-based implant design.

2.2 Projection of Stationary Velocity Fields Onto the Linear Space of Log-Euclidean Polyaffine Transformations

In this section, we describe one of our main technical contributions, the projection of Stationary Velocity Fields (SVF) onto the space of Log-Euclidean Polyaffine Transformations (LEPT). This new projection allows us to estimate LEPTs by using the very efficient log-demons algorithm [Vercauteren 2009]. This projection is independent of the registration problem. It can be considered as a new basis for SVFs, that can be closely linked to anatomical substructures (e.g. left and right side of

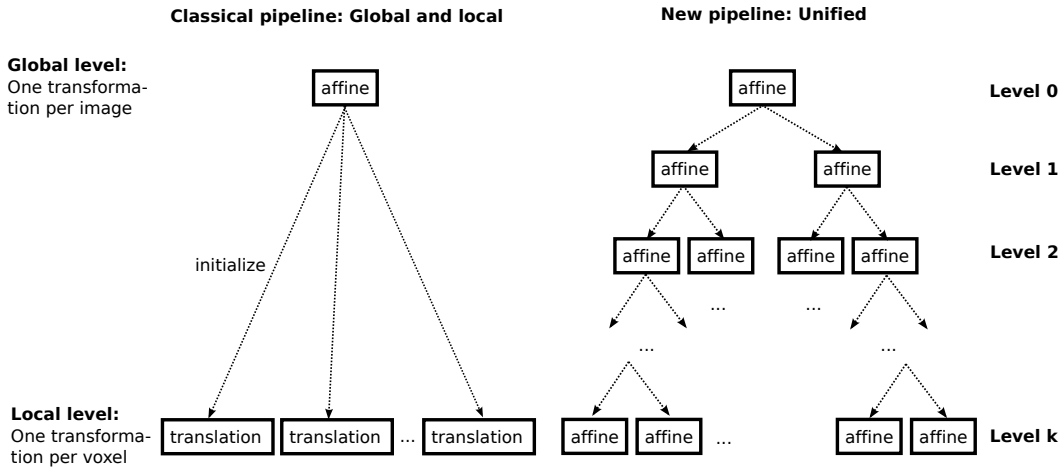


Figure 2.2: Comparison of classical and newly proposed image registration pipeline. In most classical approaches, the non-linear registration method is initialized with an affine registration performed in advance, clearly separating the two steps. In our new method we propose to move from global to local transformations by subdividing the images into smaller regions, thus providing a smooth transition, while preserving diffeomorphic deformations.

the mandible bone). In Section 2.5, we show how it can be used in the context of registration.

In [Arsigny 2005], the authors introduced polyrigid and polyaffine transformations in the context of medical image analysis. Their works showed how to obtain diffeomorphic deformations by fusing transformations using ordinary differential equations (ODE). The estimation of the transformation parameters by numerically solving the ODEs was computationally expensive and therefore hard to use in practice. To tackle the computational burden the same authors introduced the fast Log-Euclidean polyaffine framework [Arsigny 2009]. The authors redefined the problem by relying on the logarithms of the transformations. These logarithms are defined in the theory of Lie groups. In practice, this results in computations of these logarithms via matrix logarithms. The practical relevance of this theoretical reformulation of the problem was exploited in [Commowick 2008]. In a first step, block-matching was used to estimate each affine transformation for a predefined region. In a second step, the algorithm fused the separately computed affine transformation using the Log-Euclidean polyaffine framework to ensure invertibility. The polyaffine transformation is not optimized but rather used as a regularization to combine affine transformations. In this paper, we present a way to efficiently, directly and jointly estimate polyaffine transformation parameters for all regions in one step.

The novelty of our work is to take advantage of the efficiency of the log-demons

algorithm to generate iterative solutions of SVFs, which we then project onto the space of LEPTs. In this way, we constrain the domain of possible solutions to the space of LEPTs. This computation scheme is detailed in Section 2.5. In this section, we focus only on the technicalities of the projections. To fully understand the projection we first define LEPTs (which includes the matrix logarithm and the exponential of matrices in terms of Lie group theory) and SVFs (which includes the exponential map of SVFs and its inverse). Finally, we have all ingredients to define our new projection.

2.2.1 Exponential and Logarithm of Matrices

Using homogeneous coordinates, the principal logarithm of affine transformations can be computed in a simple way. The main point here is that the principal logarithm of an affine transformation A_i is represented in homogeneous coordinates by the matrix logarithm of its representation M_i . This matrix logarithm takes the following form,

$$\log \begin{pmatrix} A_i & t_i \\ 0 & 1 \end{pmatrix} = \begin{bmatrix} M_i \\ 0 \end{bmatrix},$$

where \log stands for the principal matrix logarithm, A_i is an 3×3 matrix and t_i an 3×1 vector, M_i is an 3×4 matrix and the index i can be ignored for now, it will become evident in Equation (2.2).

Using the principal logarithm of affine transformations one can associate to affine transformations a family of velocity vector fields in the following way,

$$v(x) = M_i \tilde{x}, \tag{2.1}$$

where $v(x)$ is an 3×1 and \tilde{x} is an 4×1 vector.

The logarithms of affine transformations can be computed using matrix exponentials and the ‘Scaling and Squaring’ method as shown in [Arsigny 2009]. For any square matrix, we have,

$$\exp \begin{pmatrix} M_i \\ 0 \end{pmatrix} = \exp \left(1/2^s \begin{bmatrix} M_i \\ 0 \end{bmatrix} \right)^{2^s}.$$

The key idea is that the matrix exponential is much simpler to compute for matrices close to zero. In this case, one can use only few terms of the infinite series of exponentials, since high-order terms will be completely negligible. An even better idea is to use Padé approximants, which provide excellent approximations by rational fractions of the exponential around zero with very few terms.

Exactly as for exponentials, we use ‘Inverse Scaling and Squaring’ method to compute matrix logarithms. Similarly, the idea is that logarithms are much simpler to compute for matrices close to the identity. To transform a matrix so that it is closer to the identity, the algorithm performs recursive computations of square roots, using,

$$\log \begin{pmatrix} A_i & t_i \\ 0 & 1 \end{pmatrix} = 2^s \log \left(\begin{bmatrix} A_i & t_i \\ 0 & 1 \end{bmatrix}^{1/2^s} \right).$$

Now let us introduce the LEPT for n regions with regions indexed by i . A linear combination of logarithms provides us with a SVF,

$$v_{\text{LEPT}}(x) = \sum_{i=1}^n w_i(x) M_i \tilde{x}, \quad (2.2)$$

where $w_i(x)$ are normalized weights for region i , i.e. $\forall x \in \Omega : \sum_{i=1}^n w_i(x) = 1$.

2.2.2 Exponential and Logarithm of Vector Fields

In [Arsigny 2006], the authors define the exponential $\exp(v)$ of a (smooth) vector field $v(x)$ as the flow at time 1 of the stationary ODE $\dot{x} = v(x)$. This generalizes the equivalence between one-parameter subgroups and exponential to SVFs v and diffeomorphisms ψ . This equivalence exists in the finite-dimensional case as described in the previous section. However, a proof for the existence and uniqueness of the logarithm $\log(\psi) = v$ is still an open research question. In this work we do not rely on it, since we only generate diffeomorphisms parameterized with SVFs using $\exp(v) = \psi$.

2.2.3 Our Contribution: Linear Projection

Given the velocity field v , we define the projection as the minimization of,

$$\text{proj}_M v = \underset{M}{\text{argmin}} \int_{\Omega} \lambda(x) \|v(x) - v_{\text{LEPT}}(x)\|^2 dx = \underset{M}{\text{argmin}} C(M), \quad (2.3)$$

where $M = [M_1 \dots M_n]$, and λ is a binary mask indicating background voxels (if no mask is available $\forall x \in \Omega : \lambda(x) = 1$). This is a linear least squares problem. Using the Frobenius inner product, which generalizes the dot product to matrices, $\|W\|^2 = \text{Trace}(WW^T)$, we obtain the following directional derivative (see Appendix B on details of directional derivative of matrices):

$$\begin{aligned} \partial_W C(M) &= \lim_{\varepsilon \rightarrow 0} \frac{C(M + \varepsilon W) - C(M)}{\varepsilon} \\ &= \int_{\Omega} \lambda(x) \text{Trace} \left[\left(\sum_{i=1}^n w_i(x) W_i \tilde{x} \right) \left(\sum_{i=1}^n w_i(x) M_i \tilde{x} - v(x) \right)^T \right] dx \\ &= \sum_{j=1}^n \text{Trace} \left[W_j \int_{\Omega} \lambda(x) w_j(x) \tilde{x} \left(\sum_{i=1}^n w_i(x) M_i \tilde{x} - v(x) \right)^T dx \right], \end{aligned}$$

where $w_i(x)$ are normalized weights, $\forall x \in \Omega : \sum_{i=1}^n w_i(x) = 1$. At the optimum, the directional derivative should be null in all directions W , i.e. $\partial_W C = 0$ for all matrices W . As we have $\text{Trace}(WA) = 0$ for all W iff $A = 0$, we end up with the system,

$$\sum_{j=1}^n M_j \Gamma_{ij} = B_i,$$

with

$$\Gamma_{ij} = \int_{\Omega} \lambda(x) w_i(x) w_j(x) \tilde{x} \tilde{x}^T dx, \quad (2.4)$$

$$B_i = \int_{\Omega} \lambda(x) w_i(x) v(x) \tilde{x}^T dx, \quad (2.5)$$

where Γ is symmetric and thus diagonalizable and the minimal norm solution is given by the pseudo inverse:

$$M = [M_1 \dots M_n] = B\Gamma^+. \quad (2.6)$$

2.2.4 New Metric on Stationary Velocity Fields

This new basis on SVFs gives us a new metric on SVFs,

$$\langle v_{\text{LEPT}_1}, v_{\text{LEPT}_2} \rangle_{L_2} = m_1^T G m_2, \quad (2.7)$$

where $G = \Gamma \otimes I_3$, with Γ given by Equation (2.4) from the previous section. The symbol \otimes denotes the Kronecker product, and I_3 represents the 3×3 identity matrix.

2.3 Hierarchical Structuring of Polyaffine Transformations in Trees

In this section, we assume that the weights of each region are already defined (the definition is deferred to the next section). The aim of this section is to build the tree structure.

Let us introduce the polyaffine transformation tree, which is a general formulation of [Seiler 2011b] for n regions and k levels. Let M_i^l be the i th 3×4 non null components of the matrix logarithm of affine transformations at level l and v^l be the LEPT (introduced in the previous section in Equation (2.2)) at level l :

$$v^l(x) = \sum_{i=1}^n w_i^l(x) M_i^l \tilde{x}, \quad (2.8)$$

with

$$\log \begin{pmatrix} A_i^l & t_i^l \\ 0 & 1 \end{pmatrix} = \begin{bmatrix} M_i^l \\ 0 \end{bmatrix}, \quad \tilde{x} = \begin{bmatrix} x \\ 1 \end{bmatrix},$$

where

- $v^l(x)$ is a 3×1 vector at spatial position x (3×1 vector),
- $w_i^l(x)$ are scalar weights for regions i ,
- A_i^l is the linear part (3×3 matrix) of the affine transformation,
- t_i^l is the translational part (3×1 vector) of the affine transformation.

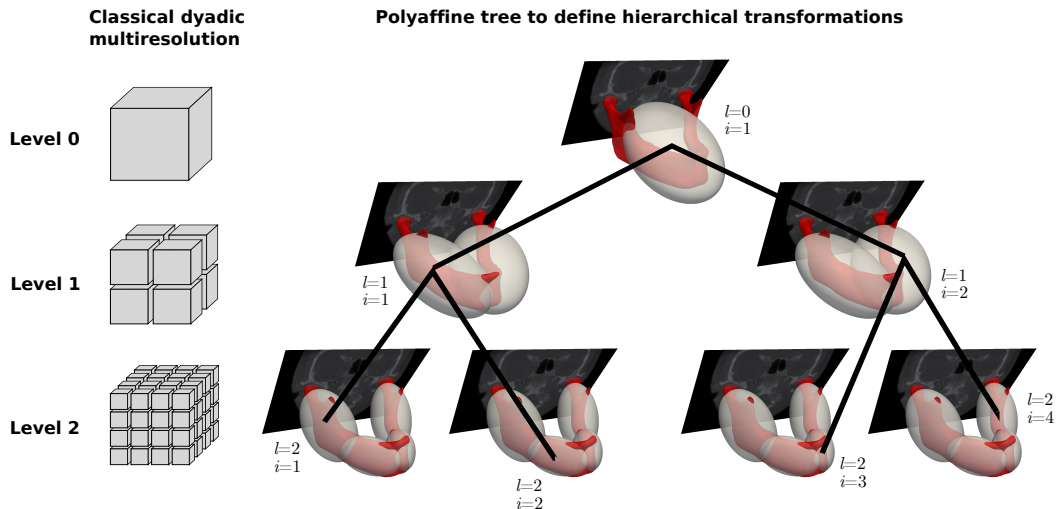


Figure 2.3: First three levels of space decomposition. **Left:** For comparison, a traditional approach using a dyadic multiresolution scheme. **Right:** Our new method decomposes the image domain using a tree of Gaussian weights. Each Gaussian weight represents one region and is visualized as one ellipsoids at σ . In addition to the contour (in red) extracted from the CT image, one CT slice is shown to stress that we work in the entire 3D image domain and not only with contours.

In Fig. 2.3, the tree structure is illustrated for the first 3 levels on mandible CT data. Each node is assigned one spatial weight function $w_i^l(x)$ and one transformation M_i^l , and each node has two child nodes, if it is not a leaf node.

The tree structure builds the basis of our work, in the next two sections we elaborate on the definition of weight parameters $w_i^l(x)$ and the estimation of transformation parameters M_i^l .

2.4 Anatomy-Driven Definition of Regions

In this section, we describe the definition of weights for each regions using a hierarchy of Oriented Bounding Boxes (OBB) for two different cases: surface contours and voxel features from the image.

2.4.1 OBBTree on Contour Extracted from Template Image

The concept of OBB has been used extensively in computer graphics to speed up ray tracing and interference detection computations. In [Gottschalk 1996], the authors presented a hierarchical version and an algorithm to compute it efficiently. An OBBTree is a hierarchy of OBB's in 3D space. Let us first consider a surface (in our case a contour of the segmented CT image). The algorithm computes OBB's via

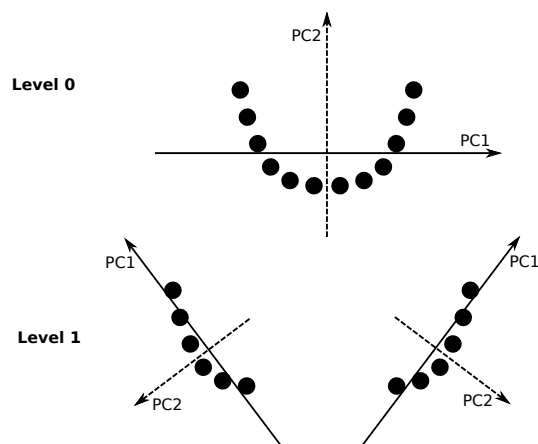


Figure 2.4: OBBTree algorithm applied to a toy example of points for level 0 and 1. At each level of the algorithm the pointset is split into two subsets along the first principle component (PC1) at the intersection with the second principle component (PC2).

Principal Component Analysis (PCA) of the vertex coordinates, which gives the orientation (principle component directions) and the extent (outmost projected point on the principle component). A refinement to avoid bias towards densely populated patches is to sample the convex hull of the vertex coordinates and approximate the analytic surface by a linear sum of all triangle areas. There are two ways of calculating the hierarchy, bottom-up and top-down. Top-down approaches start with all vertices and subdivide the points into two groups at every subsequent hierarchical level, whereas bottom-up approaches start by assigning one box per vertex and combine vertices until one box contains all vertices. We used the top-down approach, which divides the vertices into two groups by projecting the vertex coordinates onto the principle components, and uses the mean point as the group boundary. The algorithm stops once there are no more possible divisions along any component. The algorithm is illustrated in Fig. 2.4 for a toy example of a set of points. In our mandible application, points are replaced by vertices of the mandible contour.

2.4.2 OBBTree on Feature Image Extracted from Template Image

Instead of working on a subset of the image, e.g. the contour of mandible CT data as shown in the previous section, here we propose a method to use information from the entire image domain. There are many different ways to extract features from medical images and choosing the most appropriate one usually depends on the application and image modality at hand. In this work we use the following scalar feature image extracted from the template image $I_t(x)$,

$$\psi(x) = \log(1 + \|\nabla I_t(x)\|^2), \quad (2.9)$$

where $\nabla I_i(x)$ is the gradient of the image. We take the logarithm of the gradient to be more robust against small changes in intensities due to noise. As a next step we generalize the PCA of vertices to feature weighted voxels. For this purpose we introduce the feature-weighted barycenter of region Ω_i^l (discretized at voxel indices j),

$$\bar{x}_i^l = \frac{1}{\sum_{j \in \Omega_i^l} \psi(x_j)} \sum_{j \in \Omega_i^l} \psi(x_j) x_j, \quad (2.10)$$

where \bar{x}_i^l is a 3×1 vector. The feature-weighted 3×3 covariance matrix of the region is,

$$\Sigma_i^l = \frac{1}{\sum_{j \in \Omega_i^l} \psi(x_j)} \sum_{j \in \Omega_i^l} \psi(x_j) (x_j - \bar{x}_i^l)(x_j - \bar{x}_i^l)^\top. \quad (2.11)$$

We perform singular value decomposition to obtain the principle components. Following the same strategy as in the original OBBTree algorithm, the region is split at the feature-weighted mean point orthogonal to the first principal component and the splitting procedure is recursively repeated in the two new created subregions.

Finally, the spatial weight functions $w_i^l(x)$ are defined as multi-dimensional Gaussian functions,

$$w_i^l(x) = (2\pi)^{-\frac{3}{2}} |\Sigma_i^l|^{-\frac{1}{2}} \exp\left(-\frac{1}{2}(x - \bar{x}_i^l)^\top (\Sigma_i^l)^{-1} (x - \bar{x}_i^l)\right), \quad (2.12)$$

with singular value decomposition,

$$\Sigma_i^l = V_i^l (\alpha S_i^l)^2 (V_i^l)^\top, \quad (2.13)$$

where

- V_i^l is a 3×3 rotation matrix describing the orientation,
- S_i^l is a 3×3 diagonal matrix of eigenvalues describing the scaling,
- α is a scalar representing the scaling parameter to control the variance in all three directions and thus the influence of regions and its neighbors. This parameter α is to be defined by the user and controls the smoothness of the deformation v^l .

OBBTree algorithms on contours are a special case of the presented feature image-based algorithm, when $\forall x \in C : \psi(x) = 1, \forall x \notin C : \psi(x) = 0$, where C is the mandible contour.

2.5 Estimation of Transformations

Up to now, we have defined a hierarchical tree of parametric deformations which is well fitted to the anatomy that we investigate. We now need a method to estimate these parameters. In this section, we describe the basics of the log-demons algorithm and how it is used to estimate polyaffine transformations. The main idea is to iteratively find the optimal polyaffine transformation tree that describes the correspondences found by the log-demons algorithm.

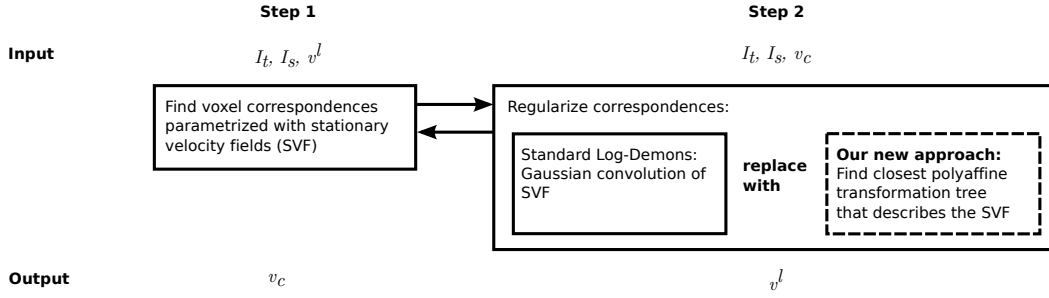


Figure 2.5: A schematic overview of the log-demons algorithm. The log-demons consists of two major steps: correspondence finding and regularization. The polyaffine transformation trees are estimated in the regularization step. The input and output row show which variable is optimized and which variable is fixed during each step.

2.5.1 Log-Demons Algorithm

The log-demons algorithm finds diffeomorphic deformations to warp a moving image into a fixed image. The deformations are parameterized with Stationary Velocity Fields (SVF). A displacement vector field can be generated from a SVF through the exponential map. The exponential map $\exp(v)$ of a smooth SVF v is defined in [Arsigny 2006] as the flow at unit time, $\phi(x, 1) = \exp(v(x))$, of the stationary ODE, $\partial\phi(x, t)/\partial t = v(\phi(x, t))$. To efficiently compute $\exp(v)$, [Arsigny 2006] proposed to use the scaling and squaring method. The theoretical motivation lies in the generalization of Lie Group theory to the infinite dimensional case. Although there are still some open questions to be resolved, in practice this approach provides good results. One interesting point of this registration framework is the efficient optimization in the domain of SVFs. This property explains the denomination of log-domain (or simply log-demons) registration.

The general form of the demons algorithm was formulated in [Cachier 2003] and later in [Vercauteren 2009] an implementation with SVFs instead of displacement vector fields was presented. The goal is to find v^l that warps the moving image I_s into the fixed image I_t (or resamples I_s in I_t), by minimizing the cost functional,

$$C(I_t, I_s, v_c, v^l) = \sigma_i^{-2} \text{Sim}(I_t, I_s, v_c) + \sigma_x^{-2} \text{dist}(v_c, v^l)^2 + \sigma_T^{-2} \text{Reg}(v^l),$$

where

- Sim is the similarity between two images, we use the sum of squared distances on the image intensities, $\text{Sim} = \frac{1}{2} \|I_t - I_s \circ \exp(v_c)\|^2$,
- dist is the hidden term linking Sim and Reg, we use $\text{dist} = \|v_c - v^l\|$,
- Reg is the regularization term, we use $\text{Reg} = \|\nabla v^l\|^2$.

Each term has a weighting parameter σ_i , σ_x and σ_T . As shown in [Vercauteren 2009], $C(I_t, I_s, v_c, v^l)$ can be optimized alternatively over the variables v_c , the correspondence velocity field computed by the first optimization part of the log-demons algorithm, and v^l . First, minimizing,

$$C_{\text{sim}}(I_t, I_s, v_c, v^l) = \sigma_i^{-2} \text{Sim}(I_t, I_s, v_c) + \sigma_x^{-2} \text{dist}(v_c, v^l)^2,$$

with respect to v_c and fixed v^l . Second, a Gaussian smoothing of v_c , which minimizes,

$$C_{\text{reg}}(I_t, I_s, v_c, v^l) = \sigma_x^{-2} \text{dist}(v_c, v^l)^2 + \sigma_T^{-2} \text{Reg}(v^l),$$

when the regularization term is $\text{Reg}(v^l) = \|\nabla v^l\|^2$. Alternating between these two steps, as shown in Fig. 2.5, allows for a very efficient registration.

2.5.2 Integration of the Estimation into the Log-Demons

To optimize the polyaffine transformation tree, we remove the regularization term but we constrain the velocity field v^l to be issued from a polyaffine transformation, i.e. to have the form specified in Section 2.3, Equation (2.8). First, we minimize the functional with respect to v_c ,

$$\begin{aligned} C(I_t, I_s, v_c, v^l) = & \sigma_i^{-2} \int_{\Omega} (I_t - I_s \circ \exp(v_c))(x)^2 dx + & (2.14) \\ & \sigma_x^{-2} \int_{\Omega} \|v_c(x) - v^l(x)\|^2 dx, \end{aligned}$$

while the first term describes the sum of squared differences (SSD) image metric, the second term is called the hidden term that allows for the splitting of the optimization. What differs from the log-demons algorithm introduced in [Vercauteren 2009] is that we replace the regularization step by a projection to find the closest polyaffine transformation tree. This requires only a modification in the second step of the optimization, schematically shown in Fig. 2.5.

Now given v_c , we can solve for M_i^l using linear least squares. Here we use our newly introduced projection of SVFs onto LEPTs as described in Section 2.2.3,

$$\text{proj}_{M^l} v_c = \underset{M^l}{\text{argmin}} \int_{\Omega} \lambda(x) \|v_c(x) - \sum_{i=1}^n w_i^l(x) M_i^l \tilde{x}\|^2 dx.$$

As shown in Equation (2.6), we end up with the following linear system of equation to solve,

$$M^l = [M_1^l \dots M_n^l] = B\Gamma^+.$$

Here, the matrix Γ does not change for different velocity field observations as long as the mask image and weights are fixed, hence only B needs to be recomputed for each iterative step of the log-demons optimization. The sequential per-level estimation with the log-demons algorithm is shown in Algorithm 1.

Algorithm 1 Estimation of Polyaffine Transformation Tree

Sequentially estimate levels $l = 0, \dots, k$

- Initialize demons with previous level $v^l = v^{l-1}$ (for starting level $v^0 = 0$)
 - Precompute Γ
 - Iterate until convergence
 - Compute correspondence SVF v_c
 - Compute residual SVF $v_r = v_c - v^{l-1}$
 - Project v_r onto M_1^l, \dots, M_n^l by solving the linear least square problem $M^l = B\Gamma^+$
-

2.6 Femur Bone Registration with Manual Regions

In this section, we present validation results of our registration for manually defined regions. We first present the clinical application and then show how our registration performs w.r.t. manual landmark measurements conducted by two medical experts. The results show that the polyaffine method improves the accuracy of the standard log-demons registration.

2.6.1 Clinical Problem

Tumor excision is the primary treatment of aggressive or recurrent benign bone tumors and malignant bone sarcomas. This requires an invasive surgical intervention that entails a residual bone defect, which can be reconstructed with a fresh frozen bone allotransplantation. In orthopaedics, recent improvements in diagnostic and therapeutic techniques have produced an increase of the patient survival as well as a reduction of the complication rate [Muscolo 2005]. It has been shown that the selection of bone allograft in terms of shape and size is crucial to prevent changes in joint mobility and load distribution, which can lead to joint fractures and early joint degeneration [Enneking 2001]. However, current selection approaches are very time-consuming, mostly based on manual measurements performed directly on the bones or on three-dimensional models reconstructed from images.

We present a method to perform allograft selection through image registration. We focus on six landmarks extracted from the velocity field obtained through registrations. The six landmarks define three distances on the bone (Fig. 2.7): Transepicondyle distance (A), anterior-posterior distance in the medial condyle (B) and in the lateral condyle (C). The clinical aspects of this work were recently published in [Ritacco 2012]. Here we use the results to show the validity of our registration compared to measurements performed by two medical experts on the landmarks defining A, B and C.

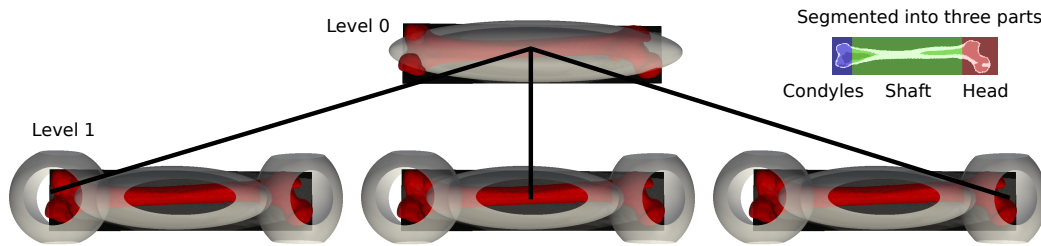


Figure 2.6: Ellipsoids representing Gaussian weights at σ for levels 0 and 1 (at the image boundary ellipsoids are cut). The Gaussian weights are defined through the labeled image shown on the top right, which splits the femur into three parts: Condyles, shaft and femoral head. The red femur is the surface extracted from the template image.

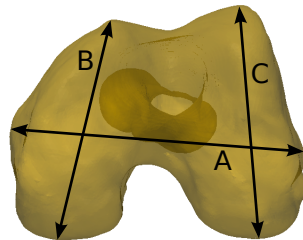


Figure 2.7: Six femur landmarks that were measured by medical experts, which define the three distances A, B and C.

2.6.2 Special Case of a Polyaffine Transformation Tree

To handle rotational misalignments of the femoral head and condyles we propose to split the bone into three regions. This results in a tree with two levels as shown in Fig. 2.6. Level 0, represents a global affine registration. Level 1, represents the division into three parts. The middle section of the femur is defined as shaft region. The distal and the proximal end are condyle and head region, respectively. We initialize the tree with an anisotropic scale transform computed from the enclosing bounding box of the entire femur.

2.6.3 Validation with Landmark Measurements by Medical Experts

We register 146 CT images of femur bones with voxel size 1 mm. The ground truth of the ABC measurements was obtained by manually selecting the landmarks on 3D reconstructed surface models. Two medical doctors performed these measurements independently and one expert repeated the measurements after a few days to yield the intraobserver variability. We compare four registration methods:

First, an anisotropic scaling computed from the enclosing bounding boxes, referenced hereafter with *Scale*. Second, a standard log-demons, referenced hereafter with *LogDemons*. Third, the newly developed 2-level polyaffine tree, referenced hereafter with *Tree*. Forth, a standard log-demons initialized with the transformation obtained from the *Tree*, referenced hereafter with *Tree relaxed*.

The results are shown in Fig. 2.8. For landmark distance A, the *Tree* is more accurate than the *LogDemons*. This is quite surprising, because the number of parameters needed to describe the *LogDemons* are three per voxel, with an image size of $120 \times 138 \times 542$, this results in a total of 10^7 parameters, whereas for the *Tree* transformation we have one region at level 0 (12 parameters) and three regions at level 1 (36 parameters), resulting in a total of 48 parameters. *Tree relaxed* shows two outliers not present in *Tree*, indicating the robustness of estimating only a few parameters as opposed to an entire field. For landmark distance B, *LogDemons* and *Tree* perform similarly as for distance A, and *Tree relaxed* shows one outlier not present in *Tree*. For landmark distance C, *Tree* shows a higher median than *LogDemons* and *Tree relaxed*. Here *Tree relaxed* performs favorably.

For all three landmarks, we can state that either the *Tree* or *Tree relaxed* are more accurate and/or more robust towards outliers. The results for *Tree* are particularly impressive, since the number of parameters needed to describe the geometrical deformation is five orders of magnitude smaller. The reduction in the number of parameters to estimate during the registration could explain why the results are in all cases more robust. We believe that these improvements stem from considering torsion and rotation in head and condyles which is implicitly modeled by dividing the bone into three parts and is not considered in a standard non-linear registration. We can thus incorporate our prior knowledge about the anatomy into the registration process by simply defining a rough mask of expected regions. This clearly indicates the power of the new method to capture the anatomical variability.

2.7 Mandible Bone Registration with Hierarchical Regions

In the previous section, we showed registration results for manual regions defined on femur bones. This is a special case within the family of polyaffine transformation trees, where the tree has two levels (level 0, one region; level 1, three manually defined regions). Now we show the more general case by computing a hierarchy of regions. We show its usefulness for mandible bones, where we encounter different variability at different levels. In this kind of anatomical setting, manual regions are not tractable anymore, due to the increasing number of regions with number of levels (grows quadratically in the case of binary trees).

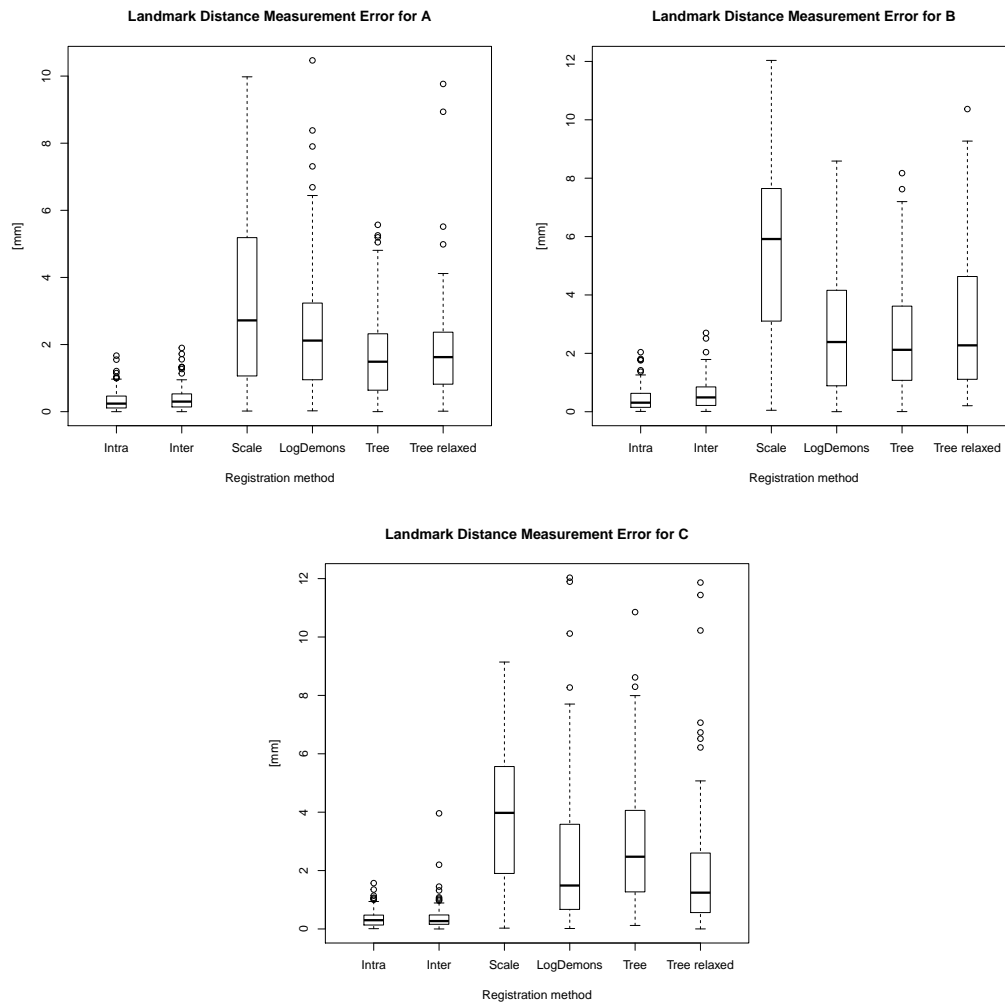


Figure 2.8: Boxplots of measurement errors (circles represent outliers) computed for each registration method and compared to *Intra* and *Inter* rater error conducted by medical experts. *Scale* represents a global scale transform; *LogDemons* a standard log-demons with scale initialization; *Tree* a 2-level tree with manual regions; *Tree relaxed* a standard log-demons with Tree initialization.

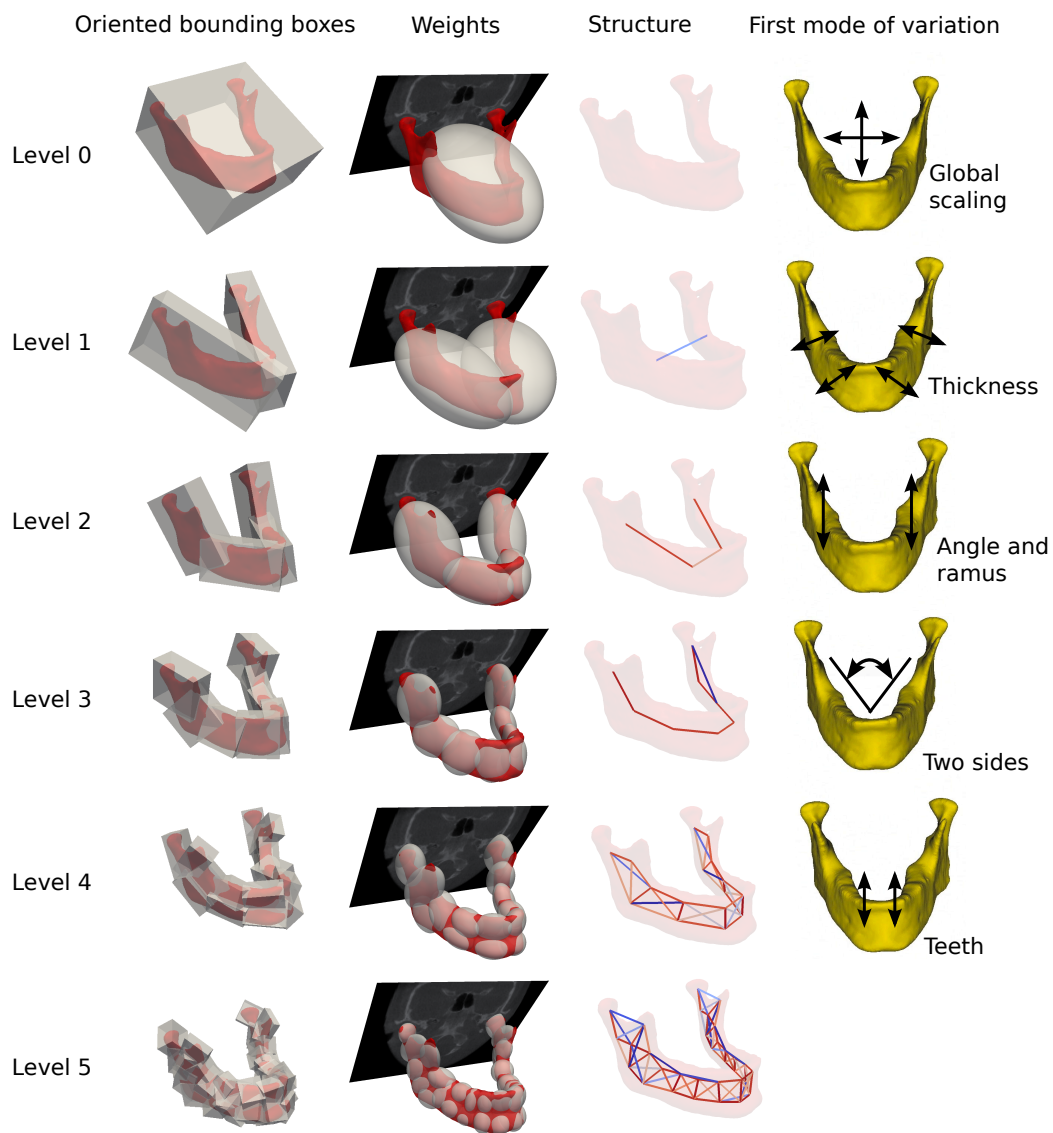


Figure 2.9: The red mandible is the surface extracted from the template image. **Column 1:** Oriented bounding boxes computed using the algorithm presented in Section 2.4. The Gaussian weights are driven by the gradient in the CT image. **Column 2:** Ellipsoids representing Gaussian weights at σ for levels 0 to 5. The parameters of the Gaussian weights are derived from the OBB. **Column 3:** Structure imposed by the weights. The color of the edges encode correlations between regions, ranging from low (blue=0.4) to high (red=1). **Column 4:** First PCA mode at each level, showing the main residual variation at that level.

2.7.1 Weights Derived from Oriented Bounding Boxes

The multiscale and hierarchical regions are computed using the weighted OBBTree algorithm on feature images (as described in Section 2.4.2). The resulting boxes are visualized in Fig. 2.9 (first column). Starting at level 1, we observe the division of the mandible into left and right side, followed by subdivisions into clinical regions as described in Fig. 2.1, to tooth-sized regions, and finally even finer scales (not visualized here), which are harder to interpret clinically. From the boxes, we computed the Gaussian weights with a scaling parameter of $\alpha = 1$. The Gaussian weights visualized as ellipsoids are shown in Fig. 2.9 (second column). In the third column, the correlation of weights are depicted according to,

$$\text{Corr}_{ij} = \Sigma_{ii}^{-1/2} \Sigma_{ij} \Sigma_{jj}^{-1/2}, \quad (2.15)$$

where Σ_{ij} is defined in Equation (2.11), and Corr_{ij} is decomposed using singular value decomposition to extract the major axis of correlation. The correlation of the major axis is colored coded from cool (blue=0.4) to warm (red=1). The graph structure clearly reveals the intrinsic underlying dimensionality of the object at each scale, going from a curve to a ribbon and finally in some areas locally to a 3D volume. It would be interesting to study if this could be a robust alternative to the medial axis or surface representation.

2.7.2 Estimation of the Transformation Tree

Rigid registration is considered as a pre-processing step to the work presented here. Indeed, intensity-based rigid registration procedures failed due to the angle between left and right side of the mandible, causing the registration to either fit the left or the right side. Instead, we extract surfaces from segmented images and align them according to the principal directions of their vertices. For the population-based analysis of mandible CT images, we register all 43 CT images to a template and analyze the deformations obtained. The template (35 year old male) was selected through visual examination. For the implant design study presented in Section 2.8, we need registrations up to level 4. In this section, we analyze all levels and compare them to two other types of registration.

In Fig. 2.10, the mean squared error (MSE) of intensity difference (fiducial localization error), computed over the union of template mask and subject mask, for three different types of registrations are shown.

- Type 1 ($S0$ and $S0R$): Standard log-demons $S0R$ with a global affine initialization computed using a tree with one level containing the root node $S0$.
- Type 2 ($M0$, $M1$ and $M1R$): A manually defined tree of regions as depicted in Fig. 2.11. At level 0, one region to capture the global affine variability $M0$, and at level 1, 9 regions defined according to the AO foundation classification scheme $M1$. The transformation parameters are estimated using Section 2.5. Standard log-demons $M1R$ initialized with $M1$.

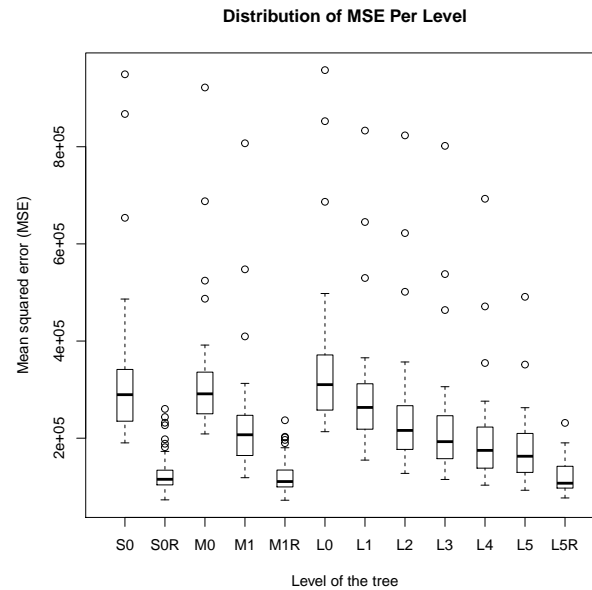


Figure 2.10: Performance of the multiscale polyaffine registration. Mean squared error (MSE) of intensity difference (fiducial localization error) calculated on the union of template and subject mask image for each of the 43 registrations (without the template to itself registration). Explanation of boxplots (circles represent outliers) starting from the left hand side: *S0*: Level 0 of manual tree defined through mask image. *S0R*: Standard log-demons initialized with *S0*. *M0*: Level 0 of manual tree defined through mask image. The results differ from *S0* because the normalization of weights is computed over all levels. *M1*: Level 1 of manual tree defined through label image. *M1R*: Standard log-demons initialized with *M1*. *L0* to *L5*: Level 0 to level 5 of the data-driven multiscale and hierarchy of regions. *L5R*: Standard log-demons initialized with *L5*.

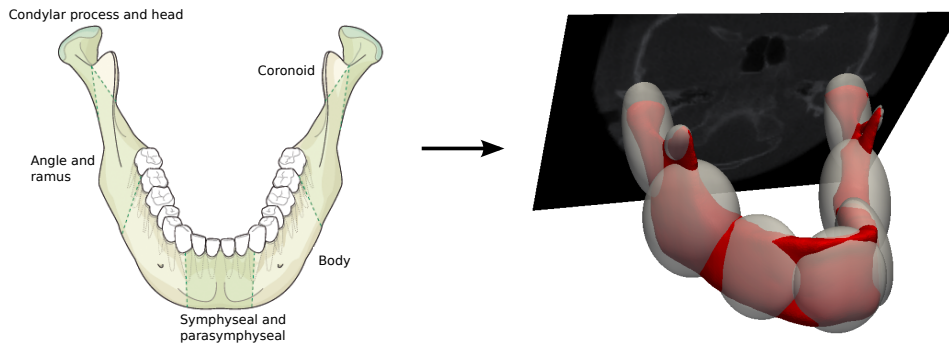
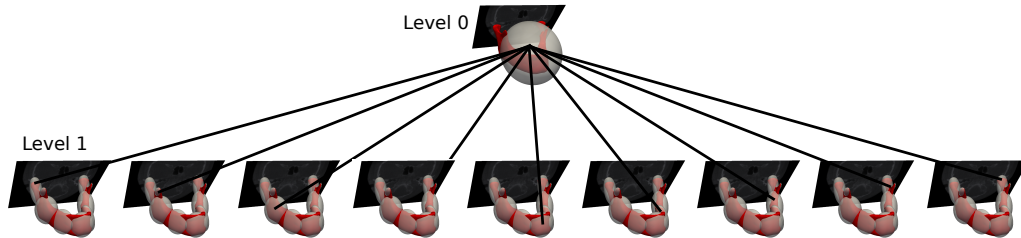
Region definition according to the AO foundation**Polyaffine tree with manual regions**

Figure 2.11: Manual regions defined on the reference image according to the AO foundation classification scheme.

- Type 3 ($L1-L5$ and $L5R$): Data-driven multiscale and hierarchical weight tree derived with the algorithm presented in Section 2.4 $L1-L5$. The estimation of transformation parameters uses Section 2.5. Standard log-demons $L5R$ initialized with $L5$.

Figure 2.10 shows two main results:

- Decrease of MSE with increasing amount of regions (levels). The MSE converges, which provides evidence of the consistency of our method (although the finer levels are not statistically analyzed in this work).
- All three relaxed registrations $S0R$, $M1R$ and $L5R$ are in the same range, with $L5R$ having less outliers. This suggest a more robust registration due to the stepwise initialization across levels.

Unfortunately, we cannot evaluate the accuracy here as we do not have manual measurements provided by medical experts for mandibles. In the future, we plan to validate the accuracy in a similar fashion as described in the previous section for femurs.

2.7.3 Analysis of Obtained Tree Transformations

One important aspect of our tree structure lies in its power of decomposing features into different scales, this can be shown by performing a hierarchical PCA for mandibles. The per level PCA (Fig. 2.9, column 4) can be interpreted as follows: (Level 0) global scaling; (Level 1) thickness; (Level 2) reorientation in the region of the masseter; (Level 3) relative displacement of condyles and coronoid processes; (Level 4) change in teeth region. This gives a visual validation of the usefulness of per level hierarchical statistical analysis, clearly distributing features across different scales.

We encountered instability starting at level 5, where the PCA modes become anatomically unrealistic. We are currently working on a Bayesian framework to make the registration more robust for higher levels.

2.8 Implant Design Based on Statistical Analysis of Transformations

In this section, we show how our registration method can be used for implant design. In order to analyze the groupwise deformations modeling the different anatomies in our population, we first draw the connection between the methodology and the clinical problem of population-based implant design in Section 2.8.1 (depicted in the first and second row of Fig. 2.12). Then, we perform (Section 2.8.2) a k-means clustering of transformations for selected regions (results depicted in the last row of Fig. 2.12). Each mean of each cluster represents a specific mandible geometry (surface and voxel intensities), which can be used to drive the design of an implant.

Our dataset consists of 43 mandible CT images of healthy patients aged between 23 to 88, with a median age of 65.5 and four patients with unknown age; 16 patients were female and 26 male. The images are resampled during rigid registration from an original spacing of 0.4 mm (uniform) to a more computational tractable spacing of 1.25 mm.

2.8.1 Link Between Clinical and Data-Driven Regions

Given the regions that were found on the template image in Fig. 2.9, we identify the corresponding clinically motivated regions from Fig. 2.1. This allows us to identify a subset of clinically important parameters. We can perform a statistical analysis for each implant design study on 12 (one region) or 24 (two regions) parameters. At this point we do not enforce a perfect overlap between the data-driven regions and the clinical regions. Work in progress focuses on an approach to incorporate prior knowledge into the tree to enforce a perfect overlap for certain regions, while allowing for data-driven regions in areas where there is no anatomical information available (i.e. very fine structures at fine levels). The link between automatic OBBTree and anatomical regions is shown in Fig. 2.12. For “symphyseal and parasymphyseal”,

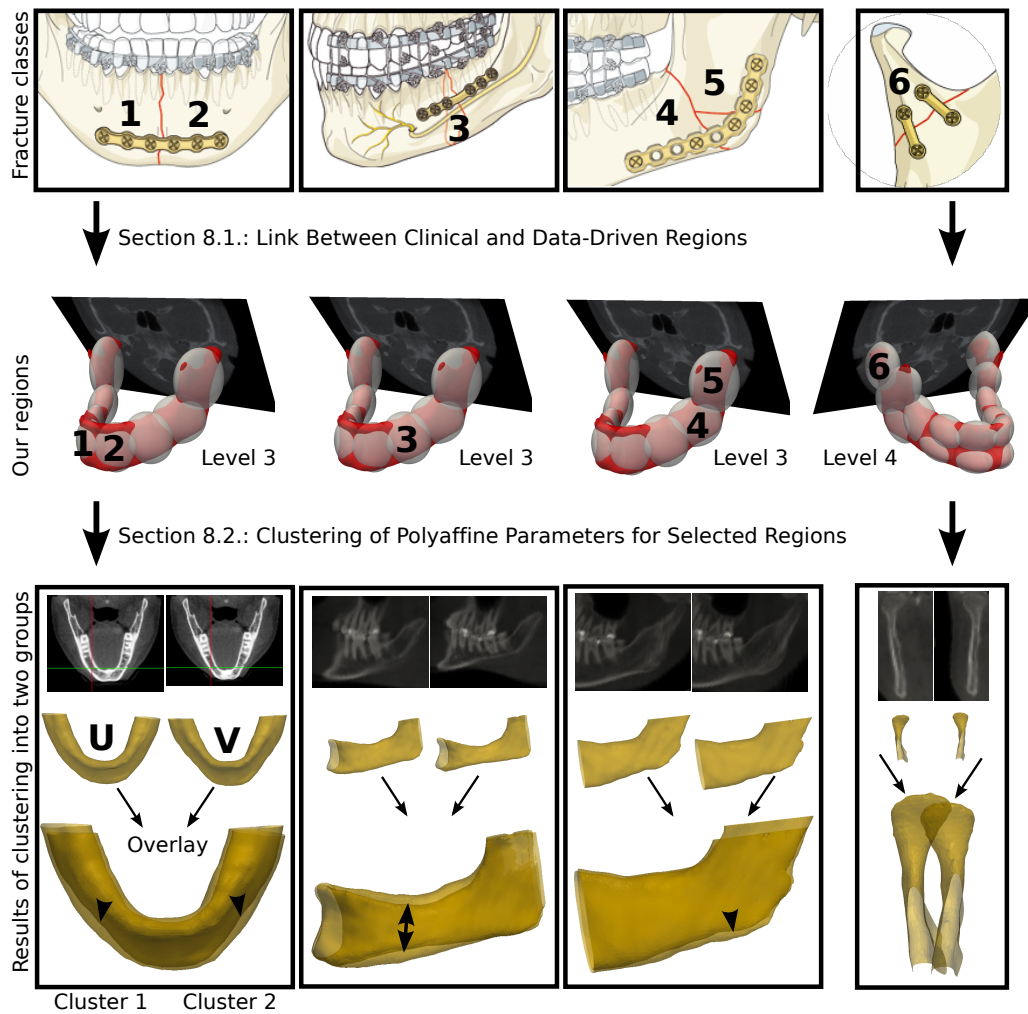


Figure 2.12: Overview of the entire work flow. Starting with the fracture classes given by the AO foundation, we identify 6 regions that are close to fracture sites. We then identify corresponding regions that were retrieved during our new registration method. The three columns on the left are regions identified on level 3, the one on the right is one region at level 4. K-means clustering for each column is performed. The last row, shows the computed clusters: One slice extracted form the two mean images of each cluster, surface of the mean image of each cluster and overlay of the two mean surfaces for comparison.

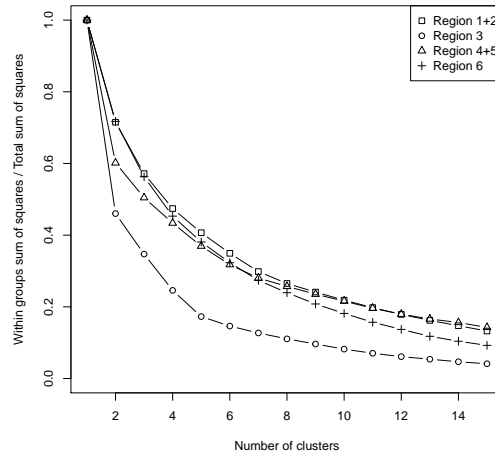


Figure 2.13: K-means clustering results for all four regions. Region 3 shows a decrease by approximately half of the WSS at two clusters.

“body”, and “angle and ramus” we select regions at level 3; for “condylar process and head” one region at level 4 is identified.

2.8.2 Clustering of Polyaffine Parameters for Selected Regions

The link between clinical and data-driven regions, presented in the previous section, allows us to focus on each part of the bone independently. For each part the goal is to find clusters representing distinguishable surface and intensity features. We apply k-means for the clustering of each part. The selection of the number of clusters, is a crucial decision in k-means, and in our application it is up to the implant designer to select how many different implants to build as each additional implant causes additional costs. In Fig. 2.13, the reduction of Within groups Sum of Squares (WSS) as a function of the number of clusters indicates a gradual decrease. In our experiments we use two clusters. In Fig. 2.12 on the last row, the different surface shape and intensity features are shown. To illustrate the difficulty of finding these feature differences by visual inspection, Fig. 2.14 shows one slice of each mandible in the transversal plane. Each slice represents the transformed template slice at level 3. As one can see it is hard to distinguish the shape and intensity feature by pure inspection of individual images.

2.9 Discussion and Conclusion

In this work, we proposed a new approach to population-based implant design for mandibles. We presented a new method that is able to link the registration directly to the clinical relevant anatomical regions. Experiments on 146 CT images of femur

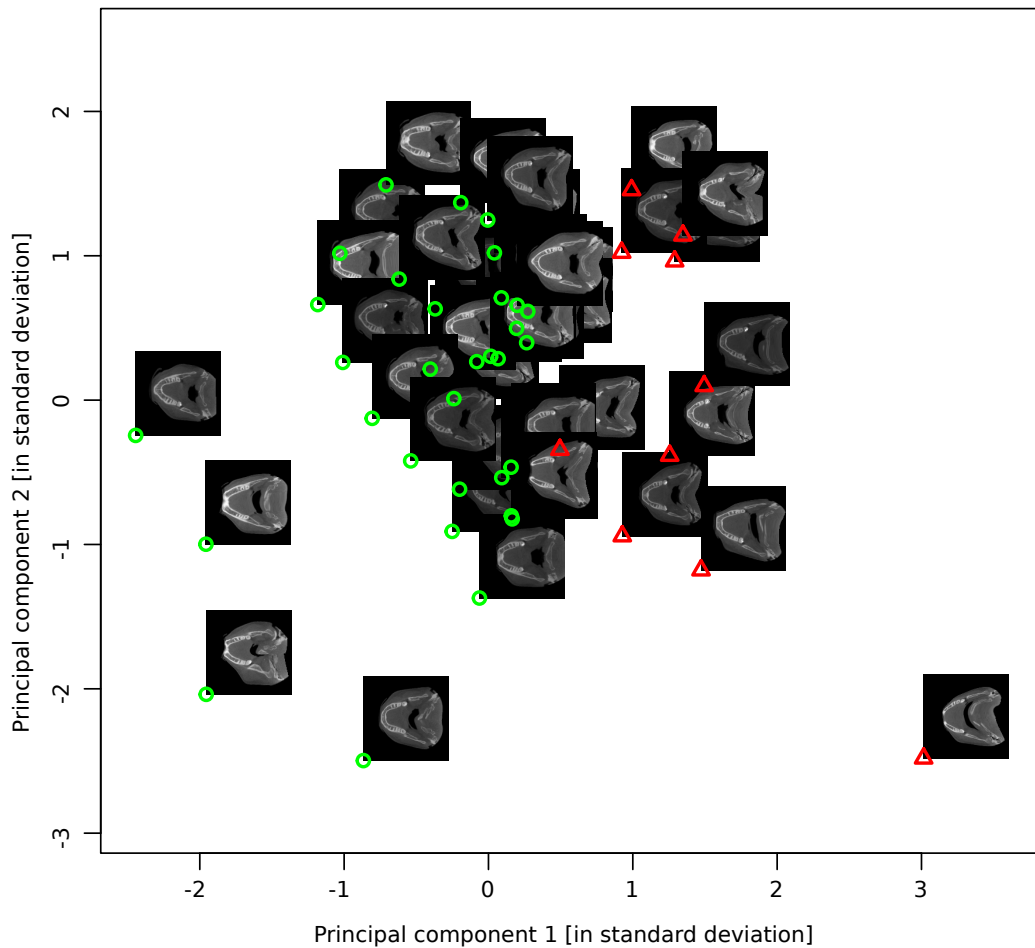


Figure 2.14: K-means clustering results for “symphyseal and parasymphyseal” (region 1+2). Red triangles represents the V-shaped mandibles; green circles represent the U-shaped mandibles. The slices are generated by warping the template slice with transformations at level 3. The 24-dimensional data points (two affine transformations) are projected onto the two largest principle components for visualization. The clustering is done in the 24-dimensional space.

bones showed that our approach (with manual regions) is more accurate than the standard log-demons. The ground truth was provided by two medical experts, who manually identified three landmark distances. Furthermore, we illustrated the usefulness of the link between registration and clinical regions (data-driven hierarchical regions) through a clustering of 43 mandibles CT images, considering not only the surface but also the volumetric information.

In contrast to current population-based implant design methods we could show a direct connection between clinically relevant regions and our methodological framework. Our findings are in accordance with the clinical literature. The authors in [Watanabe 2010] presented a morphological study on manual measurements performed on 79 Japanese patients on “symphyseal and parasymphyseal”, “body” and “angle” regions. A large variability in terms of standard deviation ranging from 3.5 mm to 3.8 mm in height and 1.3 mm to 3.2 mm in width was reported, supporting the evidence of high variability in these regions that were reflected in our results. In addition to these surface morphological findings, the volumetric shape informations could now be used for biomechanical simulations on optimal screw placement by taking advantage of the correlation between image intensities and material properties, along the line of [McBroom 1985]. This implies an additional statistical analysis of the intensities in the template space. Preliminary results in this direction were shown in [Bonaretti 2011].

Our method depends on three major parameters: First, the selection of the template image I_t , which serves as the basis of the weight definition, and thus influences not only the way transformations are estimated but also which regions are selected for clinical analysis. Hence, by changing the template we expect to obtain slightly different results. Due to the fact that weights can be easily visualized, an assessment of the quality of the selected template can be done by clinicians quite reliably. To further improve the robustness of this procedure, we plan to introducing a group-wise weight definition framework, in which we search for the optimal configuration of weights considering all images available. Second, the scaling parameter α of the covariance matrix, which controls the smoothness of the final deformation. In the current work, this parameter was set heuristically. An alternative approach would be to find the optimal scaling parameter by evolving the regions (and thus weights) during the transformation estimation phase. Third, the total number of levels k to consider for registration. In the presented clinical application this parameter is set to level 3 and 4 given the clinical regions that are of interest. For other applications, it might be useful to define a stop criterion based on the residual variability. One step further, would be to enforce a stop criterion per node instead of the entire level. This would further reduce the number of parameters used to describe a deformation and improve the direct analysis of the registration results by clinicians.

Our methods can be decomposed into three major building blocks: First, the structure of the polyaffine trees. At the moment this is a binary tree with a fixed number of levels and fixed number of nodes. The tree structure with its number of levels and number of nodes could be relaxed and adapted by learning an optimal structure from a population of images. This optimization could be accomplished in a

groupwise fashion by imposing an additional penalty favoring certain structure over others. Second, the definition of regions. By reformulating the OBBTree subdivision process in a more probabilistic framework, e.g. Gaussian Mixture Models, we could introduce priors, e.g. independence between regions on the polyaffine transformation trees, leading to an even lower dimensional representation. We can see at this point that the first two building blocks are very strongly linked. Third, the estimation of transformations. In the current implementation, we use the sum of squared differences as our similarity measures in the log-demons algorithm. This could be extended to consider other similarity measures. Furthermore, other methods than the log-demons algorithm could be used to drive the estimation. All methods that are parametrized with SVFs are potential candidates. Additionally, by changing the coarse to fine transformation estimation to a joint estimation over all levels, we believe we can further improve the results in terms of robustness toward outliers (by taking care of artifacts at finer levels) and improving interpretability (by skipping levels). At the core of our new method lays the introduction of a new basis for SVFs. As we showed in our experiments, this basis has very close links to anatomical substructures. In the future, this method has the potential to discover the hidden and possibly sparse structure of the anatomy. We currently work on a method that imposes sparseness on the basis on a groupwise level by formulating our method in a Bayesian framework.

A Generative Statistical Model for Multiscale Diffeomorphic Deformations

This chapter has been submitted as a journal article in [Seiler 2012b]. The journal article builds upon the published conference paper [Seiler 2012d]. Part of the introduction overlaps with the general introduction of this thesis and the introduction of Chapter 2. In contrast to the ontology of the lumbar vertebrae presented in the general introduction, here we work on the ontology of mandibles.

Abstract

Locally affine (polyaffine) image registration methods capture intersubject non-linear deformations with a low number of parameters, while providing an intuitive interpretation for clinicians. Considering the mandible bone, anatomical shape differences can be found at different scales, e.g. on a coarse scale between the entire left or right side, and on a fine scale between teeth. Classically, sequential coarse to fine registration are used to handle multiscale deformations, instead we propose a simultaneous optimization of all scales. To avoid local minima we incorporate a prior on the polyaffine parameter. This kind of group level prior is natural in a polyaffine context, if we assume one configuration of regions that describes an entire group of images, with varying transformations for each region. In this paper, we reformulate polyaffine deformations as a generative statistical model, which enables us to incorporate deformation statistics as a prior in a Bayesian setting. We find optimal deformations by optimizing the maximum a posteriori probability. We assume that the polyaffine parameter follow a normal distribution with given mean and concentration matrix. Parameters of the prior are derived from an initial coarse to fine registration. Knowing the region structure, we develop two blockwise inverse of the covariance matrix to obtain the concentration matrix. We conduct experiments on 42 mandible CT images. The results show that polyaffine parameter estimated with a prior are more accurate in terms of Dice coefficient and contour mean distance on manually segmented images, and are more robust in terms of the determinants, rotational and translational part for all regions. To our knowledge, we are the first to introduce simultaneous multiscale optimization through a prior at the group level in polyaffine registration.

Contents

3.1	Introduction	47
3.1.1	Ontology of the Human Anatomy	47
3.1.2	Population-Based Implant Design	49
3.1.3	Trees on Geometrical Deformations	50
3.2	A GLM Formulation of Intersubject Deformations	51
3.2.1	Linear Model for Deformations	53
3.2.2	Observing Noisy Stationary Velocity Fields	53
3.3	A Generative Statistical Model for Deformations	54
3.3.1	Posterior Inference of Polyaffine Parameter	54
3.3.2	Sample Covariance Matrix Inverse	55
3.4	Experiments on Real CT Data	57
3.4.1	Comparison of Sample Covariance Inverse Methods	59
3.5	Discussion and Conclusion	65

3.1 Introduction

A multiscale description of anatomical intersubject variability is important in many clinical applications. In this section, we first introduce a more general view of the anatomy, which promotes tree-like descriptions. Second, we move to the specific field of implant design for mandible bones to illustrate how the methods developed in this paper can be used in the clinics.

3.1.1 Ontology of the Human Anatomy

The term *anatomy* originates from the two Greek words *ana* and *temnein*, which translate in English to *apart* and *to cut*, respectively. The origin of this word leads us directly to the essence of this paper, which is to deepen our understanding of parts of our human body and how they interact. The Foundational Model Anatomy (FMA) ontology, as presented in [Rosse 2008], is a formal description of classical human anatomy textbooks. In classical textbooks the anatomy is divided according to function or regions. The FMA provides a more formal definition of the division process. At the core of the FMA is a tree data structure that represent the hierarchical and multiscale anatomical shape at different levels of granularity.

3.1.1.1 Anatomical Structure, Granularity and Relations

The FMA definition of anatomical structures is given by the following three points:

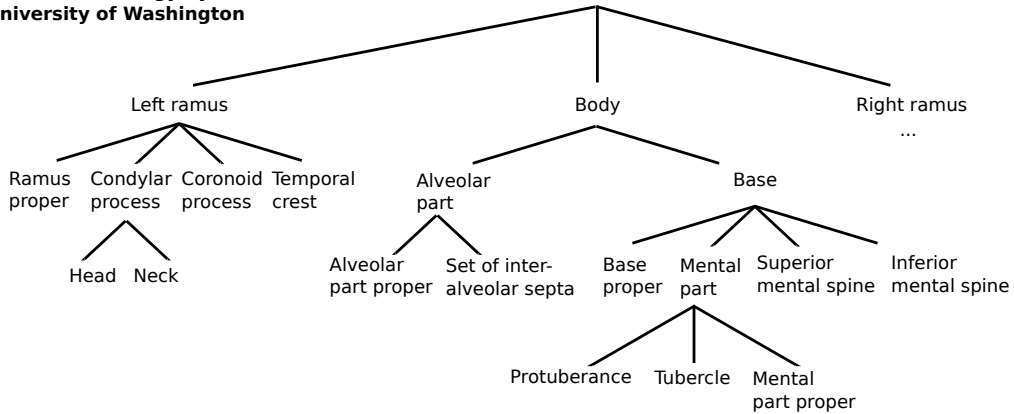
1. Anatomical structures are three-dimensional shapes
2. Anatomical structures are products of our genes
3. The parts of an anatomical structure are arrangements through our genes

Therefore, a mathematical description of anatomical structures needs to be able to describe three-dimensional shapes that are divided into parts and interact with other parts of the same or other anatomical structures. One of the central point is the tree-based description of the anatomy where entities at finer levels of granularity inherent properties form coarser levels. This kind of reasoning is implicitly considered in many medical image analysis algorithms through a (multiscale) coarse to fine analysis. In this work, we make it explicit by modeling the granularity with trees of geometrical deformations.

In the context of anatomy, the term granularity refers to the level of detail at which we observe or describe the anatomical structure. It defines the extent to which the anatomy is broken down into small parts. In Figure 3.1, the mandible bone is shown at different levels of granularity. On the top, we see a small extract of the FMA ontology form the University of Washington [Rosse 2008]. On the bottom, an illustration of the data-driven approach that we present in this manuscript is given.

According to FMA, anatomical relations are associations between anatomical entities. Relations are visualized with edges between nodes in the ontology tree

**Mandible Ontology by FME,
University of Washington**



Data Driven Multiscale and Hierarchical Tree of Regions

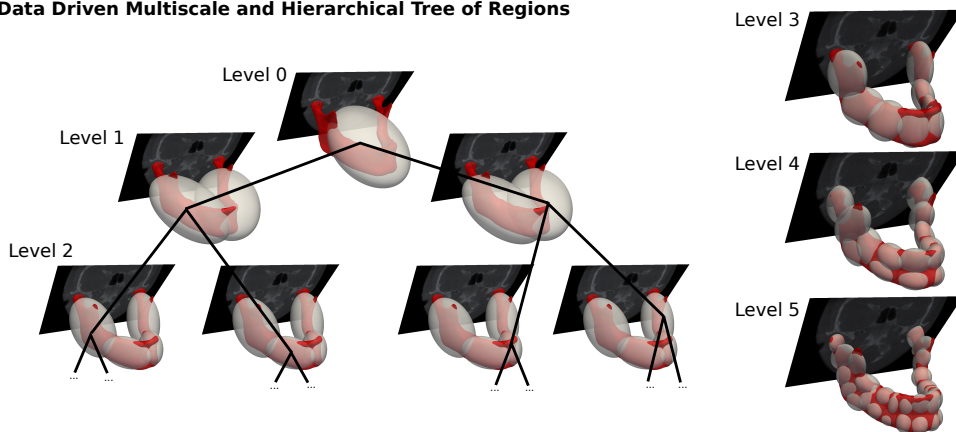


Figure 3.1: **Top:** Ontology of mandible anatomy. Subdivision of mandible into anatomical regions proposed by [Foundational Model Explorer](#), University of Washington [Rosse 2008]. **Bottom:** Tree of Gaussian weights. Weights divide the anatomy into continuous parts. The tree can be directly interpreted by clinicians. Each Gaussian weight represents one region and is visualized as one ellipsoid thresholded at σ . The red contours are extracted from CT data and one slice of the original CT image is shown (to indicate that we work in the image domain and not only on the contour).

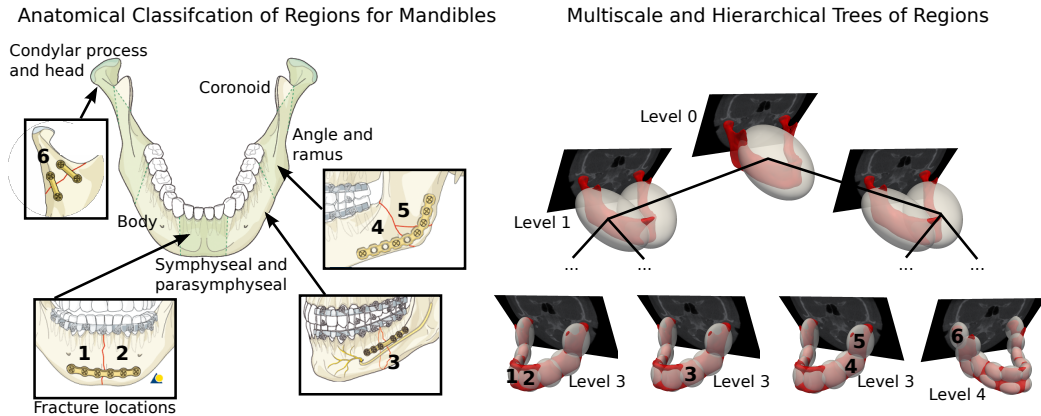


Figure 3.2: **Left:** Subdivision of mandible into anatomical regions proposed by the AO foundation to classify fractures for reconstructive surgery. Implants at four different anatomical sites are shown. Image source: www.aofoundation.org. **Right:** Tree of Gaussian weights. Each Gaussian weight represents one region and is visualized as one ellipsoids at σ . The contours extracted from CT data in red and one slice of the original CT image (to indicate that we work in the image domain and not only on the contour) are shown.

(Fig. 3.1). This means that anatomical structures can not only be described by their spatial location but also indirectly through their related structures. In the realm of medical image analysis, researchers have been exploring these connections through statistical analysis of cohorts of functional and structural images. Particularly interesting are relations that are not obvious, e.g. relations between non-neighboring structures [Allasonnière 2011]. By investigating these relations we might find new anatomical knowledge that improves diagnostics for patients.

In this paper, we propose to move the FMA from a description of the average anatomical structure, granularity and relations towards a description of the variability of these terms in a population of subjects.

3.1.2 Population-Based Implant Design

Mandibular fractures most commonly result from facial trauma, with close to half of the patients requiring surgical repair [Ellis 1985]. A majority of 75% of fractures occur in males aged between 20 and 30 [Ellis 1985], and are often caused by physical assault. For these cases surgical repair proves most effective, with the goal of recovering the anatomical structure prior to the injury and thus restoring normal function. To reach this goal the surgeon places wires or implants at the fracture site, so that the natural fusion of separated bone pieces restores the prior structure as closely as possible. A correct repair aligns teeth for food intake, and restores the patient's aesthetics. In [Urken 1991], the authors propose a classification scheme for

mandibles based on regions according to anatomical, functional and aesthetic considerations. The online register www.aofoundation.org uses the same classification (Fig. 3.2) to guide surgeons through the major steps of mandible reconstructive surgery ranging from diagnosis, selection of the optimal surgical approach, to aftercare treatment. In addition to this classification scheme, the mandible can be subdivided even further into smaller regions, e.g. one region for each tooth. In the image space, this subdivision can theoretically be performed up to the voxel level, where coarser levels enclose finer ones, representing a hierarchy of regions that can be organized in a tree-like fashion. As the regions become more fine, it is harder to find a consensus among clinicians on the size, shape and location of the region.

Recent work on biomechanical analysis of implants, indicates that geometry and topology of implants are crucial to fracture stability. In [Lovald 2010], it was shown that implants optimized for “body” and “symphyseal and parasymphyseal” region, have smaller fracture strain, while minimizing patient intrusion with respect to larger implants. The economical cost of patient specific implants makes this approach impracticable at the moment, hence current focus is set on an intermediate goal: population-based implant design. Common key steps to population-based design, e.g. [Bou-Sleiman 2011, Bou-Sleiman 2012], are registration to capture shape variability as encountered in a population and statistical analysis of the registration results, performed subsequently and independently.

Current methods look at surface shape only, but registration approaches for implant design should consider not only bone surface information, but also volumetric information describing the bone density distribution, which is needed to compute best location and orientation of the placement of screws to fixate implants.

In this paper, we propose a region-based registration that can capture the multiscale shape variability for population-based implant design.

3.1.3 Trees on Geometrical Deformations

Due to region-based description of the mandible shape and the need for volumetric information we focus on locally affine transformations, also called polyaffine transformations. Polyaffine transformations fuse locally rigid and affine transformations into a diffeomorphism [Arsigny 2009]. An efficient registration algorithm using approximations of polyaffine transformations was presented in [Commowick 2008]. Other recent work includes [Zhuang 2010], where a locally affine registration method is developed for cardiac MR images.

To consider more complex shapes and foster reusability, [Buerger 2011] presented a multiscale approach with affine regions defined through a data-driven approach. The method splits rectangular shaped regions, which are aligned along the image directions, only if certain conditions are met. The authors in [Taquet 2011] iteratively optimize between affine parameters and anchor positions (center of regions) through an expectation maximization approach. In [Zhang 2011], Log-Euclidean Polyaffine Transformations (LEPT) are employed to register multi-modal cardiac sequences in an elaborate scheme. The algorithm iteratively adds new uniform Gaussian weighted

regions with different spatial position (mean parameter) and influence (variance parameter) until a mutual information-based criterion is satisfied. Even though these methods are very promising, the link between the clinical regions (Fig. 3.2) and the regions found by these algorithms, is either constrained by aligned rectangular shaped regions or spherical weights [Buerger 2011, Zhang 2011], or produce an intractable number (around 500) of regions [Taquet 2011].

In [Seiler 2012c], we introduced a hierarchical multiscale tree structure (called polyaffine transformation trees) that is motivated by the nature of the mandible anatomy, where regions are ordered and interact with each other in a way tractable for human understanding.

Aforementioned polyaffine methods are pairwise registrations, and to our best knowledge, no groupwise deformations statistics has yet been incorporated in this context. In [Pennec 2005], the authors incorporated a prior on non-linear deformations with a statistical interpretation of the regularization. We believe that transformations on a groupwise level are crucial in a polyaffine setting. This is motivated by the assumption that there should be one configuration of regions that describes an entire group of images, with varying transformations for each region. Furthermore, the multiscale property of mandibles and other anatomical structures should be incorporated.

In [Ashburner 1997], the authors presented a Bayesian approach for affine registration, in this paper, we propose a Bayesian formulation of polyaffine registration across scales. To accomplish this we contribute the following points:

1. A General Linear Model (GLM) formulation of intersubject polyaffine deformations
2. A generative statistical model for polyaffine deformations
3. Incorporation of deformation statistics as a prior at the group level in a Bayesian setting
4. Simultaneous estimation of multiscale deformations
5. Maximum a posteriori probability (MAP) of polyaffine deformation parameter

The structure of this paper is as follows. In Section 3.2, we formulate polyaffine transformation trees as a GLM. In Section 3.3, we use the GLM to introduce a generative statistical model enabling us to incorporate deformation statistics as a prior in a Bayesian setting. We find optimal transformations by optimizing the MAP with groupwise deformation statistics as a prior. In Section 3.4, we compare two different ways of creating the deformation prior and show results on 42 mandible CT images.

3.2 A GLM Formulation of Intersubject Deformations

In this section we reformulate polyaffine transformation trees recently introduced in [Seiler 2012c] as a General Linear Model (GLM). We start by introducing Log-

Euclidean Polyaffine Transformations (LEPTs), Stationary Velocity Fields (SVFs), the log-demons algorithm and their connections.

In [Arsigny 2005], the authors introduced polyrigid and polyaffine transformations in the context of medical image analysis. Their works showed how to obtain diffeomorphic deformations by fusing transformations using ordinary differential equations (ODE). The estimation of the transformation parameters by numerically solving the ODEs was computationally expensive and therefore hard to use in practice. To tackle the computational burden the same authors introduced the fast Log-Euclidean polyaffine framework [Arsigny 2009] and LEPTs. The authors redefined the problem by relying on the logarithms of the transformations. These logarithms are defined in the theory of Lie groups. In practice, this results in computations of these logarithms via matrix logarithms. The practical relevance of this theoretical reformulation of the problem was exploited in [Commowick 2008].

In [Arsigny 2006], the authors define the exponential $\exp(v)$ of a (smooth) vector field $v(x)$ as the flow at time 1 of the stationary ODE $\dot{x} = v(x)$. This generalizes the equivalence between one-parameter subgroups and exponential to SVFs v and diffeomorphisms ψ . This equivalence exists in the finite-dimensional case as described in the previous section. However, a proof for the existence and uniqueness of the logarithm $\log(\psi) = v$ is still an open research question. In this work we do not rely on it, since we only generate diffeomorphisms parameterized with SVFs using $\exp(v) = \psi$.

The general form of the log-demons algorithm for stationary velocity fields (SVF) was formulated in [Vercauteren 2009]. The goal is to find v_M that warps the fixed image I_t into the moving image I_s (or resamples I_s in I_t), by minimizing the cost functional,

$$C(I_t, I_s, v, v_M) = \sigma_i^{-2} \text{Sim}(I_t, I_s, v_M) + \sigma_x^{-2} \text{dist}(v, v_M)^2 + \sigma_T^{-2} \text{Reg}(v),$$

where Sim, dist and Reg, are the similarity, the hidden and the regularization term, respectively. Each term has a weighting parameter σ_i , σ_x and σ_T . As shown in [Vercauteren 2009], $C(I_t, I_s, v, v_M)$ can be optimized alternatively over the variables v and v_M . Given v , the correspondence velocity field computed by the first optimization part of the log-demons algorithm, in [Seiler 2012c], we solve for M using linear least squares, i.e. minimizing

$$C(M) = \int_{\Omega} \lambda(x) \|v(x) - \sum_{i=1}^N w_i(x) M_i \tilde{x}\|^2 dx \quad \text{with} \quad \tilde{x} = \begin{bmatrix} x \\ 1 \end{bmatrix}, \quad (3.1)$$

where λ is a binary mask indicating background voxels (if no mask is available $\forall x \in \Omega : \lambda(x) = 1$). Throughout this paper we assume that all N region weights $w_i(x)$ are given, here x are spatial position within the image and i the index of one region. The extension of the OBBTree algorithm [Gottschalk 1996] to images as introduced in [Seiler 2012c] presents one way to create the weights. We refer the reader to [Seiler 2012c] for more details. For the remainder of this paper, we assume that the weights can have any non-parametric form and are smooth to ensure global diffeomorphisms.

3.2.1 Linear Model for Deformations

In this section, we formulate a linear model for SVFs that can be obtained from the polyaffine log-demons,

$$v_M(x) = \sum_{i=1}^N w_i(x) M_i \tilde{x}, \quad (3.2)$$

where $w_i(x)$ are normalized weights for region i , i.e. $\forall x \in \Omega : \sum_{i=1}^N w_i(x) = 1$. As introduced in the previous section, this kind of deformations are called LEPTs. The matrix,

$$\tilde{M}_i = \log \begin{pmatrix} A_i & t_i \\ 0 & 1 \end{pmatrix} = \begin{bmatrix} M_i \\ 0 \end{bmatrix},$$

is the matrix logarithm of the affine transformation of region i in homogeneous coordinates. The matrix exponential can efficiently be computed using scaling and squaring,

$$\exp(\tilde{M}_i) = \begin{bmatrix} A_i & t_i \\ 0 & 1 \end{bmatrix}.$$

For N regions let $M = [M_1, \dots, M_N]^T$ be a $3 \times 4N$ matrix. The vectorized version of this matrix is denoted by,

$$m = \text{Vect}(M),$$

with dimensions $12N \times 1$. We refer to m as the vector of polyaffine parameters. The weights can be represented as a $N \times 1$ vector,

$$\mathbf{w}(x) = [w_1(x), \dots, w_N(x)]^T$$

Now let's rewrite,

$$v_M(x) = M(\mathbf{w}(x) \otimes \tilde{x}) = [\mathbf{w}(x) \otimes \tilde{x}^T \otimes I_3] m,$$

where \otimes is the Kronecker product of matrices. Using this notation we can write the following linear model,

$$v_M(x) = \phi(x)m, \quad (3.3)$$

where $\phi(x)$ is a $3 \times 12N$ matrix, m is a $12N \times 1$ vector, $v_M(x)$ is a 3×1 velocity vector at spatial position x , and,

$$\phi(x) = \mathbf{w}(x) \otimes \tilde{x}^T \otimes I_3. \quad (3.4)$$

3.2.2 Observing Noisy Stationary Velocity Fields

Now in the polyaffine log-demons, we want to best explain the SVF v using the LEPT v_M according to Equation (3.1) from the previous section. In a probabilistic setting, the correspondence SVF is only observed at the voxel values $x_1, \dots, x_{|\Omega|}$ belonging to some mask region Ω , which means that the vector of observations is,

$$\mathbf{v} = [v(x_1)^T, \dots, v(x_{|\Omega|})^T]^T, \quad (3.5)$$

with dimensions $3|\Omega| \times 1$. As for the observations, let us stack the matrices $\phi(x)$ at all voxels into,

$$\Phi = \left[\phi(x_1)^\top, \dots, \phi(x_{|\Omega|})^\top \right]^\top, \quad (3.6)$$

with dimensions $3|\Omega| \times 12N$. The value of the predicted SVF at all voxel positions is now simply the linear model $\mathbf{v} = \Phi m$. Assuming an i.i.d. Gaussian noise of variance σ_v^2 in each spatial direction at all voxels, we end up with the GLM:

$$\mathbf{v} = \Phi m + \varepsilon \quad \text{with} \quad \varepsilon \sim \mathcal{N}\left(0, \frac{1}{\sigma_v^2} I_{3|\Omega|}\right), \quad (3.7)$$

where \mathcal{N} represents the multivariate normal distribution with mean and concentration matrix (inverse of covariance matrix). Rigorously, the log-demons computes velocity vectors from the gradient of the fixed and/or moving images, therefore, the velocities are not independent at adjacent voxel locations. Here we assume that this is a legitimate approximation.

3.3 A Generative Statistical Model for Deformations

In this section, we present the MAP to find optimal transformations with a prior for K patients. We denote m^k as the polyaffine parameter found for patient k . We denote $[k]$ to consider all patients.

3.3.1 Posterior Inference of Polyaffine Parameter

By assuming that the error term ε is i.i.d. normal distributed, the probability distribution of the SVFs for a given patient k is,

$$\mathbf{v}^k | \Phi m^k, \sigma_v^2 I_{3|\Omega|} \sim \mathcal{N}\left(\Phi m^k, \frac{1}{\sigma_v^2} I_{3|\Omega|}\right). \quad (3.8)$$

We further assume that the polyaffine parameter m^k follow a normal probability distribution,

$$m^k \sim \mathcal{N}(\mu, \Gamma), \quad (3.9)$$

where μ is the population mean and Γ is the $12N \times 12N$ concentration matrix (inverse of the covariance matrix). The posterior distribution of m^k is normal distributed, since both the prior on m^k and the distribution on \mathbf{v}^k are normal distributions. In Bayesian statistics, if the prior and the posterior are from the same family (in our case the exponential family) then the prior and posterior are called conjugate distributions, and the prior is called conjugate prior. This allows us to analytically derive the posterior probability for polyaffine parameters for patient k ,

$$m^k | \mathbf{v}^k, \mu, \Gamma \sim \mathcal{N}(\check{\mu}, \check{\Gamma}), \quad (3.10)$$

where $\check{\mu}$ and $\check{\Gamma}$ are posterior mean and concentration matrix, respectively. Let us now write this posterior probability (using Bayes' theorem) of m^k given the observed

velocity field \mathbf{v}^k , and the parameter of the prior μ , Γ for one patient k (modulo constants),

$$P(m^k | \mathbf{v}^k, \mu, \Gamma) \propto \exp \left(-\frac{1}{2} [(\mathbf{v}^k - \Phi m^k)^\top \frac{1}{\sigma_v^2} I_{3|\Omega|} (\mathbf{v}^k - \Phi m^k) + (m^k - \mu)^\top \Gamma (m^k - \mu)] \right) \quad (3.11)$$

Since both distributions are normal distributions, we obtain a normal posterior in the form of,

$$P(m^k | \mathbf{v}^k, \mu, \Gamma) \propto \exp \left(-\frac{1}{2} (m^k - \check{\mu})^\top \check{\Gamma} (m^k - \check{\mu}) \right). \quad (3.12)$$

To find the parameter of the posterior normal distribution we use the ‘‘completing the squares’’ method (as for instance used in [Gelman 2003]). We rearrange Equation (3.11) with respect to m^k into the form of Equation (3.12), and after pulling out the constant factors, we obtain,

$$\check{\mu} = \check{\Gamma}^{-1} \left(\frac{1}{\sigma_v^2} \Phi^\top \mathbf{v}^k + \Gamma \mu \right) \quad \text{with} \quad \check{\Gamma} = \frac{1}{\sigma_v^2} \Phi^\top \Phi + \Gamma. \quad (3.13)$$

As we can see the posterior mean is a weighted average of the SVF and the prior mean, with weights given by the $\check{\Gamma}^{-1} \frac{1}{\sigma_v^2} \Phi^\top$ and $\check{\Gamma}^{-1} \Gamma$, respectively. The posterior concentration matrix is the sum of $\frac{1}{\sigma_v^2} \Phi^\top \Phi$ and the prior concentration. Now we can easily identify the MAP estimate of m^k as,

$$m_{\text{MAP}}^k = \check{\mu}, \quad (3.14)$$

in the absence of noise it is,

$$m_{\text{MAP}}^k = (\Phi^\top \Phi)^{-1} \Phi^\top \mathbf{v}^k \quad (\text{if } \sigma_v^2 = 0), \quad (3.15)$$

and with $\sigma_v^2 = \infty$, we obtain,

$$m_{\text{MAP}}^k = \mu \quad (\text{if } \sigma_v^2 = \infty). \quad (3.16)$$

We propose to estimate each m_{MAP}^k separately for each patient k , thus assuming the independence of SVFs across subjects,

$$P(m^{[k]} | \mathbf{v}^{[k]}, \mu, \Gamma) = \prod_{k=1}^K P(m^k | \mathbf{v}^k, \mu, \Gamma). \quad (3.17)$$

This assumption is only valid if the template with which the patients are registered is unbiased. In this work, we chose the template according to visual inspection.

3.3.2 Sample Covariance Matrix Inverse

In the previous section, we assumed the parameter μ and Γ for the prior distribution were known. Here we propose to use the coarse to fine registration approach introduced in [Seiler 2012c] to compute these parameters. The first step is to compute

the covariance matrix of polyaffine parameter obtained from [Seiler 2012c]. The sample covariance matrix of polyaffine parameter is given by,

$$\text{Cov} = \frac{1}{K} \sum_k (\hat{m}^k - \bar{m})(\hat{m}^k - \bar{m})^\top \quad \text{with} \quad \bar{m} = \frac{1}{K} \sum_k \hat{m}^k, \quad (3.18)$$

where \bar{m} is the sample mean, and we denote the polyaffine parameter obtained through the method described in [Seiler 2012c] as \hat{m}^k . In a second step we need to invert the covariance matrix to obtain the concentration matrix Γ that is used in Equation (3.13). The problem is that the inverse of the covariance is not robust, since we have only few samples (in our case 42) and a high number of variables (in our case 372). In addition to the number of samples problem we have elements in the covariance matrix with very different scales. The linear parts of the polyaffine parameters are much smaller than the one for the translational part. This causes numerical problems when taking the Cholesky inverse of the covariance matrix. To remedy this we use information about the structure of the covariance matrix and assume conditional independence between regions.

The inverse of the sample covariance of polyaffine parameter has an inherent block structure due to the regions,

$$\Gamma = \text{Cov}^{-1} = \begin{bmatrix} \Gamma_{11} & \dots & \Gamma_{1N} \\ \vdots & \ddots & \vdots \\ \Gamma_{N1} & \dots & \Gamma_{NN} \end{bmatrix}, \quad (3.19)$$

where each block Γ_{ij} is a 12×12 matrix, and the number of blocks are equal to N^2 . Off-diagonal blocks represent connections between regions, whereas blocks along the diagonal are connections within each polyaffine parameter region. The inverse of the covariance matrix and these connections have a statistical meaning. If an off-diagonal block Γ_{ij} is zero, then region i and j are conditionally independent. Two variables are conditionally independent if there is no direct or indirect relation between them. Conditional independence is stronger than independence, since it also considers indirect relations. Methods such as Graphical Lasso [Friedman 2008, Banerjee 2008] are examples where covariance matrices are inverted to find these conditional independencies among variables. The objective of Graphical Lasso is to find a sparse graph describing conditional independences of variables.

In this paper, we focus on the block diagonal elements only and thus assume conditional independence of polyaffine parameters between all regions. It will be interesting to relax this assumption in future work to explore structural relations between regions. In the next two sections, we propose two methods to take the inverse of covariance matrices in our context.

3.3.2.1 Blockwise Diagonal Inverse

To ensure numerical stability for the covariance matrix inverse, we propose to take advantage of the region structure by inverting the block diagonal of the covariance

matrix,

$$\Gamma = \text{diag}(\text{Cov}_i^{-1}) = \begin{bmatrix} \text{Cov}_1^{-1} & \dots & 0 \\ \vdots & \ddots & \vdots \\ 0 & \dots & \text{Cov}_N^{-1} \end{bmatrix}. \quad (3.20)$$

This implicitly assumes conditional independence of all regions.

3.3.2.2 Kronecker Product Blockwise Diagonal Inverse

As in the first method described in the previous section, we propose to take advantage of the region structure, which reflects as a blockwise structure in the covariance matrix. In addition, we use the Kronecker product to decompose the covariance matrix into two parts, the polyaffine parameter per regions and a scaling factor. We develop a blockwise pseudoinverse,

$$\Gamma = \text{diag}(\alpha_i^+ \otimes C^{-1}) = \begin{bmatrix} \alpha_1^+ C^{-1} & \dots & 0 \\ \vdots & \ddots & \vdots \\ 0 & \dots & \alpha_N^+ C^{-1} \end{bmatrix}, \quad (3.21)$$

where \cdot^+ is the pseudoinverse, α_i is a scalar of the block i (i.e. region i), and C is a 12×12 matrix, representing the metric of the polyaffine parameter, e.g. how translation and linear parameters interact with each other. We optimize,

$$\{\hat{\alpha}_i, \hat{C}\} = \underset{C, \alpha_i}{\text{argmin}} \sum_i^N \|\text{Cov}_{ii} - \alpha_i C\|^2, \quad (3.22)$$

in two sequentially steps. In step one, for C with fixed $\forall i : \alpha_i = 1$, and in step two for α_i with fixed C obtained from the previous step. We derive the cost function with respect to α_i and C and set it to zero, to obtain optimal estimates \hat{C} and $\hat{\alpha}_i$,

$$\text{Step one: } \hat{C} = \frac{\sum_{i=1}^N \alpha_i \text{Cov}_{ii}}{\sum_{i=1}^N \alpha_i^2}, \quad \text{Step two: } \hat{\alpha}_i = \frac{\text{Trace}(\text{Cov}_{ii} C)}{\text{Trace}(C^2)}. \quad (3.23)$$

By constraining the matrix C to be fixed for all diagonal blocks of Γ we intend to lower the risk of overfitting.

3.4 Experiments on Real CT Data

In this section, we register 42 mandible CT images to a template and evaluate the resulting transformations. The template is chosen through visual inspection of all images. We register five levels and generate 31 regions using the weighted OBBTree algorithm presented in [Seiler 2012c]. The resulting weights are shown in Fig. 3.3, where each ellipsoid represents a Gaussian weight thresholded at σ . The algorithm splits the mandible bone into front and back part at level 1, followed by a split into left and right side at level 2. After further refinement at level 3, the algorithm splits

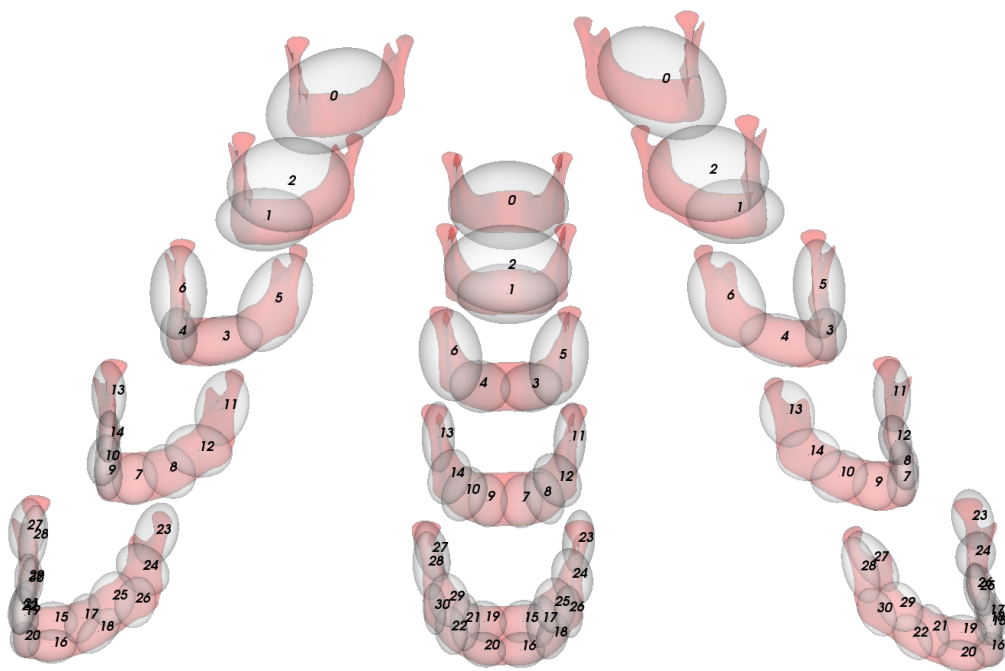


Figure 3.3: Three different views of 31 regions across 5 levels considered for the registration. Each Gaussian weight represents one region and is visualized as one ellipsoids thresholded at σ .

the mandible into upper and lower part at level 4 (finest level). The regions are computed prior to the registration and can vary for different templates.

To study the characteristics of polyaffine parameter, we first decompose each log affine transformation into three parts: expansion, rotation and translation. The theorem of Helmholtz states that the most general motion of a sufficiently small non-rigid body can be represented by,

$$\text{Expansion: } \frac{1}{2}(\tilde{M}_i + \tilde{M}_i^\top), \quad \text{Rotation: } \frac{1}{2}(\tilde{M}_i - \tilde{M}_i^\top), \quad \text{Translation: } \log(t_i),$$

where the expansion is measured along the three orthogonal directions, and the decomposition of the linear part into skew symmetric and symmetric matrices (representing expansion and rotation, respectively) is given by,

$$\tilde{M}_i = \frac{1}{2}(\tilde{M}_i + \tilde{M}_i^\top) + \frac{1}{2}(\tilde{M}_i - \tilde{M}_i^\top).$$

Second, it can be shown, for example using the Jordan (or Schur) decomposition of matrix \tilde{M}_i , that the following equality provides us with the determinant of linear transformations (for any square matrix with a principal logarithm),

$$\det(A_i) = \exp(\text{Trace}(\tilde{M}_i)).$$

In the next section we use the volume change, rotation and translation characteristics to evaluate the polyaffine parameter for a wide range of noise parameter σ_v^2 and the two covariance matrix inversion methods. Since each \tilde{M}_i is weighted with its corresponding weight function $w_i(x)$ at spatial position x , we evaluate only the transformation at the center of each region,

$$\tilde{M}_{i,\max} = w_i(\hat{x}_i)\tilde{M}_i \quad \text{with} \quad \hat{x}_i = \underset{x_i}{\text{argmax}}\{w_i(x_i)\}. \quad (3.24)$$

In Figs. 3.5 and 3.6, we compared the following characteristics at the center point of each region i ,

$$\text{Volume change:} \quad \exp(\text{Trace}(\tilde{M}_{i,\max})), \quad (3.25)$$

$$\text{Measure of rotation:} \quad \left\| \frac{1}{2}(\tilde{M}_{i,\max} - \tilde{M}_{i,\max}^\top) \right\|_F, \quad (3.26)$$

$$\text{Measure of translation:} \quad \left\| \log(t_{i,\max}) \right\|, \quad (3.27)$$

where we use the Frobenius norm of the rotation part and the L^2 -norm of the translation part.

3.4.1 Comparison of Sample Covariance Inverse Methods

In Sections 3.3.2.1 and 3.3.2.2, we presented two methods to compute the inverse of covariance matrices. In this section we compare the results that we obtained for the two methods in terms of three transformation characteristics: determinant (volume change), rotation and translation. We performed 42 manual segmentation

on all images. The segmentation classifies bone and non-bone voxels. From this we compute the following scores between all 41 images to the template: Dice coefficient of the segmented images and contour mean distance between segmented images. More refined segmentations subdividing the bone into different regions, as suggested for instance in [Rohlfing 2012], are planned for future validation experiments.

In the following we refer to the block diagonal inverse as Block-Inv, and to the Kronecker Product Blockwise Diagonal Inverse as Kron-Inv. With the experiments we address the following questions:

- What is the optimal noise parameter σ_v^2 ?
- According to Equation (3.16), we expect a shrinkage towards the prior mean with increasing noise. Is this observable in the experiments?
- What are the differences between Block-Inv and Kron-Inv?
- Are there regions with high variability? What caused this high variability?

Figure 3.4 compares a wide range, $\sigma_v^2 = \{0, 0.5^2, 1^2, 2^2, \dots, 32^2\}$ mm, of noise parameter. The best accuracy in terms of Dice coefficient and contour mean distance are obtained with 4^2 for Block-Inv. In method Kron-Inv, the optimal Dice coefficient is at 1^2 and even lower at 0.5^2 for the contour mean distance. To recall, the parameter σ_v^2 describes the independent noise level at each voxel in all three directions. Thus the optimal noise assumptions according to the Dice coefficients for Block-Inv and Kron-Inv are 4 and 1 mm, respectively. We conjecture that the lower σ_v^2 for Kron-Inv is caused by the averaging of block diagonal matrices, which regularizes the inverse covariance matrix.

According to Equation (3.16) from Section 3.3.1, we expect that a higher noise parameter shrinks the estimates towards the prior mean. This effect is observed in both inversion methods. Figure 3.5 shows the shrinkage for both inverse methods in terms of the volume change of regions, as can be seen, the higher the noise the lower the variability of the transformations. The axis labels in the plots correspond to the region labels in Fig. 3.3.

Figure 3.6 shows the three different deformation characteristics that we previously introduced: determinant (volume change), rotation and translation. The left column shows the results obtained with Block-Inv. For region 0 to 14 (level 0 to 3), we observe only a small variation from the identity transform, almost 1 for determinants and close to 0 for rotation and translation part. In contrast, in regions 15 to 30 (level 4), we observe determinants between 0.5 to 2 (with two outliers around 3), and higher median and variability for rotation and translation part. Figure 3.7 shows how this reflects in the two performance scores across levels. For the Dice coefficient and contour mean distance, the levels 0 to 3 provide almost nothing to the improvement of the score, all the work is done at level 4.

The right column of Fig. 3.6 shows results obtained with Kron-Inv. We can observe two interesting points. First, region 2 shows a high variability. This makes sense, in Fig. 3.3, region 2 is the back part of the mandible containing two distant

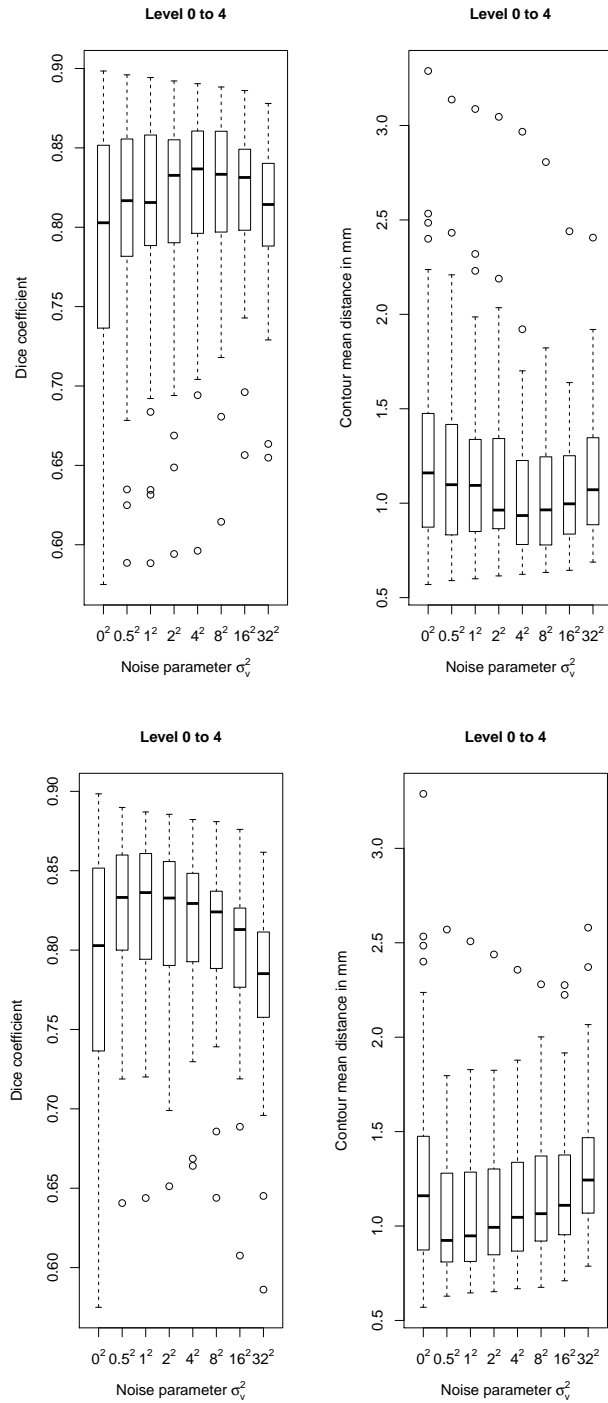


Figure 3.4: Comparison of registration accuracy in terms of Dice coefficient and contour mean distance. Scores over a wide range of noise parameter σ_v^2 . **Top row:** Blockwise Diagonal Inverse (Block-Inv). **Bottom row:** Kronecker Product Blockwise Diagonal Inverse (Kron-Inv).

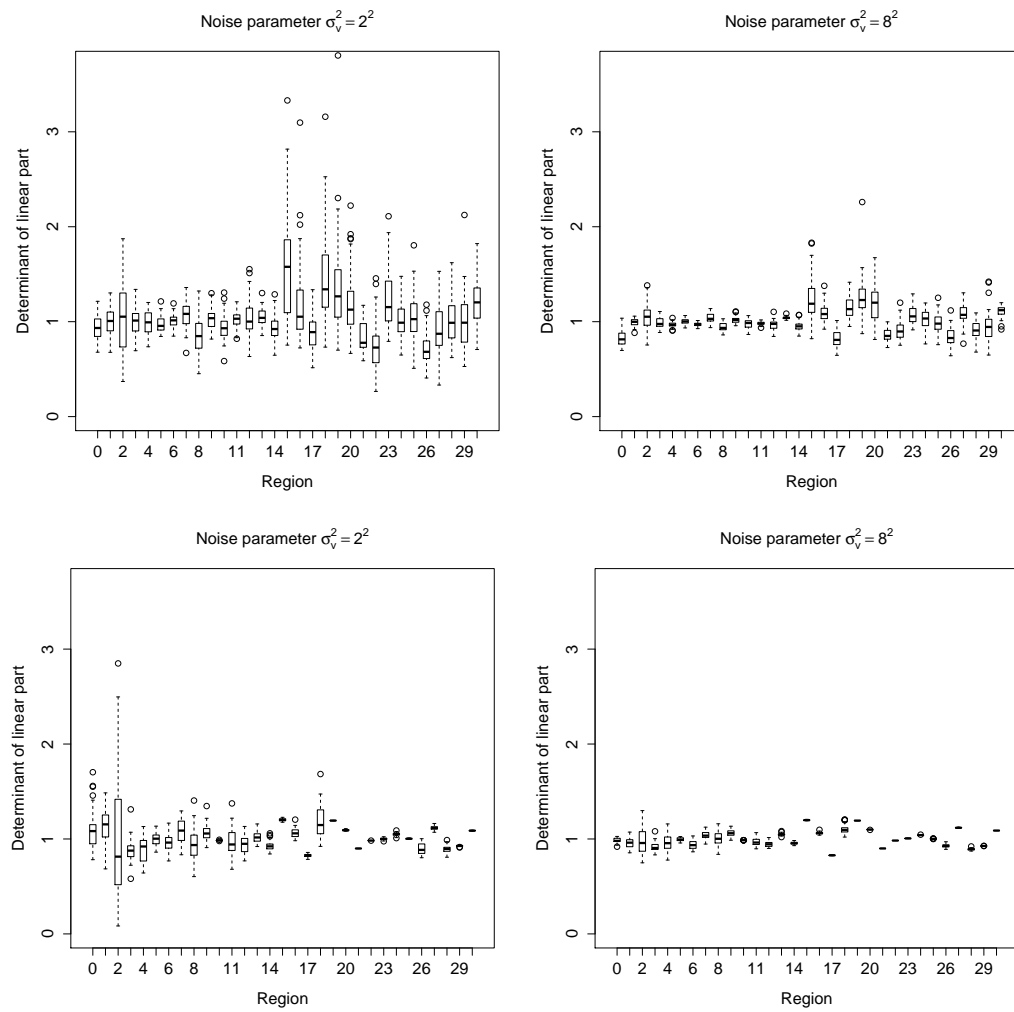


Figure 3.5: Statistics of the determinant of regions with noise parameter set to $\sigma_v^2 = 2^2$ and $\sigma_v^2 = 8^2$. The axis labels correspond to the region labels in Fig. 3.3. **Top row:** Blockwise Diagonal Inverse (Block-Inv). **Bottom row:** Kronecker Product Blockwise Diagonal Inverse (Kron-Inv). As expected from Equation (3.16), the shrinkage towards the prior mean increases with increasing amount of noise.

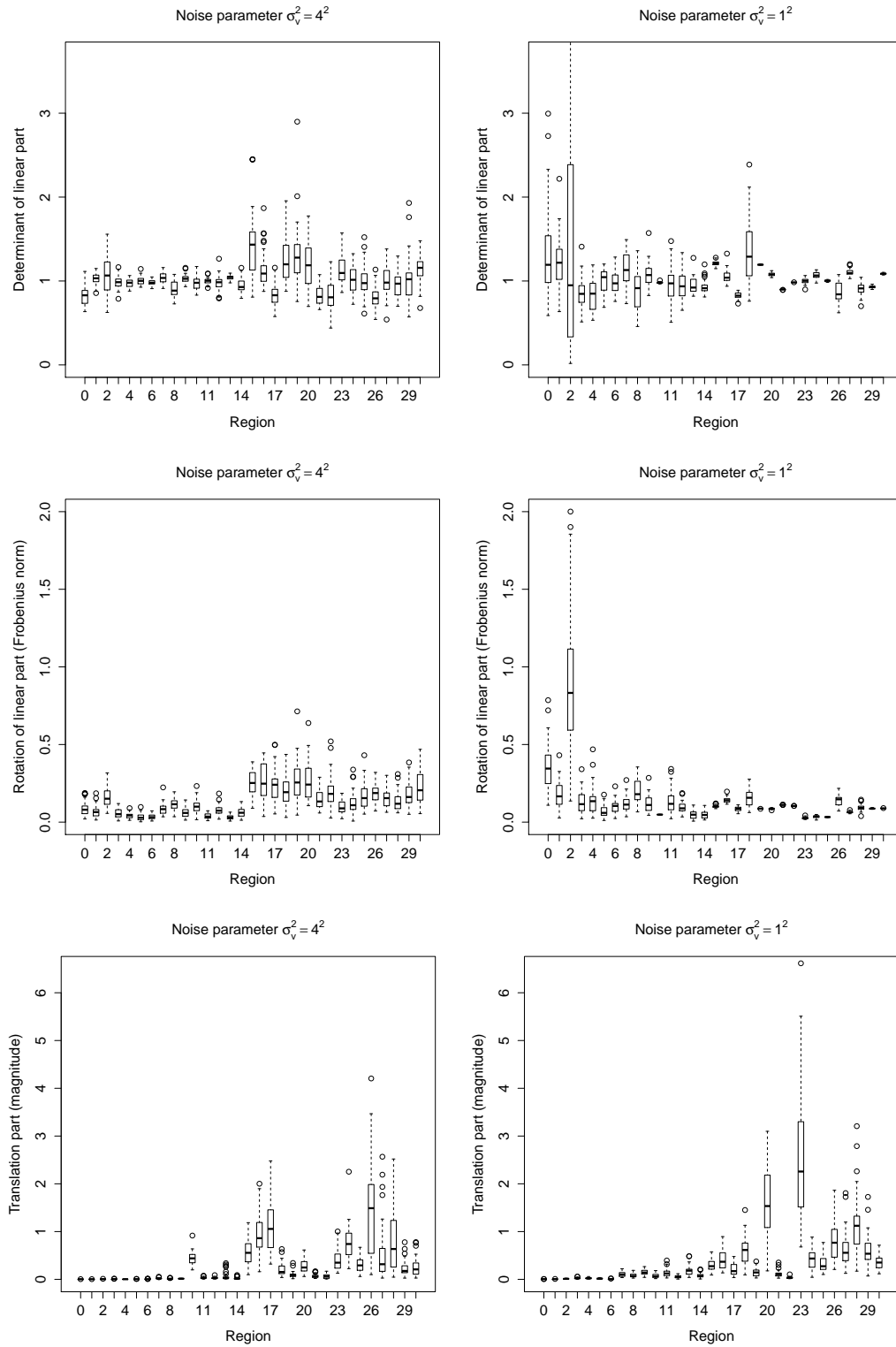


Figure 3.6: Statistics of the determinant, rotation and translation. **Left column:** Block-Inv with $\sigma_v^2 = 4^2$. **Right column:** Kron-Inv with $\sigma_v^2 = 1^2$. Region 2 in the top plot reaches up to 5 with 2 outliers.

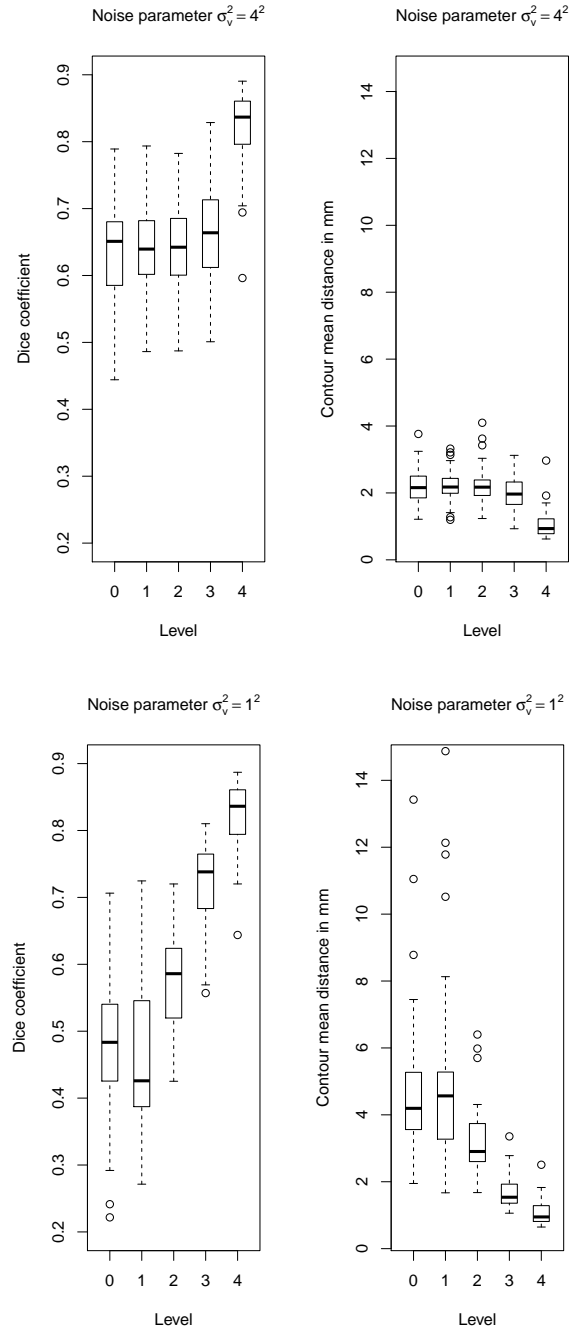


Figure 3.7: Comparison of registration accuracy in terms of Dice coefficient and contour mean distance. Scores on registrations with optimal noise parameter $\sigma_v^2 = 324$. **Top row:** Blockwise Diagonal Inverse (Block-Inv). **Bottom row:** Kronecker Product Blockwise Diagonal Inverse (Kron-Inv).

sides (coronoid, condylar process and head, and part of angle and ramus regions). We expect this registration to be difficult and thus to yield a high uncertainty of the resulting deformation parameter. The second interesting point is the high variability of determinants and rotations for levels 0 to 3, with low variability in level 4, and the low variability of the translation part in levels 0 to 3, with high variability for level 4. This indicates that regions at the coarser levels are rotated and expanded (or shrunk), and the finer regions are translated. Figure 3.7, shows a gradual improvement of the scores with increasing levels (expect the difficult region 2 at level 1), reflecting the more uniform distribution of polyaffine parameter over all regions and levels.

3.5 Discussion and Conclusion

In this work, we presented a multiscale polyaffine registration method that simultaneously registers all scales. We showed a GLM for polyaffine deformations, which we used to create a generative statistical model. This allowed us to incorporate a prior in a Bayesian framework. The results with prior increased registration accuracy in terms of Dice coefficient and contour mean distance, and controls the robustness of polyaffine parameter estimates in terms of determinants, rotation and translation measured for each region. This suggest that we avoid a local solutions by incorporated deformations statistics.

The proposed multiscale registration depends on the selection of the noise parameter σ_v^2 . We showed that it can be found by computing a range of values and evaluating it with respect to a performance measure. This parameter represents the variance of stationary velocity vectors. Its optimal values for the two inverse methods on our mandible dataset were found to be $\sigma_v^2 = 4^2$ and $\sigma_v^2 = 1$ mm for Block-Inv and Kron-Inv, respectively. Several interesting conclusion from the results could be made. First, as expected with higher noise parameter the variability of the deformation parameter was reduced. Second, the variability was high in regions where we expect the log-demons to have difficulty to find a good correspondence. Particularly interesting was one observation for Kron-Inv, where we could see that the variability of volume change and rotation is high for level 0 to 3, whereas the translation is high in level 4. This suggests that for Kron-Inv, coarser regions mainly differ in terms of the linear part and finer regions in terms of the translation part of the polyaffine parameter. This is consistent with other medical image registration algorithms, if we consider the special case of one region per voxel, where one tries to find a translation of each voxel.

The block structure of the covariance matrix has an interpretation in terms of the anatomy. Each 12×12 block represent one region, the off-diagonal blocks represent the covariance between two regions. Furthermore, the inverse of the covariance matrix gives us conditional independences between regions, which indicates anatomical relations between parts of the anatomy. In the presented paper, we limited our concentration matrix to be block diagonal, removing all relations between regions.

We plan to work on an extension to include the off-diagonal blocks in the concentration matrix as well. The long term objective is to consider the prior mean μ and the prior concentration Γ not as fixed parameters but as hyperpriors with their own distributions. In Bayesian statistics, hyperpriors represent prior distributions on hyperparameters, which are the parameter of the prior distribution. A possible choice of hyperpriors can be found in [Wang 2009, Wang 2012]. With the inclusion of hyperpriors we will need to move from the analytical closed form solutions to posterior computations using Markov Chain Monte Carlo methods.

An intermediate step before moving to Monte Carlo simulations could be to assume sparsity of the region relations and invert the sample covariance matrix with the Graphical Lasso [Friedman 2008, Banerjee 2008], or its extensions to structured matrices using the Kronecker product [Werner 2008, Tsiligkaridis 2012]. In the case of mandibles, this kind of sparse relations between regions are largely unexplored in the clinical setting and thus provide no way to validate new results. Therefore, we first plan to investigate articulated structures, where the relations are better known.

We believe that our approach is more than just an extension of [Ashburner 1997]. By considering not only one affine component, but a mixture of components acting at different scales, we are moving the discussion into structured learning, which to our knowledge is a novelty in the medical registration community. In future work, we plan to introduce a sparse representation of anatomical substructures and their connection at different scales, which might uncover structures equivalent to rigid articulated bodies.

Clinical Applications

The methods we developed in previous chapters were found to be helpful in a wide range of clinical applications that we summarize in this chapter. The first section in this chapter shows an abstract on symmetry assessment of bones, which we presented at Computer Assisted Orthopaedic Surgery (CAOS), a well respected clinical conference in the field of orthopaedic surgery [Seiler 2009b]. The second section, is a conference paper [Seiler 2010b] on regression of geometrical deformations. It relates the femur shaft length and caput collum diaphysis angle to SVFs computed using the standard log-demons.

The remainder of this chapter describes collaborative work conducted at four different research institutions in five different fields of application. The work on orthopaedic fracture risk and implant design for femurs was performed at the University of Bern in collaboration with Serena Bonaretti [Bonaretti 2011, Bonaretti 2010]. The interesting clinical task of allograft selection was approached with Lucas Ritacco, Italian Hospital of Buenos Aires, Argentina, and led to a publication in a clinical journal [Ritacco 2012]. In collaboration with Habib Bou-Sleiman, University of Bern, we published work on implant design for mandibles [Bou-Sleiman 2012]. In collaboration with Rémi Blanc from the ETH in Zurich, we worked on conditional shape models and regression models for orthopaedic research, which resulted in two publications [Blanc 2009, Blanc 2012]. Together with Kristin McLeod from Asclepios at INRIA Sophia Antipolis, we extended our method to consider additional constraints important for heart modeling, the results were published in [McLeod 2012]. In all projects our ITK implementation (Appendix C) built the basis for the collaboration.

Contents

4.1	Left-Right Symmetry in Femur and Tibia Bones	68
4.2	Regression of Geometrical Deformations in Femur Bones .	71
4.3	Biomechanics of Femur Bones	78
4.4	Allograft Selection for Femur Bones	80
4.5	Implant Shape Design for Mandible Bones	82
4.6	Prediction of Bone Surface for Orthopaedic Research . . .	83
4.7	Heart Modeling with Incompressibility Constraints	85

4.1 Left-Right Symmetry in Femur and Tibia Bones

This abstract was presented at the international conference on Computer Assisted Orthopaedic Surgery (CAOS) [Seiler 2009b].

Abstract

Optimal reproduction of normal femur and tibia anatomy is one of the prerequisites for successful designing implants. Usually implant design is based upon an average anatomy. However, little is known, apart from size, on the shape variability of tibia and femur anatomy in different populations. Although there is limited evidence to suggest that there are differences in symmetry between left and right, to our knowledge it has not been yet qualitatively proven. Hence, in order to highlight potential important factors of symmetry in implant design, more detailed knowledge is necessary. This work presents, based upon information from a large virtual bone database, a systematic analysis for left and right variations in femur and tibia anatomy.

Methods

Recent advances in quantitative computed tomography (CT) image post processing have enabled researchers to quantify variations in bone morphology between individual patients and population groups [Kozic 2008]. In this study, shape analysis techniques are utilized to extract femur and tibia anatomical landmarks between left and right for male and female Caucasian population groups. Equipped with this data, statistical comparisons between these groups are made to establish their statistical significance.

The proposed methodology was applied to a dataset of 72/71 male and 94/91 female left/right femur CT bone scans and patient age range of 21 to 93 years. For tibia bones the datasets consists of 68/66 male and 88/87 female and patient age range of 17 to 90 years. All patient were Caucasians.

Image segmentation was performed in a semi-automatic fashion in order to extract the outer shell of the femur and tibia bones. After image segmentation, reference images are selected for femur and tibia and a combined affine and non-rigid image registration [Vercauteren 2007] approach is employed to establish corresponding anatomical points across the images. Given a point x in the reference image we aim at finding the corresponding point x' such as $x' = A^{-1}(\phi^{-1}(x))$, where A and ϕ are respectively the affine and non-rigid transformations needed to morph every image into the reference one. The affine transformation allows us to deal with coarse deformations, whereas the non-rigid transformation captures the local shape variations. Landmarks are selected interactively through a Graphical User Interface on which the reference bone is displayed in a 3-D space. Consequently, distances can be propagated automatically across all the images. In addition, the landmark selection process was extended to generate cutting planes on which new measurements are

Table 4.1: Results of t-tests for left and right on femur male Caucasian.

Measurement	Left $\mu \pm \sigma$	Right $\mu \pm \sigma$	P-value
Bone length [mm]	437.66 ± 20.22	433.99 ± 18.59	0.26
Antetorsion angle [°]	15.29 ± 2.38	19.72 ± 2.97	< 0.05
CCD angle [°]	114.94 ± 3.83	132.05 ± 5.23	< 0.05
IC distance [mm]	61.47 ± 4.01	52.86 ± 3.34	< 0.05

Table 4.2: Results of t-tests for left and right on femur female Caucasian.

Measurement	Left $\mu \pm \sigma$	Right $\mu \pm \sigma$	P-value
Bone length [mm]	415.42 ± 17.96	413.36 ± 18.11	0.44
Antetorsion angle [°]	14.42 ± 2.44	19.98 ± 3.04	< 0.05
CCD angle [°]	116.82 ± 5.38	133.74 ± 5.19	< 0.05
IC distance [mm]	53.49 ± 4.14	46.43 ± 3.32	< 0.05

defined. The following anatomical measurements were extracted from femur and tibia bones:

- Femur: Bone length, antetorsion angle, Caput Collum Diaphysis (CCD) angle and Inter-Condyles (IC) distance.
- Tibia: Bone length, plateau height, plateau slope and plateau width.

These measurements are extracted automatically and stored for statistical analysis.

Results

To test the similarity between left and right datasets we chose the unpaired t-test, thus we assume a normal distribution and a similar variance. We perform unpaired tests, since the amount of bones for each side is not the same. We reject the null hypothesis when the p-values are below 0.05. The statistics for femurs, Tabs. 4.1 and 4.2, shows asymmetry in all measurements except the bone length. For tibias, Tabs. 4.3 and 4.4, plateau height and slope are asymmetric.

Table 4.3: Results of t-tests for left and right on tibia male Caucasian.

Measurement	Left $\mu \pm \sigma$	Right $\mu \pm \sigma$	P-value
Bone length [mm]	363.51 ± 18.31	369.43 ± 19.50	0.07
Plateau height [mm]	63.65 ± 3.82	66.47 ± 3.91	< 0.05
Plateau slope [°]	14.96 ± 1.68	13.35 ± 1.39	< 0.05
Plateau width [mm]	82.21 ± 3.97	81.64 ± 4.85	0.46

Table 4.4: Results of t-tests for left and right on tibia female Caucasian.

Measurement	Left $\mu \pm \sigma$	Right $\mu \pm \sigma$	P-value
Bone length [mm]	345.88 ± 18.26	350.94 ± 18.55	0.07
Plateau height [mm]	55.83 ± 3.43	57.54 ± 4.40	< 0.05
Plateau slope [°]	15.29 ± 2.63	14.48 ± 2.26	< 0.05
Plateau width [mm]	73.85 ± 3.39	73.97 ± 3.33	0.80

Discussion

A significant difference between left and right femur and tibia measurements was found in male and female Caucasian groups. The results showed that the symmetry is independent of the gender; in all statistical tests we obtained the same results for female and male bones. The length shows in both bones a significant symmetry. Interestingly, all plateau landmarks are symmetric but the width.

The automatic propagation of anatomical landmarks provides us with a powerful tool able to analyze large datasets in a fast and accurate way, avoiding error prone manual measurements.

In the future it will be interesting to look at symmetry differences between ethnic groups.

4.2 Regression of Geometrical Deformations in Femur Bones

This section was published as a conference paper in [Seiler 2010b].

Abstract

Currently there is an increase usage of CT-based bone diagnosis because low-radiation and cost-effective 2D imaging modalities do not provide the necessary 3D information for bone diagnosis. The fundamental objective of our work is to build a model connecting 2D X-ray information to 3D CT information through regression. As a first step we propose an univariate non-parametric regression on individual predictor variables to explore the non-linearity of the data. To later combine these univariate models we then replace them with parametric models. We examine two predictors, shaft length and caput collum diaphysis angle on a database of 182 CT images of femurs. We show that for each predictor it is possible to describe 99% of the variance through a simple up to second order parametric model. These findings will allow us to extend to the multivariate case in the future.

Introduction

Up to now, 3D bone anatomy has been generated from X-ray images using computational tools. However these tools have focused only on 3D bone shape reconstruction while little attention has been given to 3D reconstruction of bone mineral density, which is important in analysis of bone fragility, orthopaedic surgery, orthopaedic implant design, etc. We hypothesize that full 3D bone anatomy (i.e. bone shape and bone mineral density) for X-ray based diagnosis can be achieved through development of computational and statistical tools, making use of vast amount of femur CT images.

The fundamental objective is to perform multivariate regression on the anatomy of bones. As predictors, the regression model uses patient-specific metadata (e.g. age, weight, body mass index, etc.), and image features extracted from patient radiographs. The variables to predict are patient-specific 3D CT images of bones. As a first step, in this paper we propose univariate parametric regression models based on the exploration of non-parametric regression results for femur bones on a selected subset of clinically meaningful morphological parameters: Femoral shaft length depicted in Fig. 4.1 (a,b) and caput collum diaphysis (CCD) angle in Fig. 4.1 (c).

Currently in medical image regression, parametric (e.g. [Yang 2008, Rao 2008, Liu 2004]) and non-parametric (e.g. [Davis 2007]) approaches have been employed.

- On one hand, parametric-based approaches can be utilized for multivariate regression without encountering the curse of dimensionality problem, but its use pre-imposes a statistical structure on the data.

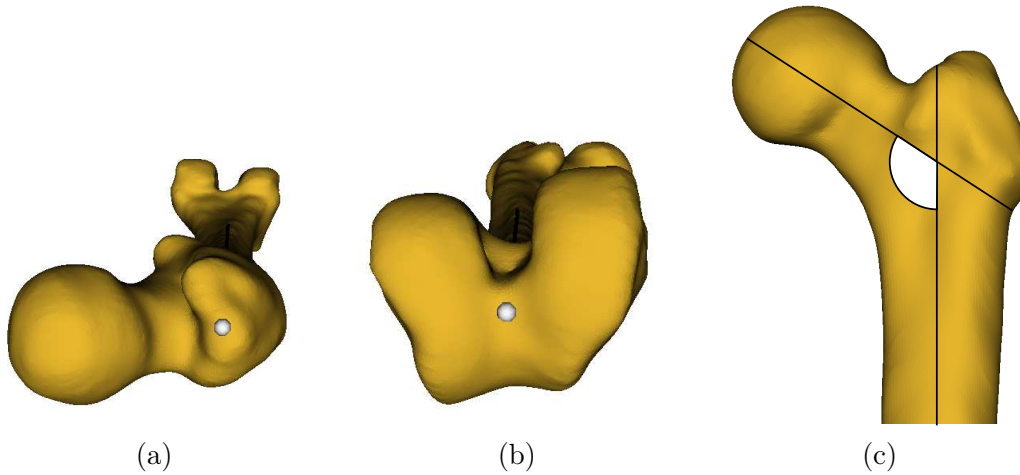


Figure 4.1: (a) Starting point of shaft length morphological parameter at the greater trochanter. (b) End point between condyles. (c) CCD angle.

- On the other hand, non-parametric approaches do not impose a certain structure, but they suffer from the curse of dimensionality when trying to optimize for hyper-parameters in high-dimensional spaces. However, provided low-dimension subspaces can be found, efficient optimization could be performed. Nevertheless, this is still an open research question [Gerber 2009, Steinke 2009].

Therefore, we selectively combine these two approaches to solve the problem in a low-dimensional space, without pre-imposing a statistical data structure. For this goal we propose a two-step approach. First, we explore the data structure through univariate non-parametric regression. This step enforces no assumptions on the data structure while avoiding the curse of dimensionality problem. Second, we parametrize the explored structures.

In [Davis 2007] the authors showed kernel regression formulated with Fréchet weighted means to take into account the non-Euclidean nature of diffeomorphisms endowed with a right invariant metric (LDDMM) and applied it to images of the brain. In contrast, in this work we formulate kernel regression in an Euclidean way in a Log-Euclidean framework. This simplifies and speeds-up the process significantly while still taking into account a large part of the non-Euclidean nature of the manifold-valued data. Furthermore, this simplification allows for other computations that are out of reach to LDDMM, such as determining the optimal kernel bandwidth through cross-validation. The Log-Euclidean framework uses stationary velocity fields to parametrize a diffeomorphic deformation, whereas in [Davis 2007] non-stationary velocity fields are used. Although the theory shows that not all diffeomorphic deformation can be reached with stationary velocity fields; there is no indication so far that this affects the anatomical shape analysis in any way.

In the following, we develop the methodology and show results obtained on femur

CT images.

Methods

The methods description will be divided in five parts: Log-domain registration, Log-Euclidean statistics, non-parametric kernel regression, cross-validation and parametrization of principal component (PC) scores.

Log-Domain Registration

To setup correspondences between anatomical images, a set of images are registered to a reference. We use the novel symmetric diffeomorphic registration approach described in [Vercauteren 2008]. What is new in this registration framework is the efficient optimization in the log-domain. As a consequence, the results of the registration are so-called stationary velocity fields. These velocity fields can be looked at as generators for diffeomorphic deformations through the group exponential map that can be very efficiently computed using the scaling and squaring method [Arsigny 2006].

Log-Euclidean Statistics

Applying the Log-Euclidean framework [Arsigny 2006] on these fields allows us to compute statistics, e.g. averages, and still preserve diffeomorphism. In the Log-Euclidean framework, velocity fields are regular elements in a vector space; this allows us to use simple Euclidean statistics instead of more complex non-linear techniques, which we needed when working in the LDDMM space of diffeomorphic transformations. To map resulting velocity fields into diffeomorphic transformations the exponential is calculated. To go from diffeomorphic transformation back to velocity fields, a logarithmic mapping is performed. However, in many cases the intrinsic parametrization of the transformation by its log in the log-domain registration allows to avoid this numerically unstable step. For a detailed survey of the methodology we refer to [Pennec 2008].

Non-Parametric Kernel Regression

We use a kernel regression method to compute the deformation of the template that best predicts the images based on prediction variables x , in our case shaft length and CCD angle. Our kernel regression function is

$$\hat{m}_\sigma(x) = \exp \left(\frac{\sum_{i=1}^N K_\sigma(x - x_i) v_i}{\sum_{i=1}^N K_\sigma(x - x_i)} \right), \quad (4.1)$$

where N , x_i , K_σ , \exp and v_i are the total number of images, shaft length or CCD angle for image i , a Gaussian kernel function with σ bandwidth, the mapping from velocity fields to diffeomorphic deformations and the i^{th} velocity field, respectively.

Cross-Validation

The quality of kernel regression methods strongly depends on the selection of bandwidth parameters. To select a bandwidth parameter we apply cross-validation with penalty functions. The penalty and corresponding weighting functions penalize very small bandwidth values. Bandwidth values equal to zero are not interesting because they are just a nearest neighbor interpolation of the data. In our case we solve the following minimization problem:

$$\hat{\sigma} = \operatorname{argmin}_{\sigma \in \mathbb{R}} \sum_{i=1}^N \|\log(\hat{m}_{\sigma}(x_i)) - v_i\|^2 \Xi(W_{\sigma,i}(x_i)), \quad (4.2)$$

where N , \log , σ , Ξ are total number of images, mapping from diffeomorphic deformations to velocity fields, bandwidth and penalty function, respectively, and $W_{\sigma,i}(x_i) = K_1(0) / \sum_{j=1}^N K_1(\sigma^{-1}(x_i - x_j))$ is the weighting function. For details we refer to [Härdle 1992]. By solving this optimization problem we obtain a kernel bandwidth greater than zero which minimizes the regression function's prediction error for all images N .

Parametrization of Univariate Kernel Regression

To parametrize the non-linear regression function that we have established via kernel regression, the regressed velocity fields are reduced in dimension using principle component analysis (PCA). The data points are then projected onto a low-dimensional space covering 99% of the variance and evaluated for possible parametrization. In all cases that we have observed so far it is possible to fit a polynomial to each PC. The procedure can be summarized as follows:

1. Regress velocity fields
2. PCA on regressed velocity fields
3. Plot scores for each PC
4. Fit parametric function to each score plot

The new parameterized regression model is then:

$$\hat{m}(x) = \exp \left(\mu + \sum_{i=1}^M p_i(x) z_i \right), \quad (4.3)$$

where μ is the mean regressed velocity field, $p_i(\cdot)$ is the i th polynomial function representing i th PC scores, z are PCs and M the number of PCs describing 99% of the variance.

Regression is done on 50 predictor values drawn from a normal distribution we obtained on the original data. This way we avoid conducting PCA on the original data and still get a reasonable representation of the original data structure.

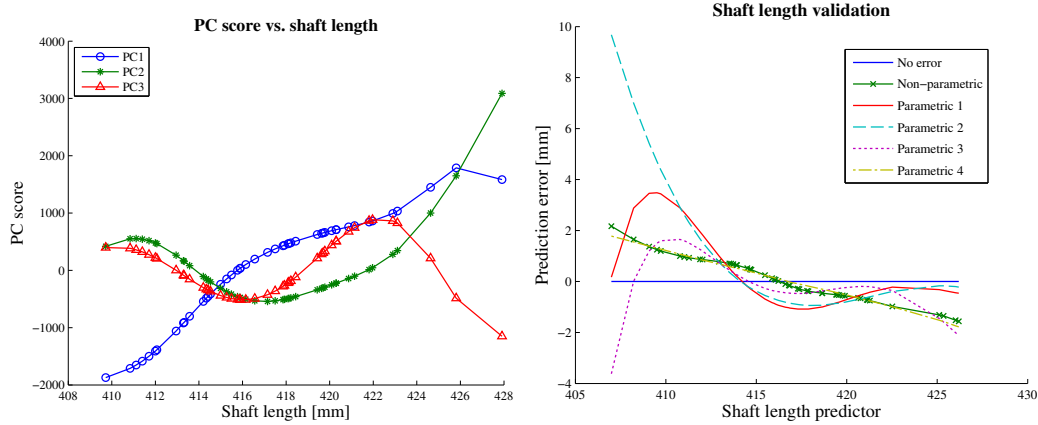


Figure 4.2: **Left:** Score values for the first three PCs. **Right:** Comparison of parametric and non-parametric regression results for shaft length.

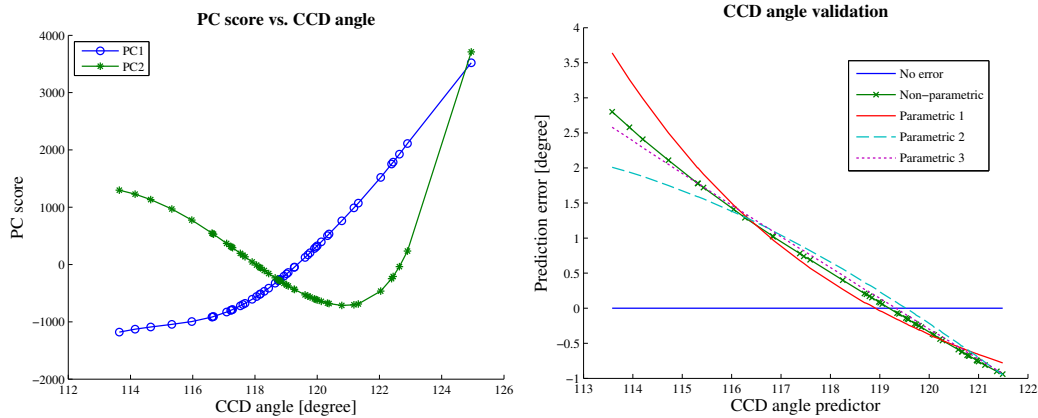


Figure 4.3: **Left:** Score values for the first two PCs. **Right:** Comparison of parametric and non-parametric regression results for CCD angle.

Results

Considering generalized cross-validation (GCV), $\Xi(u) = (1 - u)^{-2}$, as the penalty function in (4.2) we obtain 2.1 for shaft length and 1.6 for CCD angle. With these bandwidth values, prediction is performed on a dataset of 182 left femur CT images.

To validate the results, 50 velocity fields were predicted with prediction values drawn from the normal distribution of the original data. Then the exponential was taken of these fields and the shaft length and CCD angle were measured in the exponentiated fields.

Shaft Length Regression

To find the best parametric model, different polynomials were evaluated. Our evaluation showed that the best fit is linear for all PCs. In Fig. 4.2 the score plots

	PC1	PC2	PC3	RMS [mm]
Parametric 1	1	2	5	1.37
Parametric 2	1	2	3	2.26
Parametric 3	2	2	5	0.97
Parametric 4	1	1	1	0.83
Non-parametric	-	-	-	0.84

Table 4.5: Shaft length parametrization comparison. PCn columns show the order of the polynomial fit used for the corresponding PC.

	PC1	PC2	RMS [degrees]
Parametric 1	2	3	1.14
Parametric 2	1	2	0.88
Parametric 3	1	1	0.98
Non-parametric	-	-	1.00

Table 4.6: CCD parametrization comparison. PCn columns show the order of the polynomial fit used for the corresponding PC.

are depicted and in Tab. 4.5 four different parametrization and the root mean square (RMS) prediction error are listed. Parametric model 4 performs similar to the non-parametric model. In Fig. 4.2 the prediction values are compared in a more qualitative manner.

Caput Collum Diaphysis Angle Regression

Similar to the shaft length low order polynomial give better prediction results. The best prediction results are reached using a linear parametrization for the first PC and quadratic for the second (Tab. 4.6). This parametric model even outperforms the non-parametric model. See Fig. 4.3 for score and prediction error plot.

Discussion and Conclusions

Only three PCs for shaft length and two for CCD angle are needed to describe 99% of the variance in the velocity fields. This fact enables us to evaluate each predictor individually. Surprisingly, in both experiments low order polynomial parameterizations provided the best results. One possible reason for this could be the behavior of polynomials at the boundary data points. In both cases the parametric slightly outperforms the non-parametric model. It seems that the non-parametric model overfits on the training data. Therefore, we gain in three ways from parametric models: Simplicity of the model, computational efficiency and reduction of overfitting.

We plan to evaluate other parametric functions to avoid possible problems at boundary data points. The shown validation can only test the consistency of the

method, therefore we will further validate our method by comparing the prediction to manual segmentation results. In future work, simplicity and efficiency, will allow us to use univariate exploration methods to build multivariate regression models with two and more predictors.

4.3 Biomechanics of Femur Bones

Implant design manufacturers rely on limited amount of anatomical information to design femur implants. Furthermore, differences among subpopulations (stratum) within the overall population in terms of ethnicity, height, gender, etc. are usually not considered. This could partially be caused by the lack of large scale studies to understand the biomechanics of bones. Most studies have been conducted on low sample sizes [Keyak 1990, Schileo 2007] with some exceptions [Bryan 2009]. This might be due to the inaccessibility of large and public CT image datasets. Even with large datasets available, the manual effort that is required to conduct Finite Element (FE) analysis from CT images makes large scale analysis difficult. Two of the main problems are:

1. Creation of valid meshes without manual interventions
2. Automatic assignment of boundary conditions to anatomically corresponding areas

To tackle these problems, we proposed in [Bonaretti 2010] to use Statistical Appearance Models (SAMs) to conduct large-scale FE simulations. We analyzed biomechanical differences between 80 female and 57 male Caucasian subjects. Our proposed method is described in Fig. 4.4. The registration step that is needed to setup the SAM is preformed with the standard log-demons algorithm [Vercauteren 2009] after initializing with our method, as described in Section 2.6, with 2 levels and 4 regions. This femur specific polyaffine model is necessary to capture torsion and rotation in head and condyle regions of the femur bone. The SAM allows us to sample plausible bone instances from the PCA model and run FE analysis. To evaluate the stiffness of the femur bones, we applied a vertical load on the femoral head in the direction of the condyles while the condyles were fixed in all directions. The magnitude of the applied load was adjusted according to the weight of each subject.

In a second paper [Bonaretti 2011], we compared our volumetric registration-based SAM to a mesh registration pipeline on a dataset of 157 femur CT images. The evaluation of the FE mesh quality resulting from both approaches favored our method. The element quality was measured in terms of Jacobian, edge ratio and minimum angle on the mesh tetrahedrons.

In the future, it will be interesting to investigate if the element quality is linked to the number of modes used in the SAM. A long term goal consists of incorporating uncertainties in the FE method as discussed for instance in [Stefanou 2009]. In our case, these probabilistic FE methods could be extended by incorporating deformation statistics obtained from a cohort of images.

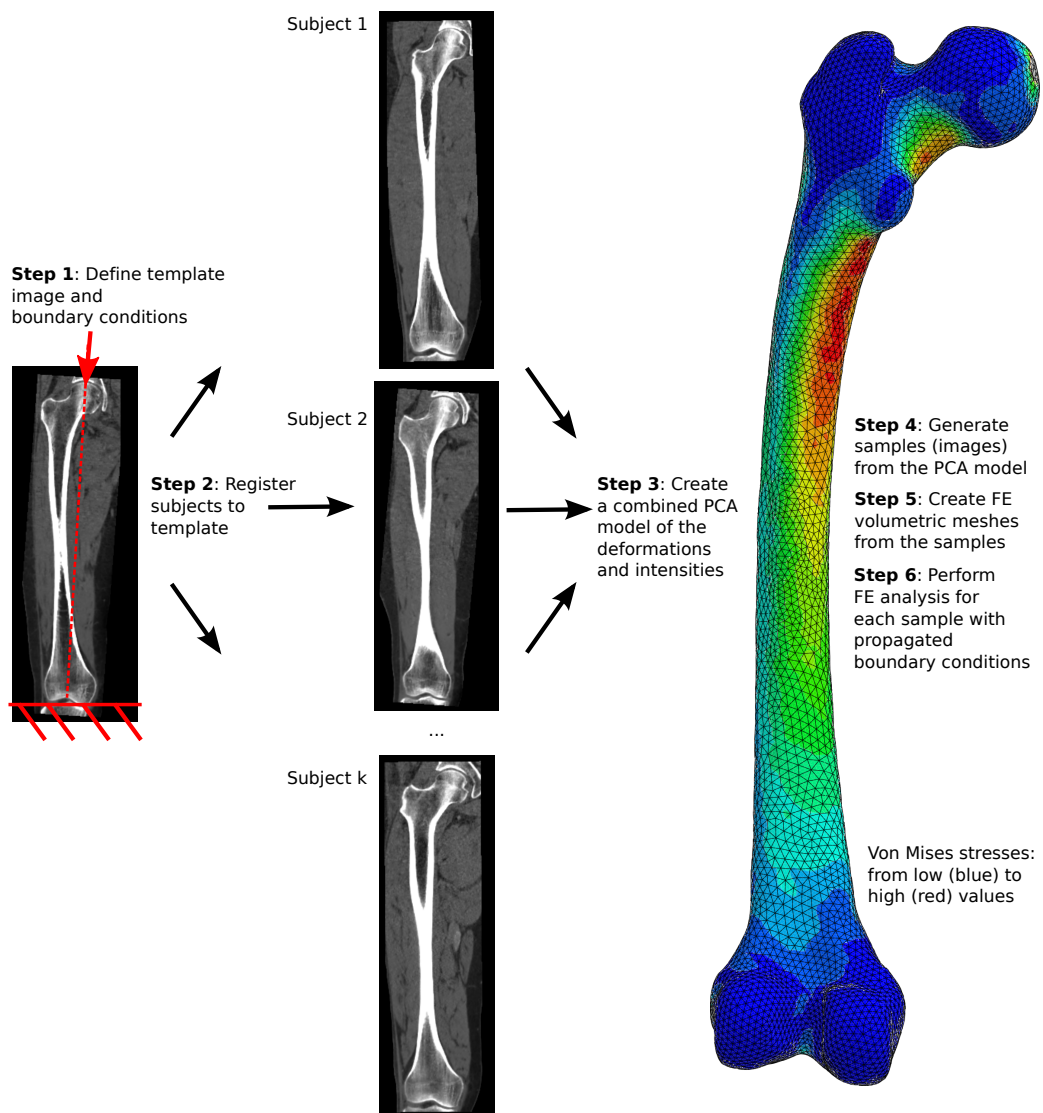


Figure 4.4: Dorsal view of the left femur bone. Shown is the pipeline that allows us to run FE simulations on a large cohort of images. In step 2, our registration method is used to initialize the log-demons. Boundary conditions are in red. On the right, the von Mises stresses computed with the FE simulation for one example bone are visualized.

4.4 Allograft Selection for Femur Bones

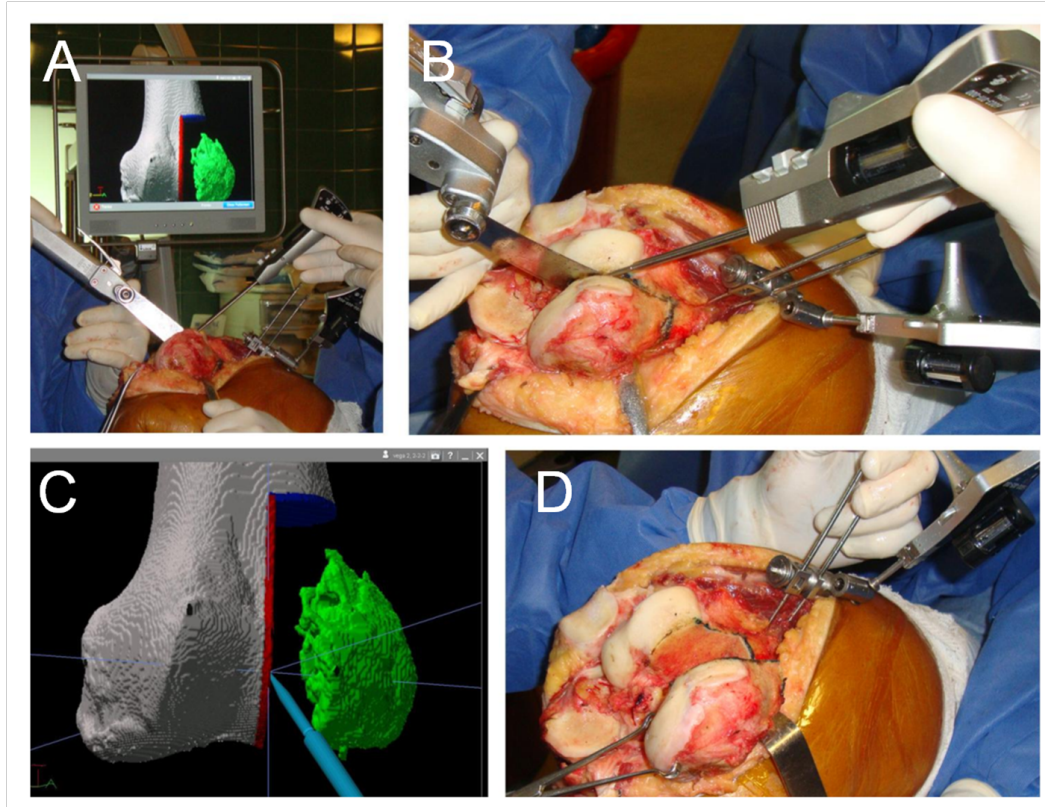


Figure 4.5: **A+C**: Three-dimensional preoperative planning. **B+D**: A multiplanar osteotomy. Image source: Lucas Ritacco, Department of Medical Informatics, Virtual Planning and Navigation Unit, Italian Hospital of Buenos Aires, Buenos Aires, Argentina.

Tumor excision is the primary treatment of aggressive or recurrent benign bone tumors and malignant bone sarcomas. This requires an invasive surgical intervention (Fig. 4.5) resulting in a residual bone defect that can be reconstructed with a fresh frozen bone allotransplantation. In orthopaedics, recent improvements in diagnostic and therapeutic techniques have produced an increase of patient survival as well as a reduction of the complication rate [Muscolo 2005]. It has been shown that the selection of bone allograft in terms of shape and size is crucial to prevent changes in joint mobility and load distribution, which can lead to joint fractures and early joint degeneration [Enneking 2001]. However, current selection approaches are very time-consuming, mostly based on manual measurements performed directly on the bones or on three-dimensional models reconstructed from images.

Ideally, an automatic allograft selection system could perform shape comparisons

between the patient’s anatomy and the complete bone bank. In this case, it would be necessary to allocate extra time to the clinical work flow in order to segment the patient’s anatomy and register it to the existing bone bank.

Practically, to avoid preprocessing, hence reducing preoperative planning time, the authors in [Ritacco 2010] proposed a simplified protocol for bone size characterization. The so-called ABC protocol is based on well-known anatomical landmarks, which can be extracted from the CT image and used in a selection criteria. The protocol defines 6 landmarks on the distal femur: Transepicondyle distance (A), anterior-posterior distance in the medial condyle (B) and in the lateral condyle (C). One possible automation of this protocol requires two steps. First, CT images of all donor bones are segmented and registered to a preselected reference. The ABC measurements can now be performed on the reference and correspondences in the other images can be extracted and stored. Second, the surgeon identifies manually the ABC landmarks on the patient CT image and uses the previously stored ABC measures to select the best match. Thus, the time consuming segmentation and registration step is performed only once, whereas for new patients only ABC landmarks are measured.

In order to automatize the procedure, we first tried to perform non-linear registration of the CT images using the log-demons approach [Vercauteren 2008]. However, we observed that the direct use of this method failed to capture torsion and rotation in head and condyle regions of the femur bone. To address this issue, we proposed in [Ritacco 2012] to model the expected deformations through a femur specific polyaffine model. We initialized the demons with a polyaffine registration of three regions (head, shaft and condyles) using block matching [Ourselin 2000] and regularized the subsequent iterations with a polyaffine model integrated into the log-demons algorithm as described in Section 2.6. As a last step, we relaxed the polyaffine constraint to allow more general local deformations regularized using a Gaussian smoothing.

The evaluation of the automatic ABC measurements showed a good agreement with manual measurements performed by two medical experts. The major advantage of the automatic method lies in its flexibility to extend the ABC protocol to include more or different measurements. A new protocol can be defined by simply selecting a different set of landmarks on the reference bone, the corresponding points are then available for the entire database at no additional costs. In terms of computation speed, the average time needed by a medical expert to perform the manual measurements was 16 hours, and 3 minutes for the automatic method. This clearly highlights the potential of the proposed automatic bone morphology tool for large databases.

4.5 Implant Shape Design for Mandible Bones

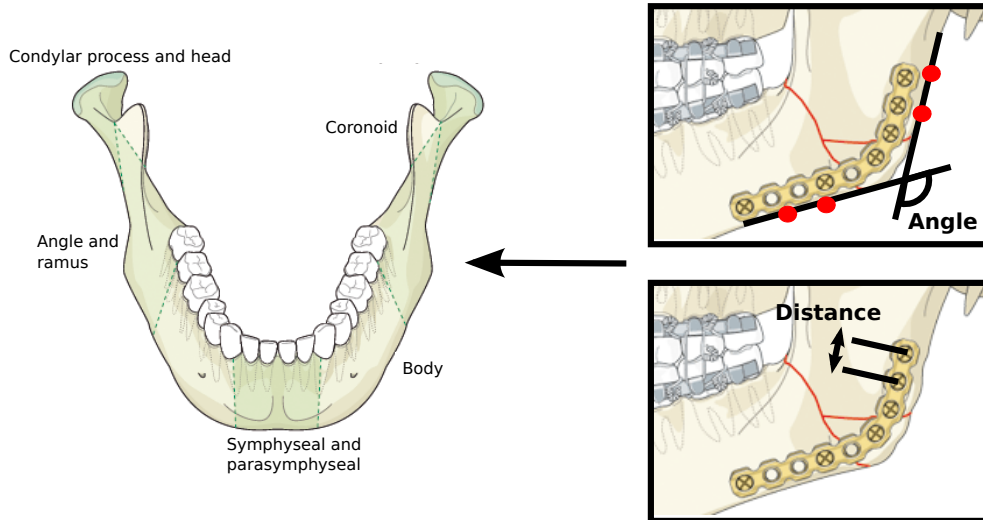


Figure 4.6: **Left:** Mandible with anatomical regions. **Top right:** The four red circles define the angle. **Bottom right:** The distance is measured between adjacent screw holes. Image source: www.aofoundation.org.

In [Bou-Sleiman 2012], we optimized the shape of implants considering intensity information in a cohort of 43 CT images. This population-based implant design approach extends recent works [Kozic 2010, Bou-Sleiman 2011] that focused on the surface of the bone. The interested reader can find a detailed motivation of population-based mandibular implant design in Chapter 2.

We optimized the distance between adjacent screws and the angle of the implant (as illustrated in 4.6) as a function of the thickness of the bone at the screw site and the maximum intensity values along the screws. The optimization in the two dimensional parameter space was done using an extensive search. To obtain correspondences between all 43 mandible CT images, we used the polyaffine transformation tree registration described in Section 2.7 with four levels.

Our optimal plate design was significantly different from a standard plate manufactured at Medartis AG, Basel, Switzerland. To test whether this change in the shape of the implant affects the biomechanical stability, we plan to preform FE analysis in the future.

4.6 Prediction of Bone Surface for Orthopaedic Research

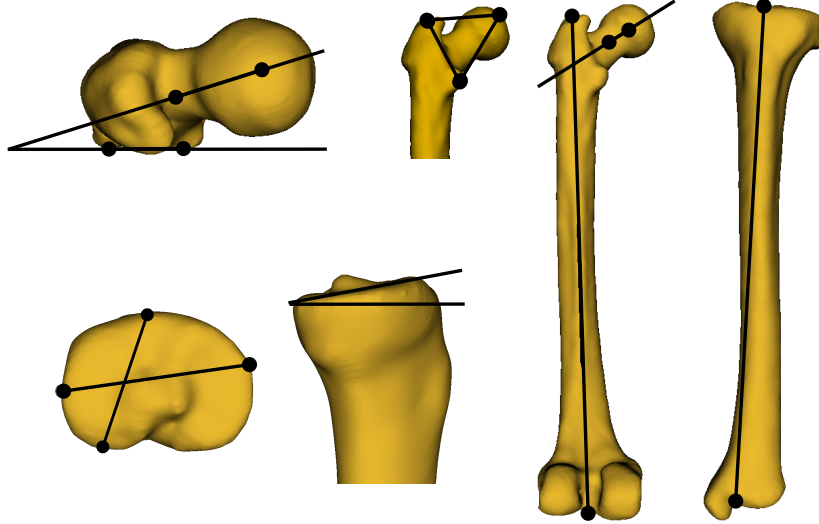


Figure 4.7: Distance and angle based predictors for femur and tibia. **Top left:** Femoral head. **Bottom left:** Tibial plateau. **Right:** Dorsal view of femur and frontal view of tibia.

In [Blanc 2012], we investigated the benefits of considering patient metadata and morphometric measures to enhance bone surface shape prediction. Our investigation compared four regression methods: partial least square regression, principal component regression, canonical correlation analysis, and non-parametric kernel-based regression. These methods are compared for different anatomical sites of interest in orthopaedic research including femur and tibia. Clinically relevant covariates were selected, and the effect of different combinations of covariates on the prediction accuracy was investigated on a database of 142 femurs and 154 tibias.

Along with CT images we collected anthropometric, demographic and morphological covariates for each subject. The covariates that we included in the study are the following:

- Anthropometric: Height and weight
- Demographic: Age
- Morphological: Bone angles and distances, measured on the reference bone surface, as shown in Fig. 4.7
- Point clouds: To simulate predictors from ultrasound imaging used in computer-assisted surgery tasks we selected patches of vertices on the surface of the reference bone. The coordinates of all vertices are used as predictors.

The response variables of the regression problem were three-dimensional bone surfaces. The correspondences between surfaces was established by using a preliminary version of the registration method presented in Section 2.6.

We found that additional height and weight information of the patient improves prediction accuracy. Therefore, we recommended that researchers constructing and utilizing statistical shape models, systematically collect such meta-information in addition to the image. Furthermore, such additional patient information could be incorporated at the group level in the prior presented in Chapter 3.

4.7 Heart Modeling with Incompressibility Constraints

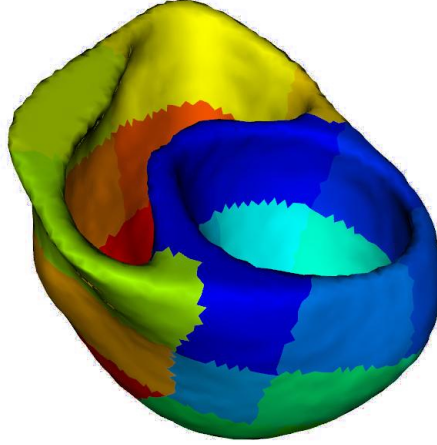


Figure 4.8: The heart divided into 17 anatomical regions defined by the American Heart Association.

In [Cerqueira 2002], the American Heart Association (AHA) introduced a standardized myocardial segmentation of the heart into 17 regions. Each region has different tissue properties and anatomical functionality. An example geometry of the heart with labeled regions is shown in Fig. 4.8.

To help clinicians study heart defects and improve diagnostic and therapeutical procedures, the motion of the heart is tracked over time using 3D cine MRI sequences. The analysis is performed on the change per regions over time on a cohort of images. The tracking is done using registration algorithms. In [McLeod 2012], we propose a new kind of registration to tackle this task. The registration builds on the polyaffine transformation tree approach presented in this thesis. Additionally, we introduce new constraints that are in accordance with clinical evidence.

It was reported in [Glass 1991] that during the cardiac cycle the heart muscle changes its volume approximately 5%. We incorporated this clinical prior knowledge as a penalty term on the determinants of the log affine transformation parameter. To further regularize the results we assume that neighboring regions have similar transformation parameter and we introduce a second constraint penalizing a Log-Euclidean distance between adjacent regions.

We obtained results on a dataset of 10 healthy volunteers on the left ventricle. The volume change on average is within an approximate 20% range. To achieve the ideal 5% of volume change during a cycle we plan to increase the number of regions by further subdividing the anatomical regions. This subdivision could be guided by the data-driven approach that we employed for femur and mandible bones as presented in Chapter 2.

Conclusion and Perspectives

In this chapter, we make an overall conclusion of this Ph.D. thesis and give our perspective on interesting open questions. We believe the work on statistics of trees in the context of Phylogenetic Trees has the potential to provide interesting insights in polyaffine transformation trees. We give a short introduction to this topic in Appendix A.

Contents

5.1	Conclusion	88
5.2	Short Term Perspectives	89
5.2.1	Validation on 100'000 Landmarks in 400 Spine CT's	89
5.2.2	More Structures: Spine, Whole Body Scans, Brain	90
5.2.3	Regions Derived from Atlases	92
5.2.4	Multivariate Regression on Geometrical Deformations	92
5.3	Long Term Perspectives	92
5.3.1	Probabilistic FEM Parameterized with PTTs	93
5.3.2	Empirical Bayes Method to Optimize Hyperparameter	93
5.3.3	Sparse Anatomical Relations at the Group Level	93
5.3.4	Hyperpriors for Polyaffine Parameter	93
5.3.5	Applied Topology to Analyze Tree Deformations	94
5.3.6	A Prior Distribution of Weight Trees	94
5.3.7	Image Registration by MCMC Simulations	96
5.3.8	Angiogenesis of Heart Muscle Fibers	96

5.1 Conclusion

In medical image analysis, geometrical deformations are used to model intersubject variability. In orthopaedic applications, the geometrical variability is usually observable across anatomical scales. For instance, anatomical differences between mandible bones of different patients can be found on a coarse scale, between the entire left or right side, or on a fine scale, between teeth. Each level of granularity has specific regions of interest in clinical applications. The challenge is to connect the geometrical deformations to clinical regions across scales. In this manuscript, we introduced a tree-based structuring of geometrical deformations that is able to capture shape variability across scales and is intelligible for clinicians. We then formulated a statistical estimation of the transformation parameter which allowed us to incorporate deformation statistics as a prior. The improved intelligibility for clinicians and accuracy makes our method a good candidate for clinical use.

In Chapter 2, we introduced a novel way to capture anatomical variability with polyaffine transformation trees in a mathematical rigorous framework and computational efficient optimization. We showed two applications where this new description of the anatomy is helpful. In allograft selection for tumoral femur bone replacement, on a dataset of 146 CT images, the results showed an improved accuracy of the registration with a much smaller set of parameters with respect to standard methods. In the implant design application, we illustrated, on a dataset of 42 mandible CT images, that our method is able to capture the anatomical differences across scales. Furthermore, we illustrated how the new registration can be linked to known anatomical regions. Finally, the clustering of selected regions highlighted the intelligibility of our new approach in medical applications.

In Chapter 3, we formulated the estimation of polyaffine transformation trees in a Bayesian framework. The Bayesian interoperation of our registration method allowed us to optimize all scales simultaneously as opposed to the traditional coarse to fine optimization scheme. We introduced a General Linear Model (GLM) for multiscale intersubject deformations and we gave an interpretation of our assumption to neglect the off-block diagonal elements of the concentration matrix in terms of conditional independence of regions. To our best knowledge, this is the first attempt towards the incorporation of deformation statistics at the group level for polyaffine registration. The results indicate that incorporating deformation statistics increases registration accuracy (in terms of Dice coefficient and contour mean distance on the manually segmented bone mask) and robustness (in terms of determinant, rotation and translation part of the polyaffine parameter).

In Chapter 4, we presented seven different clinical applications of our work carried out in the context of five collaborations. In addition to applications in orthopedics (symmetric assessment of tibias and femurs, regression of deformations from landmarks distances and angles for femur bones, biomechanics of femurs, allograft selection for femurs, implant design for mandibles, prediction models for orthopaedic research), we pointed out that our methods can be translated to other fields (heart modeling). Even though, the presented clinical applications have yet

to fully take advantage of the intelligibility of our method, they benefit from the improved registration accuracy (as shown in Chapter 2).

Overall, we conclude that the next steps towards an intelligible description of the anatomy is to fully take advantage of the tree structure. As of now, we consider the multiscale structure by optimizing the entire tree simultaneously, considering implicitly the connection of parent nodes (i.e. regions) and child nodes through the weight of each node.

In this manuscript, we made two main assumptions:

1. Topology of the weight tree is the same for all patients (with varying transformation parameters)
2. The estimated polyaffine parameter do not influence the weight tree topology

To relax the two assumptions we consider works on statistics of trees (e.g. Phylogenetic Trees) or applied topology. A short introduction in Phylogenetic Trees is given in Appendix A. Some ideas on how to combine Phylogenetic Trees and our trees are given in the long term perspectives (Section 5.3.6).

5.2 Short Term Perspectives

During the course of writing this Ph.D. thesis many questions have been raised and not all of them have been addressed. Here is a list of short term perspectives of same of these questions.

5.2.1 Validation on 100'000 Landmarks in 400 Spine CT's

In Chapter 2, the validation of our method was performed on 146 femur bones using manual measurements from two medical experts (one medical expert performed the measurements twice to yield intra-rater errors). This validation was task specific for allograft selection based on the same measurements. For the mandible bones, we did not have such a task-oriented validation available. According to [Rohlfing 2012], a reliable accuracy test would involve segmenting all 42 images into anatomical regions and testing of the overlap of each region. As a first step, the accuracy test was done on one region representing the entire bone. The segmentations were performed manually and the accuracy was tested in terms of overlap score and mean contour distance.

For the next step of evaluation, we plant to use a unique dataset from the anatomist Nicolas Bronsard at the Centre Hospitalier Universitaire de Nice, France. In [Bronsard 2012], Nicolas Bronsard measured 100'000 landmarks in 400 spine CT images. The measurements include 27 landmarks on L1, 50 landmarks on L2-L5 and 23 landmarks on S1 (illustrations of a subset of landmarks are shown in Fig. 5.1). We plan to validate our method and explore anatomical questions in collaboration with Nicolas Bronsard and his impressive dataset.

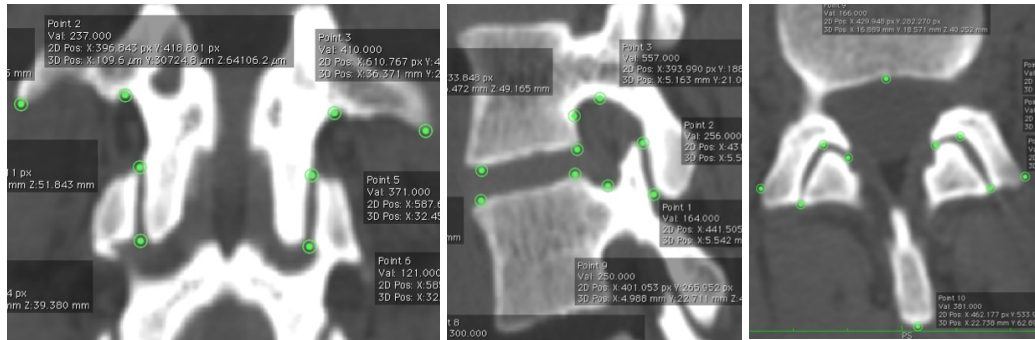


Figure 5.1: Landmarks measurements (green circles) on lumbar spine L1 and L2. **Left:** Coronal plane. **Middle:** Sagittal plane. **Right:** Transverse plane. Image source: Nicolas Bronsard, Centre Hospitalier Universitaire de Nice, France.

5.2.2 More Structures: Spine, Whole Body Scans, Brain

The methods described in this manuscript are not specific to any anatomical structure. We conducted preliminary experiments on spine CT images and brain MRI. As a first step, we propose to create weights enclosing all five vertebra for an initial affine alignment with a subdivision into vertebrae L1-L5 (Fig. 5.2). Further subdivision per vertebra are possible either via our data-driven approach or by including anatomical prior knowledge from the anatomist.

In the brain dataset LPBA40 from LONI, we explored data-driven regions as depicted in Fig. 5.3. As anticipated, we obtained a splitting (at level 2) into the two hemispheres. The data-driven definition of weights was computed from structure tensors [Clatz 2005, Taquet 2011] instead of the gradient image as presented in Chapter 2. Despite the fact that the weights can be anatomical justified, the obtained transformations were not conclusive. At this point, we conjecture that the regions are not homogenous enough to provide a consistent estimation of transformations. We plan to investigate other ways to obtain more homogenous regions, for instance, a good candidate could be the recently introduced regional flux analysis of longitudinal atrophy in Alzheimer’s disease [Lorenzi 2012].

Another interesting field application are whole body scans. Whole body scans clearly need a global initialization of major structures prior to any kind of analysis. Since our approach is based on polyaffine transformations, which were initially designed to handle articulated structures, we believe that our method could be a good candidate. Another important requirement for whole body scans is the need for efficient algorithms to handle the large datasets. Our method is driven by the log-demons algorithm, which is known for its efficiency, indicating that it could be helpful for large images.

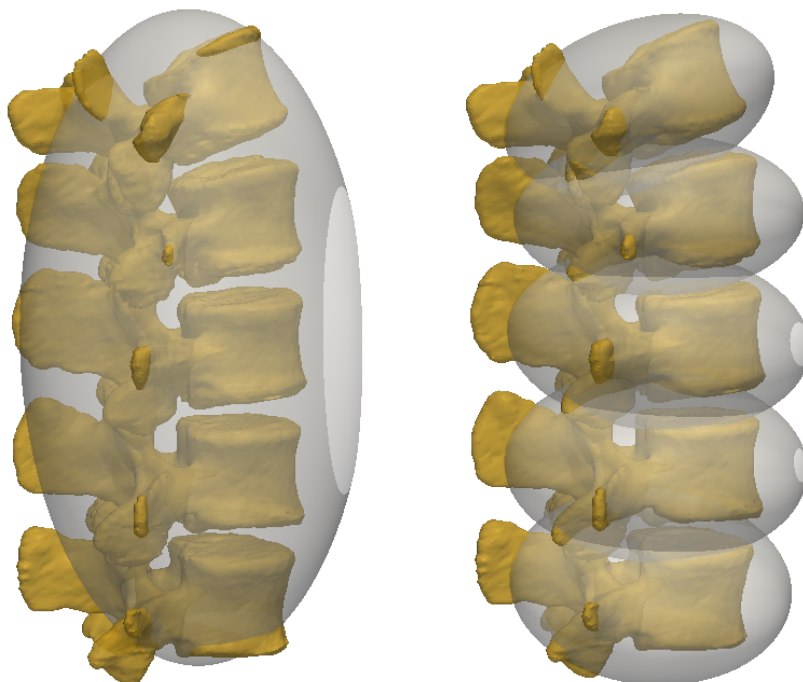


Figure 5.2: An example surface with weight regions superimposed. The weights were computed using the data-driven approach presented in Chapter 2. Each Gaussian weight represents one region and is visualized as one ellipsoids thresholded at σ . The surfaces were extract from one of the spine CT images from Nicolas Bronsard at the Centre Hospitalier Universitaire de Nice, France.

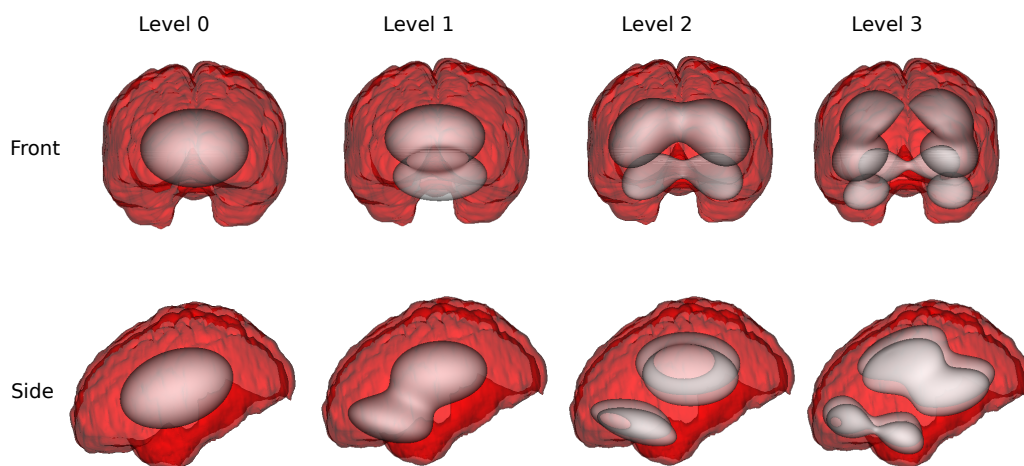


Figure 5.3: Four levels of regions derived from structure tensors using the data-driven approach introduced in Chapter 2. Each Gaussian weight represents one region and is visualized as one ellipsoid at σ . Brain MRI from the LONI LPBA40 dataset.

5.2.3 Regions Derived from Atlases

The current ITK implementation (Appendix C) can handle manually defined and data-driven regions. In case of manually defined regions, the user needs to add an additional argument specifying a label image. Each integer label is read as one region and converted to a Gaussian weight. This allows us to run further experiments using atlases.

5.2.4 Multivariate Regression on Geometrical Deformations

In [Blanc 2009], we presented conditional shape models for bone surfaces extracted from 170 femur CT images. We conditioned the surface shape distribution with patient metadata (age, height, and weight) and morphometric information (femur length, inter-condyle distance, neck length, vertical head diameter, collo-diaphysal angle, and anteversion angle). The results highlighted the more compact model that can be attained by conditioning the space of plausible shapes, making the proposed method suitable to create personalized shape models. The extension of this approach to shape models of bone mineral density is not straightforward due to the large number of variables (voxels) present in medical images. We stated that the regression problem becomes computationally challenging unless dimensionality reduction techniques are employed or a low-dimensional parameterization of the geometrical deformation is used. A solution was presented in [Rohlfing 2009] introducing a generalized multi-linear regression for appearance atlases and illustrated on brain MR images of 36 subjects. The authors solve one regression model for each voxel independently.

The introduction of our new parameterization of diffeomorphisms with polyaffine transformation trees opens an alternative way. In the light of our registration with groupwise deformation statistics as a prior (Chapter 3), we are now able to adapt [Blanc 2009] for appearance regression. The main idea is to use the estimated covariance matrix (inverse of the concentration matrix) and the sample mean as the parameters of a normal distribution. This normal distribution can now be conditioned along the lines of [Blanc 2009]. Synergies with the developments on Bayesian estimation of transformation parameters described in Section 5.3.2 and 5.3.4 are anticipated, since these approaches also try to estimate the mean and concentration matrix of transformations.

5.3 Long Term Perspectives

Long term perspectives on questions that have been raised during the course of this Ph.D. are addressed here.

5.3.1 Probabilistic FEM Parameterized with Polyaffine Transformation Trees

Building on our work in biomechanics with Statistical Appearance Models (Section 4.3), a long term goal consists of incorporating uncertainties in the Finite Element Method (FEM) as discussed for instance in [Stefanou 2009]. In our case, these probabilistic FEM approaches could be extended by incorporating deformation statistics obtained from a cohort of images. The mesh geometry could be modeled not as one instance but as a distribution.

To enable this kind of computationally intense analysis, the polyaffine basis could be a possible candidate to replace meshes. Efforts in isogeometric analysis [Hughes 2005, Vuong 2010], where the meshes are parametrized with spline functions, could be considered to use polyaffine transformation trees as the basis instead of splines.

5.3.2 Empirical Bayes Method to Optimize Hyperparameter

Building on the Bayesian formulation of our registration method from Chapter 3, we could optimize the hyperparameter Γ of the normal prior with the Empirical Bayes Method. The method was introduced in [MacKay 1992] and recently extended to favor sparse hyperparameter [Tipping 2001, Wipf 2011]. In [Zhang 2011], the authors introduced extensions for hyperparameter in the form of block diagonal matrices. However, it is unclear how off-block diagonal elements of the hyperparameter can be included in the optimization.

In [Sabuncu 2011], the authors used the Empirical Bayes Method to predict the age of brain MR images by learning a sparse set of spatial predictors. The predictors are voxel-wise measurements of gray matter density values obtained through the Jacobian of the non-linear deformations.

5.3.3 Sparse Anatomical Relations at the Group Level

If we made an additional assumption that regions are only sparsely related to each other, we could replace the block diagonal sample covariance matrix inversion from Chapter 3 with the Graphical Lasso [Friedman 2008, Banerjee 2008]. Extensions to structured matrices using the Kronecker product [Werner 2008, Tsiligkaridis 2012] might be worth to explore.

In the case of mandibles, this kind of sparse relations between regions are largely unexplored in the clinical setting and thus do not provide any way to validate new results. Therefore, articulated structures, where the structural relations are known, would be a better starting point.

5.3.4 Hyperpriors for Polyaffine Parameter

As shown in Chapter 3, the block structure of the covariance matrix has an interpretation in terms of the anatomy. Each 12×12 diagonal block represents one

region, the off-diagonal blocks represent the covariance between two regions. Furthermore, the inverse of the covariance matrix gives us conditional independences between regions, which indicates anatomical relations between parts of the anatomy. In Chapter 3, we limited our concentration matrix to be blockdiagonal, removing all relations between regions. We plan to work on an extension to include the off-diagonal blocks in the concentration matrix as well. The long term objective is to consider the prior mean μ and the prior concentration Γ not as fixed parameters but as hyperpriors following their own distributions.

In Bayesian statistics, hyperpriors represent prior distributions on hyperparameters, which are the parameters of the prior distribution. A possible choice of hyperpriors can be found in [Wang 2009, Wang 2012]. With the inclusion of hyperpriors, we will need to move from the analytical closed form solutions to the posterior computation using Markov Chain Monte Carlo methods.

5.3.5 Applied Topology to Analyze Tree Deformations

One of the ideas of applied topology is to use topology to understand the geometry of the underlying space of a dataset qualitatively, e.g. connectedness or the number of holes of that space, before doing computer-intense quantitative analysis. In the context of Big Data, applied topology already found its application to detect the structure of the data with possible subsequent geometrical statistical analysis (for instance [Bubenik 2010]). In the field of network engineering, one application of topology is to take a collection of local data and try to patch it together to obtain an understanding of the global landscape. On the theoretical side, the Mayer-Vietoris principle provides a deep idea from homology to describe the transition from local to global data. In the field of biology, during the workshop on “Statistics, Geometry, and Combinatorics on Stratified Spaces Arising from Biological Problems” at MBI¹, presentations were given covering the current state in this field. Topics of the presentations ranged from general surveys of stratified spaces, the geometry and statistics of geometric trees, and statistical topology.

The connection to polyaffine transformations lays in the fact that we describe deformations in a local region and combine everything to a global diffeomorphisms. Future research could address questions on how applied topology could be used to learn the structural relations between parts of the anatomy.

5.3.6 A Prior Distribution of Weight Trees

In this manuscript, we considered the weights of the image regions to be fixed during the registration. We estimated the weights from image features before the estimation of polyaffine parameter through a generalization of the Oriented Bounding Boxes Tree algorithm [Gottschalk 1996]. We believe that this is a good starting point for the registration, but not the optimal configuration of weights. Another limitation of

¹Mathematical Biosciences Institute at the Ohio State University, OH, USA

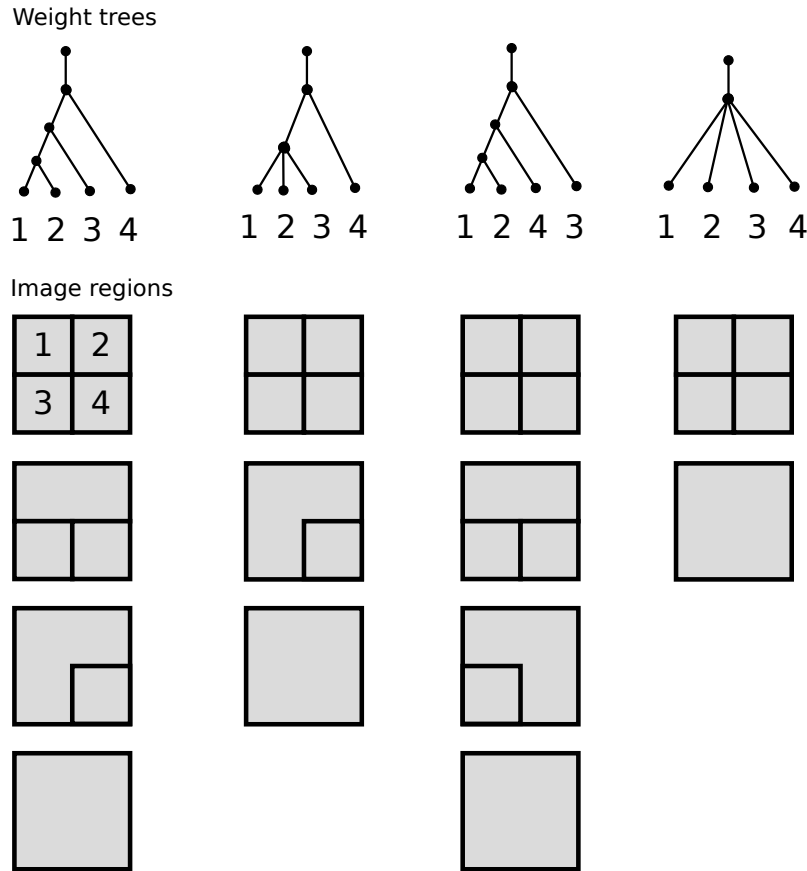


Figure 5.4: Labeled weight trees and corresponding image regions.

the current work is the weight definition on the template rather than the entire cohort of images. Furthermore, the Gaussian weights could be adopted to other types of functions as long as they are smooth so that all requirements for diffeomorphic deformations from SVFs are satisfied.

Instead of computing a deterministic configuration of weights prior to the registration, we could create a distribution of possible weight configurations and include it in our Bayesian formulation (Chapter 3) as an additional prior. The distribution of weight trees could be inspired by statistics for Phylogenetic Trees. However, this will lead to non-analytic solutions, and force us to use Monte Carlo methods to compute the posterior distribution of polyaffine parameter.

An introduction to Phylogenetic Trees and trees space can be found in Appendix A. Figure 5.4, shows a possible connection between labeled tree combinatorics as used in phylogenetic analysis and our image regions. Each column represents a different tree topology. The question here is, what is the best combination of regions across different levels with four fixed leaf node regions.

5.3.7 Image Registration by MCMC Simulations

In the very long term, we envision an image registration that does not rely on registration algorithms like the log-demons but is formulated entirely within a statistical framework. We plan a generative model with prior distributions on the weight tree and the polyaffine parameter. For the polyaffine parameter distribution, we can make reasonable assumptions, for instance we expect a volume change of 0.5 to 2 with respect to the template for all regions. On the other hand, the distribution of the weight tree is an even more challenging problem.

The new statistical registration algorithm will be based on MCMC simulations. We could sample from the posterior distribution of polyaffine parameter, generate SVFs and compute performance scores to guide the random walk of the simulation. These performance scores could be manually measured landmarks or Dice coefficients from segmentations.

We think this kind of simulation is now possible because we introduced a generative linear model of geometrical deformations. This could open up many new avenues, where image registration is not concerned with finding the best possible image metric to be optimized but with finding the smartest way of sampling from the posterior distribution.

Interesting works on finite element based Bayesian image registration was recently introduced in [Risholm 2011, Janoos 2012a, Janoos 2012b]. The authors sample from the posterior distribution of deformation parameter and provide uncertainty quantifications for parameter, which is important in many clinical applications.

5.3.8 Angiogenesis of Heart Muscle Fibers

Angiogenesis is the physiological process of formation and splitting of blood-vessels. In the context of cancer and cardiovascular research, angiogenesis is studied both as a diagnostic and therapeutical tool. As seen in Fig. 5.5, a scanning electron microscopy image of heart muscle fibers reveals a tree-like branching structure of the fibers. In the clinical context, it is hypothesized that different branching structure exist for patient with cardiovascular diseases with respect to the control group. Therefore, there is a need to perform quantitative analysis on this kind of images. One interesting question in this setting would be the classification of unhealthy versus control patients based on the branching structure of the vessel tree [Metzen 2009, Aydin 2009, Lo 2010, Owen 2011, Feragen 2011, Aydin 2012]. These kind of questions could be addressed with more advanced polyaffine transformation trees.

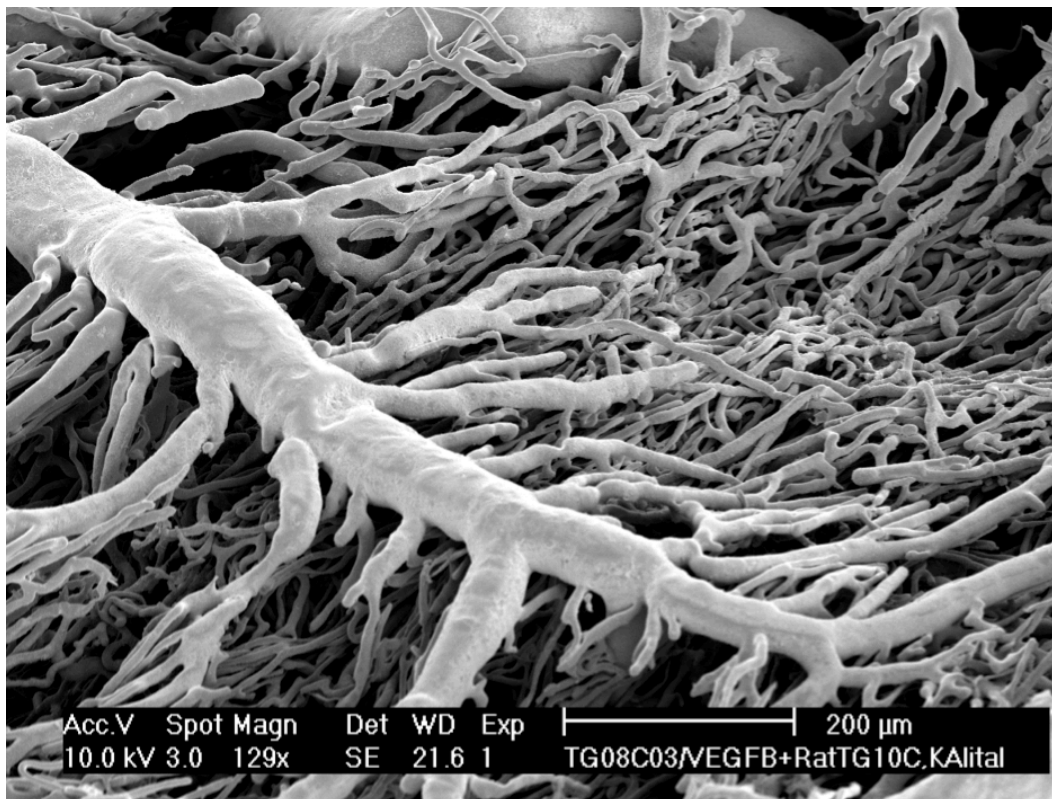


Figure 5.5: Scanning electron microscopy image of heart muscle fibers. Image source: Institute of Anatomy, University of Bern.

Appendix: Phylogenetic Trees

The work in statistics on Phylogenetic Trees is outlined here to highlight possible synergies between polyaffine transformation trees and phylogenetics.

A.1 What are Phylogenetic Trees?

Phylogenetic Trees describe the evolutionary process of species. The tree has a root node, the origin of the species, from which child nodes represent species that descent form the origin. Each child node can then itself become the parent of another subspecies. A recent example of a Phylogenetic Trees is shown in Figure A.1. It is a very detailed tree of life estimated using DNA sequence data as of 2006 and published in [Ciccarelli 2006]. DNA sequences obtained from different genes across species are aligned prior to the tree-based statistical analysis. The alignment can be done with known orthologs, paralogs or xenologs genes. The estimation of the tree can be done with many different methods, ranging from parametric to non-parametric.

A.2 Geometry of Phylogenetic Tree Space

Let's define an n -tree as a acyclic graph with n leaf nodes and one root node. The root node has index 0 and the leaf nodes are indexed from 1 to n . A metric n -tree is an n -tree with all inner edges having length greater than 0. A binary 4-trees has 15 quadrants (or 2-dimensional orthant) according to $(2n - 3)!! = (2n - 3) \cdot (2n - 5) \cdots 5 \cdot 3 \cdot 1$, which are glued together along their common faces. For more details of enumerating labeled trees we refer the reader to [Stanley 2001]. A subspace of the 4-tree space with three quadrants is show in Figure A.2. An illustration of the full tree space with all 15 quadrants is shown in [Billera 2001].

Tree rotations are one way to measure the distance between two trees. A tree rotation shrinks an inner edge to 0, then expands the resulting vertex of degree 4 into a new inner edge and two new vertices of degree 3. The degree of a vertex is measured by counting the number of edges connected to it. In Figure A.3, an example rotation is shown for a 4-tree.

The metric of this space of trees is a sum of Euclidean distances for each quadrant between two points. A geodesic in this space is the path that describes the minimum sum of Euclidean distances between two points. As shown in [Billera 2001], the tree space has non-positive curvature. This property of the space provides uniqueness

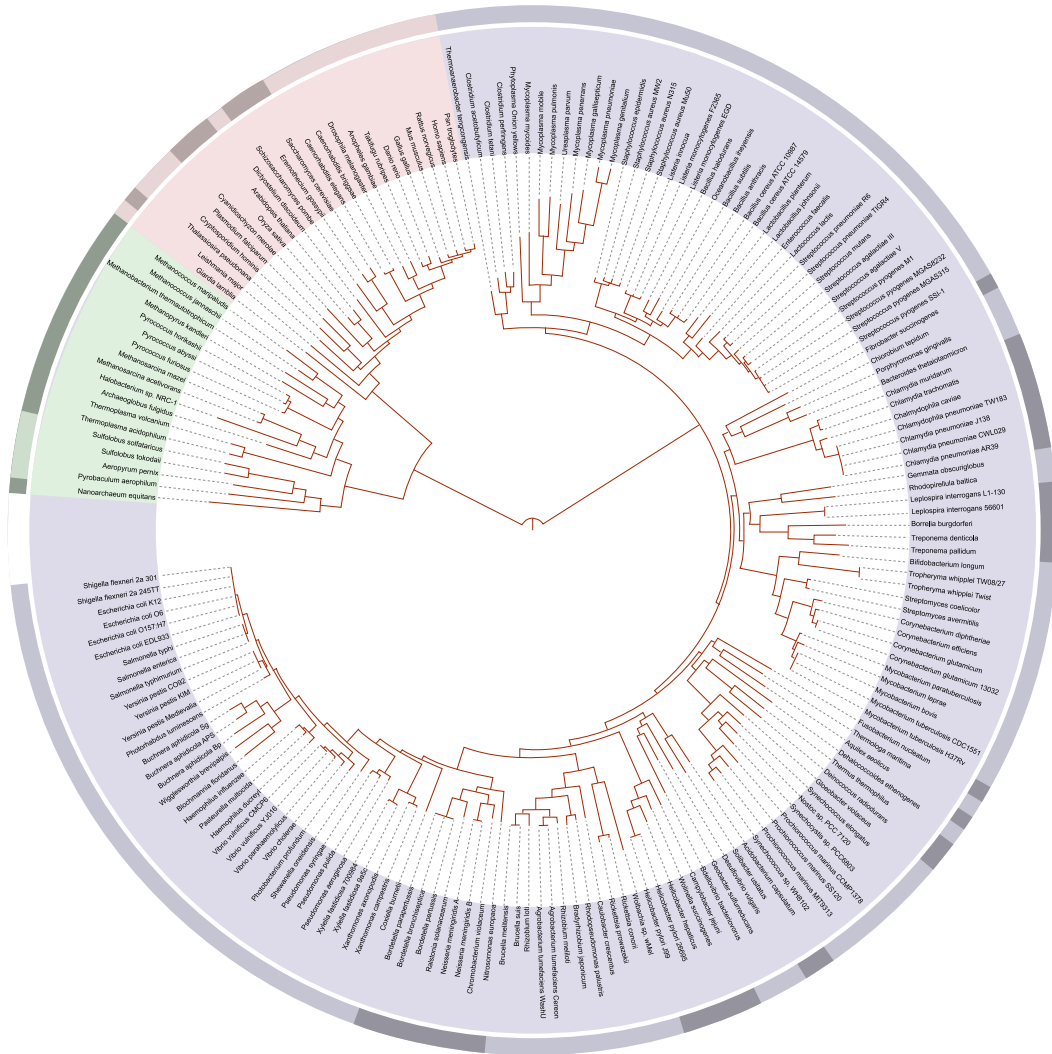


Figure A.1: Shown is a phylogenetic tree of relationships between species whose genomes had been sequenced until 2006. The last universal ancestor of all life on earth is represented as the root node. The color code visualizes the three domains of life: pink represents eukaryota (animals, plants and fungi), blue represents bacteria, and green represents archaea. The Homo sapiens can be found second from the rightmost edge of the pink segment. Image source: [Ciccarelli 2006]

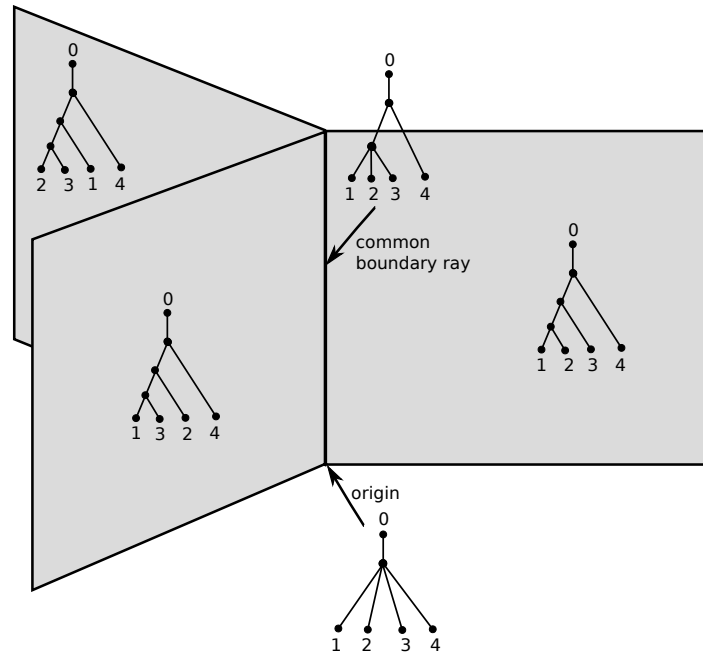


Figure A.2: A subspace of the 4-tree space showing the origin, where all trees come together, and an edge representing the common boundary ray shared between three different 4-trees. The three quadrants are an idealization, in theory they would go to infinity in two directions. Every point on the quadrants represents one 4-tree. To change the inner edges of the tree we move to a different quadrant. The common boundary ray is a 4-tree with only one edge. At the origin we have no inner edges.

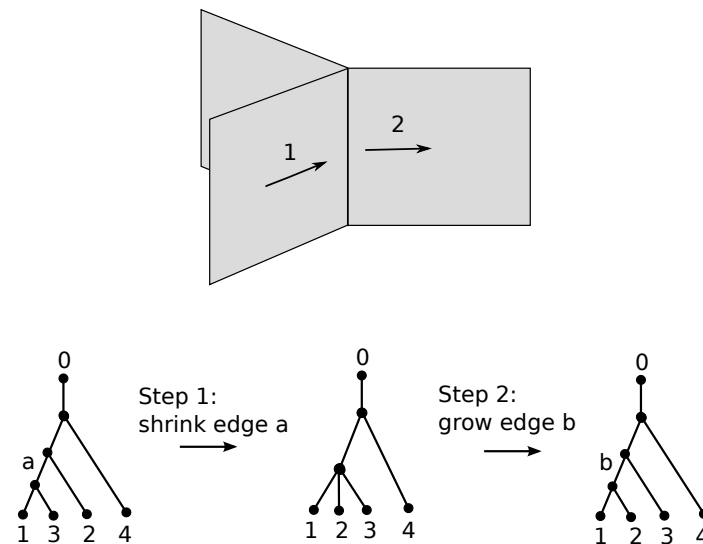


Figure A.3: A rotation from one tree configuration of inner edges to another through an intermediate change of the number of inner edges.

of geodesic paths, and existence and uniqueness of various type of centroids. This allows us to do statistics in the space of trees.

Appendix: Directional Derivative of Matrices

We use the method of directional derivatives to derive C w.r.t. M in the direction of W in Section 2.2.3. When the directional derivative is zero we have the minimal solution (in a least square sense) for M .

We present three definitions and properties that we later use for the method. First, we use the following definitions for directional derivative:

$$\begin{aligned} \partial_W C(M) &= \frac{\lim_{\varepsilon \rightarrow 0} (C(M + \varepsilon W) - C(M))}{\varepsilon} \iff \\ C(M + \varepsilon W) &= C(M) + \varepsilon \partial_W C(M) + \mathcal{O}(\varepsilon^2). \end{aligned}$$

Second, we use the Frobenius inner product to write,

$$\partial_W C(M) = \left\langle W, \frac{\partial C(M)}{\partial M} \right\rangle = \text{Trace} \left(W^T \frac{\partial C(M)}{\partial M} \right).$$

Third, we use the following properties of the trace,

$$\begin{aligned} \text{Trace}(W(\nabla C)) &= \text{Trace}((\nabla C)W) = \text{Trace}(W^T(\nabla C)^T), \\ \text{Trace}(W + (\nabla C)) &= \text{Trace}(W) + \text{Trace}(\nabla C). \end{aligned}$$

Now, the method is to compute the Taylor expansion of $C(M + \varepsilon W)$, then we take the non- W part of the first order term and by using the properties of the trace, we rewrite it as,

$$\partial_W C(M) = \text{Trace}(W^T(\nabla C)), \tag{B.1}$$

now by identification, we have,

$$\frac{\partial C(M)}{\partial M} = \nabla C.$$

Appendix: Implementation in ITK

The majority of the code is written with ITK filters. For the visualization the VTK framework is used. An open source copy of the code can be found on github:

- [git://github.com/ChristofSeiler/PolyaffineTransformationTrees.git](https://github.com/ChristofSeiler/PolyaffineTransformationTrees.git)

To build binaries from the source it is required to install the latest ITK version¹. After successful installation of ITK the following commands need to be execute on the terminal:

```
> git clone
  git://github.com/ChristofSeiler/PolyaffineTransformationTrees.git
  MyPolyaffineTransformationTrees
> cd MyPolyaffineTransformationTrees
> cmake .
> make
```

In the “cmake .” step it might be necessary to define the path to the ITK build folder.

C.1 Extending the Log-Demons Code

The code is based on the log-demons described in [Vercauteren 2009]. This code is freely available on the insight journal website². The main changes that we made are isolated to one method in one class,

```
itk::PolyaffineLogDomainDeformableRegistrationFilter::
SmoothGivenField(VelocityFieldType * field,
                 const double StandardDeviations[ImageDimension])
```

This function is called to regularize the estimated SVF after every iteration of the log-demons algorithm. We overwrite this method to estimate the polyaffine transformation tree. The first argument is the unregularized SVF. The second argument is the amount of smoothing applied in the standard Gaussian smoothing step. In our implementation the second arguments is not used.

¹At the time of writing ITK 4.1.0

²<http://www.insight-journal.org/>

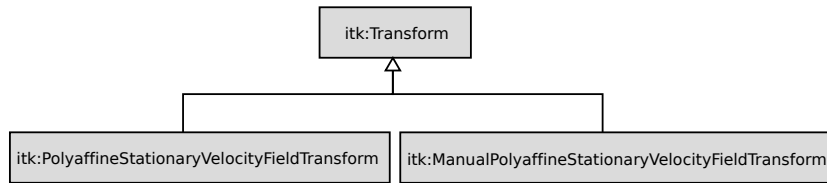


Figure C.1: UML of the new data-driven and manual polyaffine transformation tree extending from `itk::Transform`.

C.2 Trees in ITK

To implement the tree structure we use the class `itk::TreeNode`, which allows to add nodes and set values to nodes.

C.3 New Transformation Class for Polyaffine Trees

In Fig. C.1, the UML of the newly introduced data-driven and manual polyaffine transformation tree classes is depicted. The two classes extend from `itk::Transform` and thus inherit all the basic functionality, e.g. read and write to an external file.

C.4 Input Parameters

- Fixed image
- Fixed mask image
- Moving image
- Moving mask image
- Number of tree levels
- Label image to define manual regions (optional)
- Initial velocity field, e.g. initialization from coarser level (optional)
- Weight scaling factor to describe the amount of overlap between regions, a higher value represents a higher overlap (optional)
- Dilation radius added to the union of fixed and moving mask images (optional)
- Variance σ_v^2 of the velocity field vectors in mm (optional)
- Mean and concentration matrix for the normal prior distribution on the deformation parameter (optional)

C.5 Output Parameters

- Polyaffine tree transform

C.6 Example

The following example command registers a template image to a subject with five levels, 4 mm variance of the velocity vectors and 2 voxel dilation of the union of the mask images,

```
> PolyaffineLogDomainDemonsRegistration -f TemplateImage.mhd
  -F TemplateMaskImage.mhd -m SubjectImage.mhd -M SubjectMaskImage.mhd
  -s 5 -w 4 -r 2
```

Registration with prior,

```
> PolyaffineLogDomainDemonsRegistration -f TemplateImage.mhd
  -F TemplateMaskImage.mhd -m SubjectImage.mhd -M SubjectMaskImage.mhd
  -s 5 -w 4 -r 2 --prior-Mean PriorMean.txt
  --prior-Concentration PriorConcentration.txt
```

Registration with manual regions (the labels are expected to be numbered with integers ranging from one to the total number of regions),

```
> PolyaffineLogDomainDemonsRegistration -f TemplateImage.mhd
  -F TemplateMaskImage.mhd -m SubjectImage.mhd -M SubjectMaskImage.mhd
  -s 5 -w 4 -r 2 -R LabelImageManualRegions.mhd
```


Bibliography

- [Allasonnière 2007] S. Allasonnière, Y. Amit and A. Trouvé. *Towards a Coherent Statistical Framework for Dense Deformable Template Estimation*. Journal of the Royal Statistical Society: Series B (Statistical Methodology), Vol. 69, No. 1, pages 3–29, February 2007. (Cited on page 8.)
- [Allasonnière 2010] S. Allasonnière, E. Kuhn and A. Trouvé. *Construction of Bayesian Deformable Models Via a Stochastic Approximation Algorithm: A Convergence Study*. Bernoulli, Vol. 16, No. 3, 2010. (Cited on page 8.)
- [Allasonnière 2011] Stéphanie Allasonnière, Pierre Jolivet and Christophe Giraud. *Detecting Long Distance Conditional Correlations Between Anatomical Regions Using Gaussian Graphical Models*. In MFCA, MICCAI Workshop 2011, pages 111–122, Toronto, Canada, September 2011. (Cited on pages 4 and 49.)
- [Arsigny 2005] Vincent Arsigny, Xavier Pennec and Nicholas Ayache. *Polyrigid and Polyaffine Transformations: A Novel Geometrical Tool to Deal with Non-rigid Deformations – Application to the Registration of Histological Slices*. Medical Image Analysis, Vol. 9, No. 6, pages 507–523, December 2005. (Cited on pages 8, 19, 21 and 52.)
- [Arsigny 2006] Vincent Arsigny, Olivier Commowick, Xavier Pennec and Nicholas Ayache. *A Log-Euclidean Framework for Statistics on Diffeomorphisms*. In R. Larsen, M. Nielsen and J. Sparring (eds.), MICCAI 2006, Vol. 4190 of LNCS, pages 924–931. Springer, Heidelberg, 2006. (Cited on pages 6, 23, 28, 52 and 73.)
- [Arsigny 2009] Vincent Arsigny, Olivier Commowick, Nicholas Ayache and Xavier Pennec. *A Fast and Log-Euclidean Polyaffine Framework for Locally Linear Registration*. Journal of Mathematical Imaging and Vision, Vol. 33, No. 2, pages 222–238, February 2009. (Cited on pages 8, 19, 21, 22, 50 and 52.)
- [Ashburner 1997] J. Ashburner, P. Neelin, D. L. Collins, A. Evans and K. Friston. *Incorporating Prior Knowledge Into Image Registration*. NeuroImage, Vol. 6, No. 4, pages 344–352, November 1997. (Cited on pages 8, 51 and 66.)
- [Ashburner 2007] John Ashburner. *A Fast Diffeomorphic Image Registration Algorithm*. Neuroimage, Vol. 38, No. 1, pages 95–113, 2007. (Cited on page 6.)
- [Aydin 2009] Burcu Aydin, Gabor Pataki, Haonan Wang, Elizabeth Bullitt and J. S. Marron. *A Principal Component Analysis for Trees*. Annals of Applied Statistics, October 2009. (Cited on pages 9 and 96.)
- [Aydin 2012] Burcu Aydin, Gábor Pataki, Haonan Wang, Alim Ladha, Elizabeth Bullitt and J. S. Marron. *New Approaches to Principal Component Analysis*

- for Trees*. Statistics in Biosciences, pages 1–25, February 2012. (Cited on pages 9 and 96.)
- [Banerjee 2008] Onureena Banerjee, Laurent E. Ghaoui and Alexandre d’Aspremont. *Model Selection Through Sparse Maximum Likelihood Estimation for Multivariate Gaussian or Binary Data*. Journal of Machine Learning Research, Vol. 9, pages 485–516, June 2008. (Cited on pages 56, 66 and 93.)
- [Bauer 2010] Stefan Bauer, Stefan Bauer, Christof Seiler, Christof Seiler, Thibaut Bardyn, Thibaut Bardyn, Philippe Buechler, Philippe Buechler, Mauricio Reyes and Mauricio Reyes. *Atlas-Based Segmentation of Brain Tumor Images Using a Markov Random Field-Based Tumor Growth Model and Non-Rigid Registration*. EMBC, Vol. 2010, pages 4080–4083, 2010. (Cited on page 13.)
- [Benjamin 1994] Perakath C. Benjamin, Christopher P. Menzel, Richard J. Mayer, Florence Fillion, Michael T. Futrell, Paula S. deWitte and Madhavi Lingineni. *IDEF5 Method Report*, September 1994. (Cited on page 2.)
- [Bigot 2009] Jérémie Bigot, Sébastien Gadat and Jean-Michel Loubes. *Statistical M-Estimation and Consistency in Large Deformable Models for Image Warping*. Journal of Mathematical Imaging and Vision, Vol. 34, No. 3, pages 270–290, July 2009. (Cited on page 8.)
- [Billera 2001] Louus Billera, Susan Holmes and Karen Vogtmann. *Geometry of the Space of Phylogenetic Trees*. Advances in Applied Mathematics, Vol. 27, No. 4, pages 733–767, November 2001. (Cited on page 99.)
- [Blanc 2009] Rémi Blanc, Mauricio Reyes, Christof Seiler and Gábor Székely. *Conditional Variability of Statistical Shape Models Based on Surrogate Variables*. In G. Z. Yang, D. Hawkes, D. Rueckert, A. Noble and C. Taylor (eds.), MICCAI 2009, Vol. 5762 of LNCS, pages 84–91. Springer, Heidelberg, 2009. (Cited on pages 10, 11, 12, 67 and 92.)
- [Blanc 2012] Rémi Blanc, Christof Seiler, Gabor Székely, Lutz-Peter Nolte and Mauricio Reyes. *Statistical Model Based Shape Prediction from a Combination of Direct Observations and Various Surrogates. Application to Orthopaedic Research*. Medical Image Analysis, 2012. (Cited on pages 10, 11, 67 and 83.)
- [Bonaretti 2010] S. Bonaretti, M. Kistler, C. Seiler, M. Reyes and P. Buechler. *Combined Statistical Model of Bone Shape and Mechanical Properties for Bone and Implant Modeling*. In CMBBE, February 2010. (Cited on pages 10, 11, 13, 67 and 78.)
- [Bonaretti 2011] S. Bonaretti, C. Seiler, C. Boichon, P. Büchler and M. Reyes. *Mesh-Based vs. Image-Based Statistical Model of Appearance of the Human Femur:*

- A Preliminary Comparison Study for the Creation of Finite Element Meshes.* In MeshMed, MICCAI Workshop, September 2011. (Cited on pages 10, 11, 13, 17, 42, 67 and 78.)
- [Bou-Sleiman 2011] Habib Bou-Sleiman, Lucas E. Ritacco, Lutz-Peter P. Nolte and Mauricio Reyes. *Minimization of Intra-Operative Shaping of Orthopaedic Fixation Plates: A Population-Based Design.* In T. Peters, G. Fichtinger and A. Martel (eds.), MICCAI 2011, Part II, LNCS, pages 409–416. Springer, Heidelberg, 2011. (Cited on pages 10, 17, 18, 50 and 82.)
- [Bou-Sleiman 2012] Habib Bou-Sleiman, Christof Seiler, Tateyuki Iizuka, Lutz-Peter Nolte and Mauricio Reyes. *Population-Based Design of Mandibular Plates Based on Bone Quality and Morphology.* In A. Nicholas, D. Hervé, G. Polina and M. Kensaku (eds.), MICCAI 2012, LNCS. Springer, Heidelberg, 2012. (Cited on pages 10, 11, 12, 17, 18, 50, 67 and 82.)
- [Bronsard 2012] Nicolas Bronsard. *3D Anatomy of Lumbar Spine.* PhD thesis, Centre Hospitalier Universitaire de Nice, 2012. (Cited on page 89.)
- [Bryan 2009] Rebecca Bryan, Prasanth B. Nair and Mark Taylor. *Use of a Statistical Model of the Whole Femur in a Large Scale, Multi-Model Study of Femoral Neck Fracture Risk.* Journal of Biomechanics, Vol. 42, No. 13, pages 2171–2176, September 2009. (Cited on page 78.)
- [Bubenik 2010] Peter Bubenik, Gunnar Carlsson, Peter T. Kim and Zhiming Luo. *Statistical Topology Via Morse Theory, Persistence and Nonparametric Estimation.* Algebraic Methods in Statistics and Probability II, Vol. 516, page 75, 2010. (Cited on page 94.)
- [Buerger 2011] Christian Buerger, Tobias Schaeffter and Andrew P. King. *Hierarchical Adaptive Local Affine Registration for Fast and Robust Respiratory Motion Estimation.* Medical Image Analysis, Vol. 15, No. 4, pages 551–564, August 2011. (Cited on pages 8, 19, 20, 50 and 51.)
- [Cachier 2003] P. Cachier, E. Bardinet, D. Dormont, X. Pennec and N. Ayache. *Iconic Feature Based Nonrigid Registration: The PASHA Algorithm.* Computer Vision and Image Understanding, Vol. 89, No. 2-3, pages 272–298, March 2003. (Cited on page 28.)
- [Cerqueira 2002] Manuel D. Cerqueira, Neil J. Weissman, Vasken Dilsizian, Alice K. Jacobs, Sanjiv Kaul, Warren K. Laskey, Dudley J. Pennell, John A. Rumberger, Thomas Ryan, Mario S. Verani and American Heart Association Writing Group on Myocardial Segmentation and Registration for Cardiac Imaging. *Standardized Myocardial Segmentation and Nomenclature for Tomographic Imaging of the Heart: A Statement for Healthcare Professionals from the Cardiac Imaging Committee of the Council on Clinical Cardiology of*

- the American Heart Association*. Circulation, Vol. 105, No. 4, pages 539–542, January 2002. (Cited on page 85.)
- [Cervantes 2012] Thomas M. Cervantes, Alexander H. Slocum and Edward B. Seldin. *Design and Experimental Evaluation of Adjustable Bone Plates for Mandibular Fracture Fixation*. Journal of Biomechanics, Vol. 45, No. 1, pages 172–178, January 2012. (Cited on page 17.)
- [Ciccarelli 2006] Francesca D. Ciccarelli, Tobias Doerks, Christian von Mering, Christopher J. Creevey, Berend Snel and Peer Bork. *Toward Automatic Reconstruction of a Highly Resolved Tree of Life*. Science, Vol. 311, No. 5765, pages 1283–1287, March 2006. (Cited on pages 99 and 100.)
- [Clatz 2005] Olivier Clatz, Hervé Delingette, Ion-Florin F. Talos, Alexandra J. Golby, Ron Kikinis, Ferenc A. Jolesz, Nicholas Ayache and Simon K. Warfield. *Robust Nonrigid Registration to Capture Brain Shift from Intraoperative MRI*. IEEE Transactions on Medical Imaging, Vol. 24, No. 11, pages 1417–1427, November 2005. (Cited on page 90.)
- [Commowick 2008] Olivier Commowick, Vincent Arsigny, Aurélie Isambert, Jimena Costa, Frédéric Dhermain, Franc Bidault, Pierre-Yves Bondiau, Nicholas Ayache and Grégoire Malandain. *An Efficient Locally Affine Framework for the Smooth Registration of Anatomical Structures*. Medical Image Analysis, Vol. 12, No. 4, pages 427–441, August 2008. (Cited on pages 8, 19, 21, 50 and 52.)
- [Cootes 2001] T. F. Cootes, G. J. Edwards and C. J. Taylor. *Active Appearance Models*. IEEE Transactions on Pattern Analysis and Machine Intelligence, Vol. 23, No. 6, pages 681–685, June 2001. (Cited on page 9.)
- [Craig 2008] Matthew Craig, Cynthia Bir, David Viano and Scott Tashman. *Biomechanical Response of the Human Mandible to Impacts of the Chin*. Journal of Biomechanics, Vol. 41, No. 14, pages 2972–2980, October 2008. (Cited on page 17.)
- [Davis 2007] B. C. Davis, P. T. Fletcher, E. Bullitt and S. Joshi. *Population Shape Regression from Random Design Data*. In ICCV 2007, pages 1–7. IEEE, December 2007. (Cited on pages 71 and 72.)
- [Dryden 1998] I. L. Dryden and Kanti V. Mardia. *Statistical Shape Analysis*. Wiley, Edition 1, September 1998. (Cited on page 6.)
- [Durrleman 2008] Stanley Durrleman, Xavier Pennec, Alain Trounev, Paul Thompson and Nicholas Ayache. *Inferring Brain Variability from Diffeomorphic Deformations of Currents: An Integrative Approach*. Medical Image Analysis, Vol. 12, No. 5, pages 626–637, October 2008. (Cited on page 6.)

- [Durrleman 2009] Stanley Durrleman, Xavier Pennec, Alain Trouvé and Nicholas Ayache. *Statistical Models of Sets of Curves and Surfaces Based on Currents*. Medical Image Analysis, Vol. 13, No. 5, pages 793–808, October 2009. (Cited on pages 6 and 8.)
- [Durrleman 2011] Stanley Durrleman, Pierre Fillard, Xavier Pennec, Alain Trouvé and Nicholas Ayache. *Registration, Atlas Estimation and Variability Analysis of White Matter Fiber Bundles Modeled as Currents*. NeuroImage, Vol. 55, No. 3, pages 1073–1090, April 2011. (Cited on page 6.)
- [Ellis 1985] E. Ellis, K. F. Moos and A. El-Attar. *Ten Years of Mandibular Fractures: An Analysis of 2,137 Cases*. Oral Surgery, Oral Medicine, and Oral Pathology, Vol. 59, No. 2, pages 120–129, February 1985. (Cited on pages 17 and 49.)
- [Enneking 2001] William F. Enneking and Domenico A. Campanacci. *Retrieved Human Allografts: A Clinicopathological Study*. J Bone Joint Surg Am, Vol. 83, No. 7, pages 971–986, July 2001. (Cited on pages 30 and 80.)
- [Fedok 1998] F. G. Fedok, D. W. Van Kooten, L. M. DeJoseph, J. D. McGinn, B. Sobota, R. J. Levin and C. R. Jacobs. *Plating Techniques and Plate Orientation in Repair of Mandibular Angle Fractures: An in Vitro Study*. The Laryngoscope, Vol. 108, No. 8 Pt 1, pages 1218–1224, August 1998. (Cited on page 17.)
- [Feragen 2011] A. Feragen, S. Hauberg, M. Nielsen and F. Lauze. *Means in Spaces of Tree-Like Shapes*. In ICCV 2011, pages 736–746. IEEE, November 2011. (Cited on pages 9 and 96.)
- [Freiman 2011] M. Freiman, S. D. Voss and S. K. Warfield. *Demons Registration With Local Affine Adaptive Regularization: Application to Registration of Abdominal Structures*. In ISBI 2011, pages 1219–1222. IEEE, March 2011. (Cited on pages 19 and 20.)
- [Friedman 2008] Jerome Friedman, Trevor Hastie and Robert Tibshirani. *Sparse Inverse Covariance Estimation with the Graphical Lasso*. Biostatistics, Vol. 9, No. 3, pages 432–441, July 2008. (Cited on pages 56, 66 and 93.)
- [Gelman 2003] Andrew Gelman, John B. Carlin, Hal S. Stern and Donald B. Rubin. *Bayesian Data Analysis*. Chapman and Hall/CRC, Edition 2, July 2003. (Cited on page 55.)
- [Gerber 2009] S. Gerber, T. Tasdizen, S. Joshi and R. Whitaker. *On the Manifold Structure of the Space of Brain Images*. In G. Z. Yang, D. J. Hawkes, D. Rueckert, J. A. Noble and C. J. Taylor (eds.), MICCAI 2009, LNCS, pages 305–312. Springer, Heidelberg, September 2009. (Cited on page 72.)

- [Glass 1991] L. Glass, P. Hunter and A. McCulloch. *Theory of Heart: Biomechanics, Biophysics, and Nonlinear Dynamics of Cardiac Function*. Springer, Edition 1, June 1991. (Cited on page 85.)
- [Glaunès 2008] Joan Glaunès, Anqi Qiu, Michael I. Miller and Laurent Younes. *Large Deformation Diffeomorphic Metric Curve Mapping*. *International Journal of Computer Vision*, Vol. 80, No. 3, pages 317–336, December 2008. (Cited on page 6.)
- [Gottschalk 1996] S. Gottschalk, M. C. Lin and D. Manocha. *OBBTree: A Hierarchical Structure for Rapid Interference Detection*. In *SIGGRAPH, SIGGRAPH '96*, pages 171–180. ACM, 1996. (Cited on pages 25, 52 and 94.)
- [Härdle 1992] Wolfgang Härdle. *Applied Nonparametric Regression (Econometric Society Monographs)*. Cambridge University Press, January 1992. (Cited on page 74.)
- [Hernandez 2007] Monica Hernandez, Matias N. Bossa and Salvador Olmos. *Registration of Anatomical Images Using Geodesic Paths of Diffeomorphisms Parameterized with Stationary Vector Fields*. In *ICCV 2007*, pages 1–8. IEEE, October 2007. (Cited on page 6.)
- [Hughes 2005] T. J. R. Hughes, J. A. Cottrell and Y. Bazilevs. *Isogeometric Analysis: CAD, Finite Elements, NURBS, Exact Geometry and Mesh Refinement*. *Computer Methods in Applied Mechanics and Engineering*, Vol. 194, No. 39–41, pages 4135–4195, October 2005. (Cited on page 93.)
- [Janoos 2012a] F. Janoos, P. Risholm and W. Wells. *Robust Non-Rigid Registration and Characterization of Uncertainty*. In *MMBIA 2012*, pages 4321–4326. IEEE, January 2012. (Cited on page 96.)
- [Janoos 2012b] Firdaus Janoos, Petter Risholm and William Wells. *Bayesian Characterization of Uncertainty in Multi-Modal Image Registration*. In Benoît M. Dawant, Gary E. Christensen, J. Michael Fitzpatrick and Daniel Rueckert (eds.), *WBIR 2012*, Vol. 7359 of LNCS, pages 50–59. Springer, Heidelberg, 2012. (Cited on page 96.)
- [Jung 2012] Sungkyu Jung, Arusharka Sen and J. S. Marron. *Boundary Behavior in High Dimension, Low Sample Size Asymptotics of PCA*. *Journal of Multivariate Analysis*, Vol. 109, pages 190–203, August 2012. (Cited on page 8.)
- [Keyak 1990] J. H. Keyak, J. M. Meagher, H. B. Skinner and C. D. Mote. *Automated Three-Dimensional Finite Element Modelling of Bone: A New Method*. *Journal of Biomedical Engineering*, Vol. 12, No. 5, pages 389–397, September 1990. (Cited on page 78.)
- [Klein 2009] Arno Klein, Jesper Andersson, Babak A. Ardekani, John Ashburner, Brian Avants, Ming-Chang Chiang, Gary E. Christensen, D. Louis Collins,

- James Gee, Pierre Hellier, Joo H. Song, Mark Jenkinson, Claude Lepage, Daniel Rueckert, Paul Thompson, Tom Vercauteren, Roger P. Woods, John J. Mann and Ramin V. Parsey. *Evaluation of 14 Nonlinear Deformation Algorithms Applied to Human Brain MRI Registration*. NeuroImage, Vol. 46, No. 3, pages 786–802, July 2009. (Cited on pages 6 and 8.)
- [Kovan 2008] Volkan Kovan. *An Assessment of Impact Strength of the Mandible*. Journal of Biomechanics, Vol. 41, No. 16, pages 3488–3491, December 2008. (Cited on page 17.)
- [Kozic 2008] N. Kozic, M. Reyes, M. Tannast, L. P. Nolte and M. A. G. Gonzalez. *Assessment of Anatomical Criteria Across Populations Using Statistical Shape Models and Level Sets*. In CAOS 2008, pages 46–49, 2008. (Cited on page 68.)
- [Kozic 2010] Nina Kozic, Stefan Weber, Philippe Büchler, Christian Lutz, Nils Reimers, Miguel A. González Ballester and Mauricio Reyes. *Optimisation of Orthopaedic Implant Design Using Statistical Shape Space Analysis Based on Level Sets*. Medical Image Analysis, Vol. 14, No. 3, pages 265–275, June 2010. (Cited on pages 17, 18 and 82.)
- [Liu 2004] T. Liu, D. Shen and C. Davatzikos. *Predictive Modeling of Anatomic Structures Using Canonical Correlation Analysis*. In ISBI 2005, pages 1279–1282, April 2004. (Cited on page 71.)
- [Lo 2010] Pechin Lo, Jon Sparring, Haseem Ashraf, Jesper J. Pedersen and Marleen de Bruijne. *Vessel-Guided Airway Tree Segmentation: A Voxel Classification Approach*. Medical image analysis, Vol. 14, No. 4, pages 527–538, August 2010. (Cited on pages 9 and 96.)
- [Lorenzi 2012] Marco Lorenzi and Xavier Pennec. *Regional Flux Analysis of Longitudinal Atrophy in Alzheimer’s Disease*. In A. Nicholas, D. Hervé, G. Polina and M. Kensaku (eds.), MICCAI 2012, LNCS. Springer, Heidelberg, 2012. (Cited on page 90.)
- [Lovald 2009] Scott T. Lovald, Jon D. Wagner and Bret Baack. *Biomechanical Optimization of Bone Plates Used in Rigid Fixation of Mandibular Fractures*. Journal of Oral and Maxillofacial Surgery, Vol. 67, No. 5, pages 973–985, May 2009. (Cited on page 17.)
- [Lovald 2010] Scott Lovald, Bret Baack, Curtis Gaball, Garth Olson and Anna Hoard. *Biomechanical Optimization of Bone Plates Used in Rigid Fixation of Mandibular Symphysis Fractures*. Journal of Oral and Maxillofacial Surgery, Vol. 68, No. 8, pages 1833–1841, August 2010. (Cited on pages 17 and 50.)
- [Ma 2008] Jun Ma, Michael I. Miller, Alain Trouvé and Laurent Younes. *Bayesian Template Estimation in Computational Anatomy*. NeuroImage, Vol. 42, No. 1, pages 252–261, August 2008. (Cited on page 8.)

- [MacKay 1992] David J. C. MacKay. *Bayesian Interpolation*. Neural Computation, Vol. 4, No. 3, pages 415–447, May 1992. (Cited on page 93.)
- [Martín-Fernández 2009] Miguel A. Martín-Fernández, Marcos Martín-Fernández and Carlos Alberola-López. *A Log-Euclidean Polyaffine Registration for Articulated Structures in Medical Images*. In G. Z. Yang, D. J. Hawkes, D. Rueckert, J. A. Noble and C. J. Taylor (eds.), MICCAI 2009, Part I, LNCS, pages 156–164. Springer, Heidelberg, 2009. (Cited on page 19.)
- [McBroom 1985] R. J. McBroom, W. C. Hayes, W. T. Edwards, R. P. Goldberg and A. A. White. *Prediction of Vertebral Body Compressive Fracture Using Quantitative Computed Tomography*. The Journal of Bone and Joint Surgery, Vol. 67, No. 8, pages 1206–1214, October 1985. (Cited on page 42.)
- [McLeod 2012] Kristin McLeod, Christof Seiler, Adityo Prakosa, Maxime Sermesant and Xavier Pennec. *A Near-Incompressible Poly-Affine Motion Model for Cardiac Function Analysis*. In STACOM, MICCAI Workshop, 2012. (Cited on pages 10, 11, 13, 67 and 85.)
- [Metzen 2009] Jan H. Metzen, Tim Kröger, Andrea Schenk, Stephan Zidowitz, Heinz-Otto Peitgen and Xiaoyi Jiang. *Matching of Anatomical Tree Structures for Registration of Medical Images*. Image and Vision Computing, Vol. 27, No. 7, pages 923–933, June 2009. (Cited on pages 9 and 96.)
- [Metzger 2011] Marc C. Metzger, Mathias Vogel, Bettina Hohlweg-Majert, Hansjörg Mast, Xianqun Fan, Alexandra Rüdell and Stefan Schlager. *Anatomical Shape Analysis of the Mandible in Caucasian and Chinese for the Production of Preformed Mandible Reconstruction Plates*. Journal of Cranio-Maxillo-Facial Surgery, Vol. 39, No. 6, pages 393–400, September 2011. (Cited on pages 17 and 18.)
- [Moore 1985] G. Moore, T. Olson and A. Yonkers. *A Retrospective of 100 Fractures in 56 Patients*. Nebraska Medical Journal, Vol. 70, pages 120–123, 1985. (Cited on page 17.)
- [Muscolo 2005] D. L. Muscolo, M. A. Ayerza, L. A. Aponte-Tinao and M. Ranalletta. *Use of Distal Femoral Osteoarticular Allografts in Limb Salvage Surgery*. J Bone Joint Surg Am, Vol. 87, No. 11, pages 2449–2455, November 2005. (Cited on pages 30 and 80.)
- [Ourselin 2000] S. Ourselin, A. Roche, S. Prima and N. Ayache. *Block Matching: A General Framework to Improve Robustness of Rigid Registration of Medical Images*. In S. Delp, A. DiGoia and B. Jaramaz (eds.), MICCAI 2000, Vol. 1935 of LNCS, pages 557–566. Springer, Heidelberg, 2000. (Cited on page 81.)
- [Owen 2011] M. Owen and J. S. Provan. *A Fast Algorithm for Computing Geodesic Distances in Tree Space*. IEEE/ACM Transactions on Computational Biol-

- ogy and Bioinformatics, Vol. 8, No. 1, pages 2–13, January 2011. (Cited on pages 9 and 96.)
- [Penec 2005] X. Penec, R. Stefanescu, V. Arsigny, P. Fillard and N. Ayache. *Riemannian Elasticity: A Statistical Regularization Framework for Non-Linear Registration*. In D. James and G. Guido (eds.), MICCAI 2005, Part II, LNCS, pages 943–950. Springer, Heidelberg, 2005. (Cited on page 51.)
- [Penec 2008] Xavier Penec. *Statistical Computing on Manifolds: From Riemannian Geometry to Computational Anatomy*. In Emerging Trends in Visual Computing, Vol. 5416 of LNCS, pages 347–386. Springer, 2008. (Cited on page 73.)
- [Pizer 2003] Stephen M. Pizer, P. Thomas Fletcher, Sarang Joshi, Andrew Thall, James Z. Chen, Yonatan Fridman, Daniel S. Fritsch, A. Graham Gash, John M. Glotzer, Michael R. Jiroutek, Conglin Lu, Keith E. Muller, Gregg Tracton, Paul Yushkevich and Edward L. Chaney. *Deformable M-Reps for 3D Medical Image Segmentation*. International Journal of Computer Vision, Vol. 55, No. 2, pages 85–106, November 2003. (Cited on pages 6 and 18.)
- [Rao 2008] A. Rao, P. Aljabar and D. Rueckert. *Hierarchical Statistical Shape Analysis and Prediction of Sub-Cortical Brain Structures*. Medical Image Analysis, Vol. 12, No. 1, pages 55–68, February 2008. (Cited on page 71.)
- [Risholm 2011] Petter Risholm, James Ross, George R. Washko and William M. Wells. *Probabilistic Elastography: Estimating Lung Elasticity*. In G. Székely and H. Hahn (eds.), IPMI 2011, LNCS, pages 699–710. Springer, Heidelberg, 2011. (Cited on page 96.)
- [Risser 2010] Laurent Risser, François-Xavier X. Vialard, Robin Wolz, Darryl D. Holm and Daniel Rueckert. *Simultaneous Fine and Coarse Diffeomorphic Registration: Application to Atrophy Measurement in Alzheimer’s Disease*. In T. Jiang, N. Navab, J. P. W. Pluim and M. A. Viergever (eds.), MICCAI 2010, Part II, LNCS, pages 610–617. Springer, Heidelberg, 2010. (Cited on page 8.)
- [Ritacco 2010] L. E. Ritacco, A. E. Orias, L. A. Tinao, D. L. Muscolo, F. G. Bernaldo de Quirós and I. Nozomu. *Three-Dimensional Morphometric Analysis of the Distal Femur: A Validity Method for Allograft Selection Using a Virtual Bone Bank*. In Medinfo, September 2010. (Cited on page 81.)
- [Ritacco 2012] Lucas E. Ritacco, Christof Seiler, German L. Farfalli, Lutz Nolte, Mauricio Reyes, Domingo L. Muscolo and Luis A. Tinao. *Validity of an Automatic Measure Protocol in Distal Femur for Allograft Selection from a Three-Dimensional Virtual Bone Bank System*. Cell and Tissue Banking, pages 1–8, April 2012. (Cited on pages 10, 11, 12, 30, 67 and 81.)

- [Rohlfing 2009] Torsten Rohlfing, Edith V. Sullivan and Adolf Pfefferbaum. *Regression Models of Atlas Appearance Information Processing in Medical Imaging*. In Jerry L. Prince, Dzung L. Pham and Kyle J. Myers (eds.), IPMI 2009, Vol. 5636 of LNCS, pages 151–162. Springer, Heidelberg, 2009. (Cited on page 92.)
- [Rohlfing 2012] Torsten Rohlfing. *Image Similarity and Tissue Overlaps as Surrogates for Image Registration Accuracy: Widely Used But Unreliable*. IEEE Transactions on Medical Imaging, Vol. 31, No. 2, pages 153–163, February 2012. (Cited on pages 60 and 89.)
- [Rosse 2008] Cornelius Rosse and José L. V. Mejino. *The Foundational Model of Anatomy Ontology Anatomy Ontologies for Bioinformatics*. In Albert Burger, Duncan Davidson and Richard Baldock (eds.), Anatomy Ontologies for Bioinformatics, Vol. 6 of Computational Biology, Chapter 4, pages 59–117. Springer London, London, 2008. (Cited on pages 2, 3, 4, 47 and 48.)
- [Sabuncu 2011] Mert R. Sabuncu and Koen Van Leemput. *The Relevance Voxel Machine (RVoxM): A Bayesian Method for Image-Based Prediction*. In T. Peters, G. Fichtinger and A. Martel (eds.), MICCAI 2011, Part III, LNCS, pages 99–106. Springer, Heidelberg, 2011. (Cited on page 93.)
- [Schileo 2007] Enrico Schileo, Fulvia Taddei, Andrea Malandrino, Luca Cristofolini and Marco Viceconti. *Subject-specific finite element models can accurately predict strain levels in long bones*. Journal of biomechanics, Vol. 40, No. 13, pages 2982–2989, 2007. (Cited on page 78.)
- [Seiler 2009a] Christof Seiler, Philippe Büchler, Lutz-Peter Nolte, Rasmus Paulsen and Mauricio Reyes. *Hierarchical Markov Random Fields Applied to Model Soft Tissue Deformations on Graphics Hardware*. In Nadia Magnenat-Thalmann, Jian J. Zhang and David D. Feng (eds.), Recent Advances in the 3D Physiological Human, Chapter 9, pages 133–148. Springer London, London, 2009. (Cited on page 12.)
- [Seiler 2009b] Christof Seiler, Stefan Weber, Walter Schmidt, Felix Fischer, Nils Reimers and Mauricio Reyes. *Automatic Landmark Propagation for Left and Right Symmetry Assessment of Tibia and Femur: A Computational Anatomy Based Approach*. In CAOS 2009, June 2009. (Cited on pages 11, 13, 67 and 68.)
- [Seiler 2010a] Christof Seiler, Amiq Gazdhar, Thomas Geiser, Mauricio Reyes and Benjamin Gantenbein-Ritter. *Mesenchymal Stem Cell Classification During Differentiation Based on Shape Information*. In TERMIS 2010, June 2010. (Cited on page 13.)
- [Seiler 2010b] Christof Seiler, Xavier Pennec and Mauricio Reyes. *Parametric Regression of 3D Medical Images Through the Exploration of Non-Parametric*

- Regression Models*. In ISBI 2010, April 2010. (Cited on pages 11, 12, 67 and 71.)
- [Seiler 2011a] Christof Seiler, Xavier Pennec and Mauricio Reyes. *Geometry-Aware Multiscale Image Registration Via OBBTree-Based Polyaffine Log-Demons*. In T. Peters, G. Fichtinger and A. Martel (eds.), MICCAI 2011, LNCS. Springer, Heidelberg, September 2011. (Cited on pages 10, 12, 15 and 20.)
- [Seiler 2011b] Christof Seiler, Xavier Pennec, Lucas Ritacco and Mauricio Reyes. *Femur Specific Polyaffine Model to Regularize the Log-Domain Demons Registration*. In SPIE Medical Imaging, Vol. 7962, February 2011. (Cited on pages 10, 12, 15, 19, 20 and 24.)
- [Seiler 2012a] C. Seiler, A. Gazdhar, M. Reyes, L. M. Benneker, T. Geiser, K. A. Siebenrock and B. Gantenbein-Ritter. *Time-Lapse Microscopy and Classification of 2D Human Mesenchymal Stem Cells Based on Cell Shape Picks Up Myogenic from Osteogenic and Adipogenic Differentiation*. Journal of Tissue Engineering and Regenerative Medicine, 2012. (Cited on page 11.)
- [Seiler 2012b] Christof Seiler, Xavier Pennec and Mauricio Reyes. *A Generative Statistical Model for Multiscale Diffeomorphic Deformations*. IEEE Transactions on Medical Imaging (to be submitted), 2012. (Cited on pages 11, 12 and 45.)
- [Seiler 2012c] Christof Seiler, Xavier Pennec and Mauricio Reyes. *Capturing the Multiscale Anatomical Shape Variability with Polyaffine Transformation Trees*. Medical Image Analysis, 2012. (Cited on pages 10, 11, 12, 15, 51, 52, 55, 56 and 57.)
- [Seiler 2012d] Christof Seiler, Xavier Pennec and Mauricio Reyes. *Simultaneous Multiscale Polyaffine Registration by Incorporating Deformation Statistics*. In A. Nicholas, D. Hervé, G. Polina and M. Kensaku (eds.), MICCAI 2012, Part II, Vol. 7511 of LNCS, pages 130–137. Springer, Heidelberg, 2012. (Cited on pages 11, 12 and 45.)
- [Siddiqi 2008] K. Siddiqi and S. M. Pizer. *Medial Representations: Mathematics, Algorithms and Applications*. Springer Verlag, 2008. (Cited on pages 6 and 18.)
- [Sommer 2011a] Stefan Sommer, François Lauze, Mads Nielsen and Xavier Pennec. *Kernel Bundle EPDiff: Evolution Equations for Multi-Scale Diffeomorphic Image Registration*. In A. M. Bruckstein, B. ter Haar Romeny, A. M. Bronstein and M. M. Bronstein (eds.), Scale Space and Variational Methods in Computer Vision, Vol. 6667 of LNCS, Ein-Gedi, Israël, June 2011. Springer. (Cited on page 8.)

- [Sommer 2011b] Stefan Sommer, Mads Nielsen, François Lauze and Xavier Pennec. *A Multi-Scale Kernel Bundle for LDDMM: Towards Sparse Deformation Description Across Space and Scales*. In G. Székely and H. Hahn (eds.), IPMI 2011, LNCS, pages 624–635. Springer, Heidelberg, 2011. (Cited on page 8.)
- [Stanley 2001] Richard P. Stanley. *Enumerative Combinatorics, Volume 2*. Cambridge University Press, Edition 1, June 2001. (Cited on page 99.)
- [Stefanou 2009] George Stefanou. *The Stochastic Finite Element Method: Past, Present and Future*. *Computer Methods in Applied Mechanics and Engineering*, Vol. 198, No. 9-12, pages 1031–1051, February 2009. (Cited on pages 78 and 93.)
- [Steinke 2009] F. Steinke and M. Hein. *Non-Parametric Regression Between Riemannian Manifolds*. In *Conference in Advances in Neural Information Processing Systems*, Vol. 21, pages 1561–1568, 2009. (Cited on page 72.)
- [Taquet 2011] M. Taquet, B. Macq and S. K. Warfield. *Spatially Adaptive Log-Euclidean Polyaffine Registration Based on Sparse Matches*. In T. Peters, G. Fichtinger and A. Martel (eds.), MICCAI 2011, LNCS. Springer, Heidelberg, September 2011. (Cited on pages 19, 20, 50, 51 and 90.)
- [Tipping 2001] Michael E. Tipping. *Sparse Bayesian Learning and the Relevance Vector Machine*. *Journal of Machine Learning Research*, Vol. 1, pages 211–244, September 2001. (Cited on page 93.)
- [Tsiligkaridis 2012] Theodoros Tsiligkaridis, Alfred O. Hero and Shuheng Zhou. *Convergence Properties of Kronecker Graphical Lasso Algorithms*. In *IEEE Statistical Signal Processing Workshop*, August 2012. (Cited on pages 66 and 93.)
- [Urken 1991] M. L. Urken, H. Weinberg, C. Vickery, D. Buchbinder, W. Lawson and H. F. Biller. *Oromandibular Reconstruction Using Microvascular Composite Free Flaps. Report of 71 Cases and a New Classification Scheme for Bony, Soft-Tissue, and Neurologic Defects*. *Archives of Otolaryngology–Head & Neck Surgery*, Vol. 117, No. 7, pages 733–744, July 1991. (Cited on pages 17 and 49.)
- [Vaillant 2005] Marc Vaillant and Joan Glaunès. *Surface Matching Via Currents*. In J. Prince, D. Pham and K. Myers (eds.), IPMI 2005, LNCS, pages 381–392. Springer, Heidelberg, 2005. (Cited on page 6.)
- [Vercauteren 2007] Tom Vercauteren, Xavier Pennec, Aymeric Perchant and Nicholas Ayache. *Non-parametric Diffeomorphic Image Registration with the Demons Algorithm*. In N. Ayache, S. Ourselin and A. J. Maeder (eds.), MICCAI 2007, Vol. 4792 of LNCS, pages 319–326, Berlin, Heidelberg, 2007. Springer, Heidelberg. (Cited on page 68.)

- [Vercauteren 2008] Tom Vercauteren, Xavier Pennec, Aymeric Perchant and Nicholas Ayache. *Symmetric Log-Domain Diffeomorphic Registration: A Demons-Based Approach*. In Dimitris Metaxas, Leon Axel, Gabor Fichtinger and Gábor Székely (eds.), MICCAI 2008, Vol. 5241 of LNCS, pages 754–761. Springer, Heidelberg, 2008. (Cited on pages 73 and 81.)
- [Vercauteren 2009] Tom Vercauteren, Xavier Pennec, Aymeric Perchant and Nicholas Ayache. *Diffeomorphic Demons: Efficient Non-Parametric Image Registration*. NeuroImage, Vol. 45, No. 1 Suppl, pages S61–S72, March 2009. (Cited on pages 6, 20, 28, 29, 52, 78 and 105.)
- [Vuong 2010] A. V. Vuong, C. Heinrich and B. Simeon. *ISOGAT: A 2D tutorial MATLAB Code for Isogeometric Analysis*. Computer Aided Geometric Design, Vol. 27, No. 8, pages 644–655, November 2010. (Cited on page 93.)
- [Wang 2009] Hao Wang and Mike West. *Bayesian Analysis of Matrix Normal Graphical Models*. Biometrika, Vol. 96, No. 4, pages 821–834, December 2009. (Cited on pages 66 and 94.)
- [Wang 2012] H. Wang and S. Z. Li. *Efficient Gaussian Graphical Model Determination Under G-Wishart Prior Distributions*. Electronic Journal of Statistics, Vol. 6, 2012. (Cited on pages 66 and 94.)
- [Watanabe 2010] Hiroshi Watanabe, Momin M. Abdul, Tohru Kurabayashi and Hideki Aoki. *Mandible Size and Morphology Determined with CT on a Premise of Dental Implant Operation*. Surgical and Radiologic Anatomy, Vol. 32, No. 4, pages 343–349, April 2010. (Cited on page 42.)
- [Werner 2008] Karl Werner, Magnus Jansson and Petre Stoica. *On Estimation of Covariance Matrices With Kronecker Product Structure*. IEEE Transactions on Signal Processing, Vol. 56, No. 2, pages 478–491, February 2008. (Cited on pages 66 and 93.)
- [Wipf 2011] D. P. Wipf, B. D. Rao and S. Nagarajan. *Latent Variable Bayesian Models for Promoting Sparsity*. IEEE Transactions on Information Theory, Vol. 57, No. 9, pages 6236–6255, 2011. (Cited on page 93.)
- [Yang 2008] Yuhui M. Yang, Daniel Rueckert and Anthony M. J. Bull. *Predicting the Shapes of Bones at a Joint: Application to the Shoulder*. Computer Methods in Biomechanics and Biomedical Engineering, Vol. 11, No. 1, pages 19–30, February 2008. (Cited on page 71.)
- [Zhang 2011] Weiwei Zhang, Michael J. Brady, Harald Becher and Alison J. Noble. *Spatio-Temporal (2D+T) Non-Rigid Registration of Real-Time 3D Echocardiography and Cardiovascular MR Image Sequences*. Physics in Medicine and Biology, Vol. 56, No. 5, pages 1341+, March 2011. (Cited on pages 8, 19, 20, 50, 51 and 93.)

- [Zhuang 2010] Xiahai Zhuang, Kawal S. Rhode, Reza S. Razavi, David J. Hawkes and Sebastien Ourselin. *A Registration-Based Propagation Framework for Automatic Whole Heart Segmentation of Cardiac MRI*. IEEE Transactions on Medical Imaging, Vol. 29, No. 9, pages 1612–1625, 2010. (Cited on pages 19 and 50.)

Curriculum Vitae

Name	Christof Seiler
Current address	Balderstrasse 31, 3007 Bern, Switzerland

Education

2009–expected 2012	Joint Ph.D. in Biomedical Engineering and Image Processing , INRIA Sophia Antipolis and University of Bern, France and Switzerland
2006–2008	M.Sc. in Biomedical Engineering , University of Bern, Switzerland
2001–2005	Dipl. Ing. FH (equivalent to a bachelor's degree) in Computer Science, University of Applied Sciences, Biel, Switzerland

Master Thesis

Title	Displacement Vector Field Regularization for Modelling of Soft Tissue Deformations (Grade 6.0/6.0)
Supervisor	Mauricio Reyes, Ph.D.
Description	The thesis presents a method to simulate soft tissue deformations taking into account material properties retrieved directly from medical images. The project was realized using Hierarchical Markov Random Fields and implemented for Graphics Processing Units.

Bachelor Thesis

Title	3D Simulation of Lego Mindstorms Robots (Grade 5.83/6.0)
Supervisors	Claude Fuhrer, Ph.D., Jean-Paul Dubois
Description	Development of a 3D simulation software for Lego Mindstorms robots. The user can run the same Java program on the simulation software and the real robot to conduct experiments.

Oral Podium Presentations at International Scientific Conferences

September 2011	MICCAI (oral presentation acceptance rate 4.2%), Toronto, Canada, 819 papers were submitted to the conference
February 2011	SPIE Medical Imaging (Image Processing) , Orlando, USA
June 2010	TERMIS , Galway, Ireland
June 2009	CAOS , Boston, USA
December 2008	3D Physiological Human , Zermatt, Switzerland

Poster Presentations at International Scientific Conferences

October 2012	MICCAI (poster acceptance rate 32%), Nice, France, 779 papers were submitted to the conference
April 2010	ISBI , Rotterdam, The Netherlands

Rewiever for International Scientific Conferences

Since 2012 | **MICCAI** (usual acceptance rate 32%)

Research Stays and Visits Abroad

2011–2012 | **Joint Ph.D.**, Asclepios Team, INRIA Sophia Antipolis, France
(1 year)
Fall Semester | **Visiting Graduate Fellow**, Statistical and Applied Mathematical Sci-
2010 (4 months) | ences Institute (SAMSI), Research Triangle Park, NC, USA

Summer School

2009 (1 week) | Summer School on Manifold Learning in Image and Signal Analysis,
Backfallsbyen, Ven, Sweden, Participation and presentation of Non-
Parametric Image Regression in a Log-Euclidean Framework

Teaching

Fall Semester | Medical Image Analysis (master level), ETH and University of Bern,
2009 | Zürich and Bern, Switzerland, Presentation of 2 lessons on Computational
Anatomy
Fall Semester | Medical Image Analysis (master level), ETH, Zürich, Switzerland, Pre-
2008 | sentation of 4 lessons on shape representation

Past Student Supervision

Bachelor Thesis | Konrad Moser, University of Applied Sciences, Brugg, Switzerland, De-
in Computer | velopment of a C++ Interface for R
Science

Industrial Experience Abroad

2003–2004 | **Internship in Software Engineering**, Oridus Inc., Silicon Valley, Fre-
(1 year) | mont, CA, USA

Industrial Experience in Switzerland

2006–2008 | **Software Engineer** (part time 45%), ISS AG, Port, Switzerland
(18 months)
2006 | **Software Engineer** (part time 55%), MEM Research Center, University
(11 months) | of Bern, Switzerland
2005 | **Consultant**, Oridus Inc., Biel, Switzerland
(3 months)

Usage of Computing Clusters

2011–2012 | dream, INRIA Sophia Antipolis, France
2011–2012 | obelix, University of Bern, Switzerland

Publications and Awards

Are shown in the introduction in Section 1.4.

Declaration of Originality

Last name, first name: Seiler, Christof
Matriculation number: 01-195-486

I hereby declare that this thesis represents my original work and that I have used no other sources except as noted by citations. All data, tables, figures and text citations which have been reproduced from any other source, including the internet, have been explicitly acknowledged as such. I am aware that in case of non-compliance, the Senate is entitled to divest me of the doctorate degree awarded to me on the basis of the present thesis, in accordance with the “Statut der Universität Bern (Universitätsstatut; UniSt)”, Art. 20, of 17 December 1997.

Place, date

Signature

.....

.....